

The hadronic running of the electromagnetic coupling and the electroweak mixing angle from lattice QCD

Marco Cè^{a,b}, Antoine Gérardin^c, Georg von Hippel^d, Harvey B. Meyer^{d,e,f},
Kohtaroh Miura^{d,e,f,g}, Konstantin Ottnad^d, Andreas Risch^h, Teseo San José^{d,e,f},
Jonas Wilhelm^d, and Hartmut Wittig^{d,e,f,b}

^a *Albert Einstein Center for Fundamental Physics (AEC) and Institut für Theoretische Physik, Universität Bern, Sidlerstrasse 5, 3012 Bern, Switzerland*

^b *Department of Theoretical Physics, CERN, 1211 Geneva 23, Switzerland*

^c *Aix-Marseille Université, Université de Toulon, CNRS, CPT, Marseille, France*

^d *PRISMA⁺ Cluster of Excellence and Institut für Kernphysik, Johannes Gutenberg-Universität Mainz, 55099 Mainz, Germany*

^e *Helmholtz-Institut Mainz, Johannes Gutenberg-Universität Mainz, 55099 Mainz, Germany*

^f *GSI Helmholtzzentrum für Schwerionenforschung, Planckstraße 1, 64291 Darmstadt, Germany*

^g *Kobayashi-Maskawa Institute for the Origin of Particles and the Universe, Nagoya University, Japan*

^h *John von Neumann-Institut für Computing NIC, Deutsches Elektronen-Synchrotron DESY, Platanenallee 6, 15738 Zeuthen, Germany*

We compute the hadronic running of the electromagnetic and weak couplings in lattice QCD with $N_f = 2 + 1$ flavors of $\mathcal{O}(a)$ improved Wilson fermions. Using two different discretizations of the vector current, we compute the quark-connected and -disconnected contributions to the hadronic vacuum polarization (HVP) functions $\bar{\Pi}^{\gamma\gamma}$ and $\bar{\Pi}^{\gamma Z}$ for Euclidean squared momenta $Q^2 \leq 7 \text{ GeV}^2$. Gauge field ensembles at four values of the lattice spacing and several values of the pion mass, including its physical value, are used to extrapolate the results to the physical point. The ability to perform an exact flavor decomposition allows us to present the most precise determination to date of the SU(3)-flavor-suppressed HVP function $\bar{\Pi}^{08}$ that enters the running of $\sin^2 \theta_W$. Our results for $\bar{\Pi}^{\gamma\gamma}$, $\bar{\Pi}^{\gamma Z}$ and $\bar{\Pi}^{08}$ are presented in terms of rational functions for continuous values of Q^2 below 7 GeV^2 . We observe a tension of up to 3.5 standard deviation between our lattice results for $\Delta\alpha_{\text{had}}^{(5)}(-Q^2)$ and estimates based on the R -ratio for space-like momenta in the range $3\text{--}7 \text{ GeV}^2$. The tension is, however, strongly diminished when translating our result to the Z pole, by employing the Euclidean split technique and perturbative QCD, which yields $\Delta\alpha_{\text{had}}^{(5)}(M_Z^2) = 0.02773(15)$ and agrees with results based on the R -ratio within the quoted uncertainties.

MITP-22-019
CERN-TH-2022-035
DESY-22-050

Contents

1.	Introduction	3
2.	The running of electroweak couplings	4
2.1.	The electromagnetic coupling	4
2.2.	The electroweak mixing angle	5
3.	Methodology	7
3.1.	The TMR method	7
3.2.	Flavor decomposition	8
3.3.	Renormalization and $\mathcal{O}(a)$ improvement	10
3.4.	Lattice setup	10
3.5.	Quark-disconnected diagrams	12
3.6.	Signal-to-noise ratio and bounding method	13
3.7.	Correction for finite-size effects	15
3.7.1.	Meyer-Lellouch-Lüscher formalism with Gounaris-Sakurai parametrization	17
3.7.2.	Hansen-Patella method	18
3.8.	Lattice results	20
4.	Results at the physical point	22
4.1.	Extrapolation strategy	22
4.1.1.	Study of the fit model systematics	24
4.1.2.	Extrapolation of the charm contribution	26
4.2.	The running with energy	27
4.2.1.	Scale-setting error	27
4.2.2.	Charm quark loop effects	29
4.2.3.	Isospin-breaking effects	30
4.2.4.	Rational approximation of the running	31
4.2.5.	Dependence on the definition of the physical point	32
5.	Comparison and discussion	33
5.1.	Hadronic running of the electromagnetic coupling	33
5.2.	Hadronic running of the electroweak mixing angle	39
6.	Conclusions	42
	Acknowledgements	42
A.	Pseudoscalar meson and gradient flow observables	43
B.	Autocorrelation study	44
C.	Treatment of quark-disconnected diagrams	45
D.	Phenomenological model of the \bar{H}^{08} contribution	47
E.	Phenomenological estimate of the charm quenching effect	49
E.1.	D meson loops	49
E.2.	Perturbative estimate	50
E.3.	Change in the ω and ϕ masses and decays constants due to mixing with J/ψ	51
E.4.	Synthesis	51
F.	Extended table of results at the physical point	51
	References	58

1. Introduction

Precision observables play a crucial role in the search for physics beyond the Standard Model (BSM). They allow for exploring the limits of the Standard Model (SM) and constrain possible extensions in a way that is complementary to direct searches in experiments at high-energy colliders. This requires both the theoretical prediction and the corresponding experimental result to be determined to a high level of precision. The evaluation of the SM prediction is particularly challenging when the quantity of interest receives significant contributions from hadronic effects. Indeed, because of the growth of the strong coupling in the low-energy domain, perturbative methods fail to describe the strong interactions at typical hadronic scales, in contrast to the high-energy regime and the electroweak sector. Lattice QCD has emerged as one of the leading methods to compute these non-perturbative QCD contributions from first principles. Lattice calculations have reached sub-percent precision for many observables that are now routinely used in precision tests of the SM [1, 2].

The prominent example of the muon anomalous magnetic moment, a_μ , is an apt illustration of the importance of precision observables. The measurement of a_μ by the E989 experiment at Fermilab [3], when combined with the earlier experimental determination at BNL [4], produces a tension of 4.2σ with the theoretical prediction summarized in the 2020 White Paper [5] by the *Muon $g - 2$ Theory Initiative*. Given that the uncertainty of the SM prediction is dominated by the hadronic vacuum polarization (HVP) and, to a lesser extent, the hadronic light-by-light scattering (HLbL) contribution, it is clear that efforts to reduce the theoretical error must focus on hadronic effects. In fact, the recent lattice calculation of the HVP contribution by the Budapest-Marseille-Wuppertal collaboration (BMWc) [6] suggests a strongly reduced tension of the SM prediction for a_μ with the experiment, and further lattice calculations are underway to confirm or refute these findings.

In this paper, we present results for two closely related observables that play a central role in SM tests, namely the energy dependence (running) of the electromagnetic coupling, α , as well as that of the electroweak mixing angle, $\sin^2 \theta_W$. The former is an important input quantity for electroweak precision tests, while the running of the mixing angle is susceptible to the effects of BSM physics, particularly at low energies [7]. As in the case of a_μ , the overall precision of both quantities is limited by hadronic effects. We employ the same methodology as in our earlier lattice QCD calculation of $a_\mu^{\text{HVP,LO}}$ [8], to compute the hadronic vacuum polarization functions $\bar{\Pi}^{\gamma\gamma}$ and $\bar{\Pi}^{\gamma Z}$ that are relevant for the running of α and $\sin^2 \theta_W$, respectively. A key advantage of the lattice approach is the ability to perform an exact valence flavor decomposition of the various contributions. This has allowed us to determine the isoscalar ($I = 0$) contribution $\bar{\Pi}^{08}$ to the vacuum polarization function $\bar{\Pi}^{\gamma Z}$ with much higher accuracy compared to the standard approach based on dispersion theory and experimentally determined hadronic cross sections.

We present our main results for the HVP functions $\bar{\Pi}^{\gamma\gamma}$, $\bar{\Pi}^{\gamma Z}$ and $\bar{\Pi}^{08}$ as continuous rational functions in the Euclidean squared momentum Q^2 up to $Q^2 \leq 7 \text{ GeV}^2$ (see eqs. (46), (48) and (58)), together with the corresponding correlation matrices. By employing the Euclidean split technique (or Adler function approach) [9, 10] we can combine our lattice result for the hadronic running of the QED coupling with perturbative QCD to translate it to the time-like momentum region. At the scale of the Z boson mass we obtain

$$\Delta\alpha_{\text{had}}^{(5)}(M_Z^2) = 0.02773(15), \quad (1)$$

which agrees with corresponding results derived from dispersion theory and the experimentally measured R -ratio [11–13] within errors.

This paper is organized as follows: In section 2 we review the main definitions relating to the running of the electromagnetic and weak couplings. Our methodology to compute the HVP

contribution to the running of α and $\sin^2 \theta_W$ in lattice QCD, including the treatment of the different sources of systematic errors, is discussed in section 3, with section 3.8 describing the details of the lattice computation and the results on individual gauge ensembles. In section 4 we discuss the extrapolation of our lattice results to the continuum limit and physical pion and kaon masses for a range of values of Q^2 , quoting the complete statistical and systematic error estimate. A detailed discussion of our results, including their comparison with phenomenological estimates is presented in section 5. We end with a short summary and conclusions. Further details on the auxiliary calculation of pseudoscalar meson observables, error estimation, phenomenological models, as well as extended tables of results at the physical point are relegated to several appendices. Readers who are not interested in the technical aspects of the lattice calculation can skip section 3 and go directly to sections 4.2 and 5.

2. The running of electroweak couplings

2.1. The electromagnetic coupling

The first quantity that we consider is the electromagnetic coupling $\alpha \equiv e^2/(4\pi)$. The value that is relevant for interactions at energies much smaller than the electron mass, such as in Thomson scattering, is the fine-structure constant, which is one of the most precisely known quantities in experimental physics, with a precision of up to 81 parts per trillion in the most recent measurement [14]. In the rest of this paper we use as reference value in the Thomson limit (that is, for $q^2 \rightarrow 0$) the current world average, slightly less precise but still better than a part per billion, of $\alpha = 1/137.035\,999\,084(21)$ [7].

This contrasts with the 7% larger value that is relevant for physics at or around the Z pole. This value can both be measured in collider experiments and predicted from the fine-structure constant using the theoretical knowledge of the renormalization group (RG) running with energy. Choosing to work in the $\overline{\text{MS}}$ scheme, RG running predicts $\hat{\alpha}^{(5)}(M_Z) = 1/127.952(9)$ [7]. Alternatively, an effective coupling can be defined at any time-like momentum transfer q^2 in the *on-shell* scheme,

$$\alpha(q^2) = \frac{\alpha}{1 - \Delta\alpha(q^2)}, \quad (2)$$

in terms of the function $\Delta\alpha(q^2)$. While the leptonic contribution to $\Delta\alpha(q^2)$ can be computed in perturbation theory, the contribution from the quarks at low energies is non-perturbative and encoded in the subtracted HVP function,¹

$$\Delta\alpha_{\text{had}}(q^2) = 4\pi\alpha \text{Re} \bar{\Pi}(q^2), \quad \bar{\Pi}(q^2) = \Pi(q^2) - \Pi(0). \quad (3)$$

The standard approach to determine $\Delta\alpha_{\text{had}}$ proceeds by invoking the optical theorem, which links the HVP function to the R -ratio, i.e. the total hadronic cross section $\sigma(e^+e^- \rightarrow \text{hadrons})$ normalized by $\sigma(e^+e^- \rightarrow \mu^+\mu^-)$, and evaluating a dispersion integral. A compilation of precise experimental data for the R -ratio $R(s)$ as a function of the squared center-of-mass energy $s = q^2$ has been used in the most recent efforts [11–13], resulting in $\Delta\alpha_{\text{had}}^{(5)}(M_Z^2) = 0.027\,66(7)$ [7], which constitutes the main uncertainty in the value of $\alpha(M_Z^2)$.

Lattice QCD allows for an *ab initio*, non-perturbative calculation of $\Delta\alpha_{\text{had}}$ that avoids the dependence on experimental R -ratio data. Since the lattice formulation realizes only space-like

¹The conventional choice of taking the real part of $\bar{\Pi}(q^2)$ and discarding the imaginary part simplifies the conversion between the on-shell scheme and the $\overline{\text{MS}}$ one, given by eq. (10.10) of ref. [7]. However, to define $\alpha(q^2)$ as a physical observable also the subleading imaginary part should be included [5]. See also the discussion around eq. (2.11) in ref. [15]. For space-like $q^2 < 0$ accessible on the lattice, $\bar{\Pi}(q^2)$ is real and there is no issue around the imaginary part.

momenta in a straightforward manner, the link to $\Delta\alpha_{\text{had}}$ is provided by the Adler function $D(Q^2)$ [16], as advocated in refs. [9, 10, 17, 18]. It is defined in terms of the derivative of $\bar{\Pi}(-Q^2)$ with respect to the space-like squared four-momentum $Q^2 = -q^2$ and can also be written as a dispersion integral over the R -ratio, i.e.

$$D(Q^2) = 12\pi^2 Q^2 \frac{d\bar{\Pi}(-Q^2)}{dQ^2} = Q^2 \int_0^\infty ds \frac{R(s)}{(s + Q^2)^2}, \quad (4)$$

On the other hand, the HVP function $\bar{\Pi}(-Q^2)$ can be represented in terms of a current correlator [19–21],

$$(Q_\mu Q_\nu - \delta_{\mu\nu} Q^2) \bar{\Pi}(-Q^2) = \Pi_{\mu\nu}(Q) = \int d^4x e^{iQ \cdot x} \langle j_\mu^\gamma(x) j_\nu^\gamma(0) \rangle, \quad (5)$$

with the electromagnetic current j_μ^γ of the quarks given by

$$j_\mu^\gamma = \frac{2}{3} \bar{u} \gamma_\mu u - \frac{1}{3} \bar{d} \gamma_\mu d - \frac{1}{3} \bar{s} \gamma_\mu s + \frac{2}{3} \bar{c} \gamma_\mu c + \dots \quad (6)$$

The determination of $\Delta\alpha_{\text{had}}$ is closely related to that of the leading HVP contribution to the anomalous magnetic moment of the muon, $a_\mu^{\text{HVP,LO}}$. Both quantities can be evaluated either via a dispersion integral using experimental data for the R -ratio or via a first-principles approach based on a lattice calculation of the HVP function $\bar{\Pi}(-Q^2)$.

The correlation between $\Delta\alpha_{\text{had}}$ and $a_\mu^{\text{HVP,LO}}$ implies that any evaluation of $a_\mu^{\text{HVP,LO}}$ also provides a constraint on $\Delta\alpha_{\text{had}}$. While enormous progress has been achieved in recent years concerning *ab initio* calculations of $a_\mu^{\text{HVP,LO}}$ in lattice QCD [5, 8, 21–29], the current SM estimate is based on dispersion theory using the experimentally measured R -ratio [5, 11, 12, 15, 30–32], which achieves an overall uncertainty at the level of 0.6%. However, the recent lattice determination by BMWc [6], which is the first to claim a level of precision similar to that obtained from the R -ratio, favors a larger value for $a_\mu^{\text{HVP,LO}}$ compared to the phenomenological estimate. While such a higher value for $a_\mu^{\text{HVP,LO}}$ would reduce the tension between the SM and the experimental measurement, it would, via the correlation with $\Delta\alpha_{\text{had}}$, further increase the already observed slight tension with global electroweak fits [33–37]. Recent investigations, considering also the global fit predictions of M_W and the electroweak mixing angle, have concluded that an increase in the values of $a_\mu^{\text{HVP,LO}}$ and $\Delta\alpha_{\text{had}}(M_Z^2)$ is still compatible with global electroweak fits, provided that the R -ratio is enhanced by 9% in the region below ≈ 0.7 GeV [35]. This seems an unlikely possibility, given the high precision that hadronic cross sections have been measured with.

The precise size of the increase on $\Delta\alpha_{\text{had}}(M_Z^2)$ which would correspond to the lattice result in ref. [6] has not been precisely estimated. An independent lattice determination of $\Delta\alpha_{\text{had}}(-Q^2)$ over an interval of Q^2 in the low-energy regime, as described in this paper, can help to resolve this puzzle. We will return to an in-depth discussion of this issue in section 5.

2.2. The electroweak mixing angle

The electroweak sector of the SM is characterized by two gauge couplings, g and g' , for the $SU(2)_L$ weak isospin and $U(1)_Y$ weak hypercharge gauge interactions, respectively. The electromagnetic coupling $\alpha = e^2/(4\pi)$ is a linear combination of g and g' parametrized by the electroweak mixing angle (or Weinberg angle) θ_W defined through [7, 38]

$$e = g \sin \theta_W = g' \cos \theta_W, \quad \sin^2 \theta_W = \frac{g'^2}{g^2 + g'^2}. \quad (7)$$

Just as the couplings in the interacting quantum field theory are renormalization scheme and energy dependent, so is the precise definition of $\sin^2 \theta_W$ beyond tree level. For instance, since the angle enters the W and Z boson mass ratio, which is known precisely from collider experiments, one choice of scheme employs the tree-level formula $\sin^2 \theta_W = 1 - M_W^2/M_Z^2$ to all orders of perturbation theory, which results in the *on-shell* value of $\sin^2 \theta_W = 0.223\,37(10)$ [7]. Another widely used convention is the *effective coupling* $\sin^2 \theta_{\text{eff}}^f$ for the Z -boson coupling to the fermion f , which is an input to the global electroweak fit mentioned in section 2.1. Finally, in the $\overline{\text{MS}}$ definition of $\sin^2 \hat{\theta}_W(\mu)$, one substitutes the $\overline{\text{MS}}$ couplings $\hat{g}(\mu)$, $\hat{g}'(\mu)$ at $\mu = M_Z$ into eq. (7), which gives the sub-permil precision value $\sin^2 \hat{\theta}_W(M_Z) = 0.231\,21(4)$ [7].

There is a growing interest in experiments that probe precision electroweak observables at momentum transfers $q^2 \ll M_Z^2$, such as measurements of cross sections of neutrino scattering and parity-violating lepton scattering, as well as nuclear weak charges in atomic parity violation experiments. These experiments are sensitive to modifications of the RG running of the mixing angle by BSM physics. A q^2 -dependent definition of the mixing angle that is appropriate for low-energy experiments is obtained by applying a form factor $\hat{\kappa}$ to the $\overline{\text{MS}}$ Z -pole value [39–44]

$$\sin^2 \theta_W(q^2) = \hat{\kappa}(q^2, \mu) \sin^2 \hat{\theta}_W(\mu), \quad (8)$$

such that the Thomson limit results in the process-independent physical observable $\sin^2 \theta_W \equiv \sin^2 \theta_W(0)$, the electroweak analog of the fine-structure constant α . The value $\hat{\kappa}(0, M_Z) \approx 1.03$ results in $\sin^2 \hat{\theta}_W = 0.238\,57(5)$, quoted by ref. [7] as the average of different results [42, 44–46], which is 3% larger than the Z -pole value used as input. Excluding uncertainties from experimental input, the error on the theory prediction of $\sin^2 \hat{\theta}_W$ at $q^2 = 0$ is dominated by the non-perturbative hadronic contributions.

Experimental determinations of $\sin^2 \theta_W$ from current low-energy experiments are much less precise [47–49] compared to α , with the current most precise value resulting from the determination of the weak charge of the proton Q_W^p by the Q_{weak} experiment at JLab [50], obtained at $Q^2 = 0.024\,8 \text{ GeV}^2$. However, future new and upgraded experiments have the potential of changing the situation. The P2 experiment at MESA [51], which is expected to start data taking in 2025, targets 0.15% precision on $\sin^2 \theta_W$ at a momentum transfer of $4.5 \times 10^{-3} \text{ GeV}^2$ [51], and the MOLLER and SoLID experiments at JLab have comparable precision goals [52–54].

Following refs. [13, 55–57], the relation between $\sin^2 \theta_W(-Q^2)$ and its value in the Thomson limit can be written as

$$\sin^2 \theta_W(-Q^2) = \left(\frac{1 - \Delta\alpha_2(-Q^2)}{1 - \Delta\alpha(-Q^2)} + \Delta\kappa_b(Q^2) - \Delta\kappa_b(0) \right) \sin^2 \theta_W(0), \quad (9)$$

where the bosonic contribution $\Delta\kappa_b$ is given in ref. [42], $\Delta\alpha$ is the contribution to the running of α in eq. (2) and $\Delta\alpha_2$ is the contribution to the running of the $\text{SU}(2)_L$ gauge coupling $\alpha_2 \equiv g^2/(4\pi)$, defined as

$$\alpha_2(q^2) = \frac{\alpha_2}{1 - \Delta\alpha_2(q^2)}. \quad (10)$$

Similarly to $\Delta\alpha$, $\Delta\alpha_2$ receives the leading hadronic contribution from the HVP mixing function

$$\Delta\alpha_{2,\text{had}}(q^2) = \frac{4\pi\alpha}{\sin^2 \theta_W} \bar{\Pi}^{T_3\gamma}(q^2) \quad (11)$$

of the electromagnetic current j_μ^γ with the vector part of the weak isospin third component T_3 current, i.e.

$$j_\mu^{T_3}|_{\text{vector}} = \frac{1}{4} \bar{u} \gamma_\mu u - \frac{1}{4} \bar{d} \gamma_\mu d - \frac{1}{4} \bar{s} \gamma_\mu s + \frac{1}{4} \bar{c} \gamma_\mu c + \dots \quad (12)$$

At leading order, the hadronic contribution to the running of $\sin^2 \theta_W$ is given by [19, 55, 58]

$$\Delta_{\text{had}} \sin^2 \theta_W(q^2) = \Delta\alpha_{\text{had}}(q^2) - \Delta\alpha_{2,\text{had}}(q^2) = -\frac{4\pi\alpha}{\sin^2 \theta_W} \bar{\Pi}^{Z\gamma}(q^2), \quad (13)$$

where $\bar{\Pi}^{Z\gamma}(q^2)$ is the HVP mixing of the electromagnetic current j_μ^γ and the vector part of the neutral weak current

$$j_\mu^Z|_{\text{vector}} = j_\mu^{T_3}|_{\text{vector}} - \sin^2 \theta_W j_\mu^\gamma. \quad (14)$$

As for the running of α , the standard approach is based on a phenomenological estimate of the hadronic contribution from experimental data [45, 46]. However, $R(s)$ alone is not sufficient in this case, as the total cross section couples only to the electromagnetic current j_μ^γ . The process of assigning individual channels in the hadronic cross section to the different quark flavor contributions, in order to reweight them according to the weak isospin charge factors, is called *flavor separation* and a source of systematic uncertainty.

In the next section we show that $\bar{\Pi}^{Z\gamma}(-Q^2)$ admits a decomposition into valence flavor components that can all be determined directly from suitable correlation functions computable in lattice QCD [19, 20, 59, 60]. This paves the way for *ab initio* estimates that do not rely on experimental cross-section data and a reweighting of individual hadronic channels.

3. Methodology

3.1. The TMR method

The main primary observable that we compute in our lattice QCD simulations is the correlation function, $G_{\mu\nu}(x)$, of two generic vector currents $j_\mu(x)$, defined by $G_{\mu\nu}(x) = \langle j_\mu(x) j_\nu(0) \rangle$. By supplying the appropriate currents, i.e. j_μ^γ or j_μ^Z , we can compute the electromagnetic HVP function $\bar{\Pi}^{\gamma\gamma}$ and its $Z - \gamma$ counterpart $\bar{\Pi}^{Z\gamma}$ as functions of Q^2 in terms of these correlators. In this work, we employ the time-momentum representation (TMR), defined in [61, 62], which has emerged as the standard method to compute the HVP in lattice QCD and which is well suited to open boundary conditions in the time direction, which are employed on a large subset of our gauge ensembles (see section 3.4). For concreteness, we consider the correlator of two electromagnetic currents, $G_{\mu\nu}^{\gamma\gamma} = \langle j_\mu^\gamma(x) j_\nu^\gamma(0) \rangle$. In the continuum and infinite-volume limits, the corresponding subtracted HVP function $\bar{\Pi}^{\gamma\gamma}(-Q^2)$ is given by the integral over Euclidean time

$$\bar{\Pi}^{\gamma\gamma}(-Q^2) = \int_0^\infty dt G^{\gamma\gamma}(t) K(t, Q^2) \quad (15)$$

of the product of the zero-momentum-projected correlator

$$G^{\gamma\gamma}(t) = -\frac{1}{3} \int d^3x \sum_{k=1}^3 \langle j_k^\gamma(t, \vec{x}) j_k^\gamma(0) \rangle \quad (16)$$

multiplied by a Q^2 -dependent kernel function

$$K(t, Q^2) = \left[t^2 - \frac{4}{Q^2} \sin^2 \left(\frac{Qt}{2} \right) \right]. \quad (17)$$

The corresponding integral representation of $\bar{\Pi}^{\gamma Z}(-Q^2)$ is obtained by replacing one of the electromagnetic currents by j_μ^Z . After inserting the definitions of the currents in eqs. (6) and (12) and performing the Wick contractions of the quark fields, one can perform explicit flavor decompositions of both $\bar{\Pi}^{\gamma\gamma}$ and $\bar{\Pi}^{\gamma Z}$, as described in section 3.2.

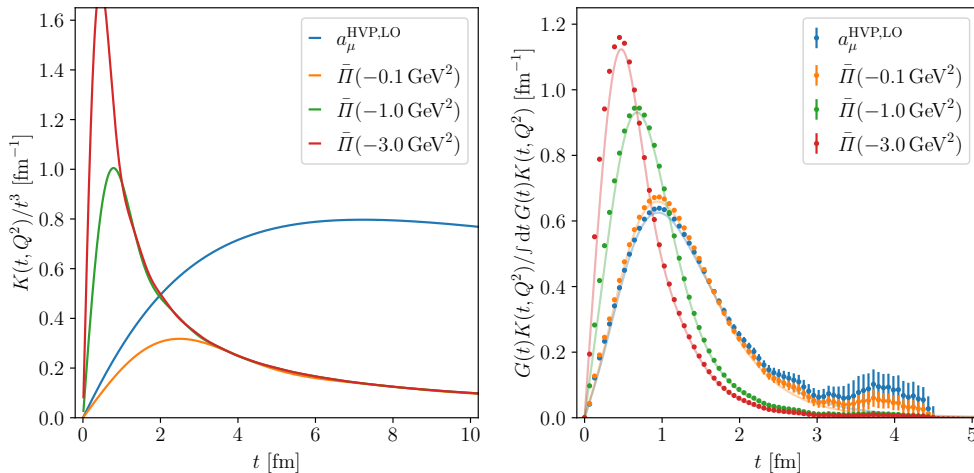


Figure 1: Left: the kernel $K(t, Q^2)$ of the TMR integral in eq. (15) for different values of Q^2 , compared to the kernel $w(t)$ for $a_\mu^{\text{HVP,LO}}$ [61, 63] (blue line), as a function of time t . All kernels are divided by t^3 in the plot, such that they tend to zero at $t \rightarrow \infty$ while being still zero at $t = 0$. Right: contribution of $G(t)K(t, Q^2)$ to the TMR integral normalized to the value of the integral, comparing different kernels. The light colored lines are drawn using a model for the Euclidean-time correlator $G(t)$ [61], that is also used for the integral, while the data points with error bars are obtained using actual lattice correlator data at the physical pion mass.

The properties of the kernel significantly influence the integral and its systematics: In the left panel of figure 1, we plot the kernel function $K(t, Q^2)$ for several different values of Q^2 versus Euclidean time. Also shown is the kernel $w(t)$ that appears in the TMR expression for $a_\mu^{\text{HVP,LO}}$, which is given explicitly in eq. (84) of ref. [61]. Despite the fact that both $K(t, Q^2)$ and $w(t)$ behave like t^2 at long distances, it is evident that $w(t)$ gives a much higher weight to long distances compared to $K(t, Q^2)$. This has several consequences for our calculation: On the one hand, since the signal-to-noise ratio of the vector correlator lattice data degrades severely with time, the stronger suppression of the long-distance contribution by the kernel $K(t, Q^2)$ makes it easier to achieve good statistical precision for $\bar{\Pi}(-Q^2)$ in our range of interest for Q^2 , compared to $a_\mu^{\text{HVP,LO}}$. Moreover, finite-size effects that affect the correlator mostly at long distances are more strongly suppressed by $K(t, Q^2)$ relative to $w(t)$, even though they are still relevant at our target precision, as explained in section 3.7. On the other hand, the peak of the kernel $K(t, Q^2)$ occurs at increasingly short distances t for larger values of Q^2 , which results in larger discretization effects, both from the correlator itself and from the approximation of the integral in eq. (15) as a discrete sum.² Therefore, lattice discretization effects and our ability to estimate and control the associated systematic error ultimately limit the upper end of the range of Q^2 values.

3.2. Flavor decomposition

As already mentioned, the HVP functions $\bar{\Pi}^{\gamma\gamma}$ and $\bar{\Pi}^{Z\gamma}$ differ only in their flavor content. For the following discussion, we assume exact strong-isospin symmetry and neglect charm disconnected

²In this work, we employ the trapezoidal rule to approximate the TMR integral, which has a $\mathcal{O}(a^2)$ error that is consistent with the use of $\mathcal{O}(a)$ -improved action and operators, see section 3.4.

contributions. It is convenient to introduce a strong isospin and SU(3)-flavor basis for the quark triplet $q = (u, d, s)^T$, starting from the vector currents $j_\mu^a = \bar{q}\gamma_\mu(\lambda_a/2)q$ where λ_3, λ_8 are Gell-Mann matrices and $\lambda_0 = \text{Id}_3$,

$$I = 1: \quad j_\mu^3 = \frac{1}{2} (\bar{u}\gamma_\mu u - \bar{d}\gamma_\mu d), \quad (18a)$$

$$I = 0: \quad j_\mu^8 = \frac{1}{2\sqrt{3}} (\bar{u}\gamma_\mu u + \bar{d}\gamma_\mu d - 2\bar{s}\gamma_\mu s), \quad (18b)$$

$$j_\mu^0 = \frac{1}{2} (\bar{u}\gamma_\mu u + \bar{d}\gamma_\mu d + \bar{s}\gamma_\mu s), \quad (18c)$$

such that, with the addition of the charm current $j_\mu^c = \bar{c}\gamma_\mu c$, the currents j_μ^γ and j_μ^Z are represented by

$$j_\mu^\gamma = j_\mu^3 + \frac{1}{\sqrt{3}}j_\mu^8 + \frac{2}{3}j_\mu^c, \quad j_\mu^{T_3}|_{\text{vector}} = \frac{1}{2} \left(j_\mu^\gamma - \frac{1}{3}j_\mu^0 - \frac{1}{6}j_\mu^c \right), \quad (19a)$$

$$j_\mu^Z|_{\text{vector}} = j_\mu^{T_3}|_{\text{vector}} - \sin^2 \theta_W j_\mu^\gamma = \left(\frac{1}{2} - \sin^2 \theta_W \right) j_\mu^\gamma - \frac{1}{6}j_\mu^0 - \frac{1}{12}j_\mu^c. \quad (19b)$$

The correlators of interest are

$$G_{\mu\nu}^{\gamma\gamma}(x) = G_{\mu\nu}^{33}(x) + \frac{1}{3}G_{\mu\nu}^{88}(x) + \frac{4}{9}G_{\mu\nu}^{cc}(x), \quad (20a)$$

$$G_{\mu\nu}^{Z\gamma}(x) = \left(\frac{1}{2} - \sin^2 \theta_W \right) G_{\mu\nu}^{\gamma\gamma}(x) - \frac{1}{6\sqrt{3}}G_{\mu\nu}^{08}(x) - \frac{1}{18}G_{\mu\nu}^{cc}(x), \quad (20b)$$

which can be obtained by computing the building blocks $G_{\mu\nu}^{33}$, $G_{\mu\nu}^{88}$, $G_{\mu\nu}^{08}$ and $G_{\mu\nu}^{cc}$. In this paper we will present as intermediate results, extrapolated to the physical point, the $I = 1$ HVP function \bar{H}^{33} , the $I = 0$ ones \bar{H}^{88} and \bar{H}^{08} , with the latter being relevant for the running of $\sin^2 \theta_W$ case only, and the charm HVP function of \bar{H}^{cc} .

Up to lattice renormalization and $O(a)$ improvement, the flavor SU(3) contributions are defined as³

$$G_{\mu\nu}^{33}(x) = \frac{1}{2}C_{\mu\nu}^{\ell,\ell}(x), \quad (21a)$$

$$G_{\mu\nu}^{88}(x) = \frac{1}{6} [C_{\mu\nu}^{\ell,\ell}(x) + 2C_{\mu\nu}^{s,s}(x) + 2D_{\mu\nu}^{\ell-s,\ell-s}(x)], \quad (21b)$$

$$G_{\mu\nu}^{08}(x) = \frac{1}{2\sqrt{3}} [C_{\mu\nu}^{\ell,\ell}(x) - C_{\mu\nu}^{s,s}(x) + D_{\mu\nu}^{2\ell+s,\ell-s}(x)], \quad (21c)$$

where the flavor labels ℓ and s denote the (isospin averaged) light and strange quarks, respectively, while $C_{\mu\nu}^{f_1,f_2}$ and $D_{\mu\nu}^{f_1,f_2}$ are, respectively, the connected and disconnected Wick contractions, schematically given by

$$C_{\mu\nu}^{f_1,f_2} = - \left\langle \gamma_\mu \begin{array}{c} \xrightarrow{f_1} \\ \xleftarrow{f_2} \end{array} \gamma_\nu \right\rangle, \quad D_{\mu\nu}^{f_1,f_2} = \left\langle \begin{array}{c} \text{circle } f_1 \\ \text{circle } f_2 \end{array} \right\rangle. \quad (22)$$

Section 3.8 explains the lattice computation of the connected and disconnected contractions in more detail.

³In the usual lattice notation, $G_{\text{con}}^\ell = 2G^{33}$ and $G_{\text{con}}^s = 3G_{\text{con}}^{88} - G^{33}$. Moreover, $G_{\text{con}}^{08} = \sqrt{3}(G^{33} - G_{\text{con}}^{88})/2$.

3.3. Renormalization and $\mathcal{O}(a)$ improvement

We use the vector correlators computed in ref. [8], with updated statistics and ensemble coverage as listed in table 1. At the sink, we employ both the local (labeled by the superscript labeled “L”) and conserved discretizations (labelled “C”) of the vector current, i.e.

$$j_\mu^{a,L}(x) = \bar{q}(x)\gamma_\mu \frac{\lambda_a}{2} q(x), \quad (23a)$$

$$j_\mu^{a,C}(x) = \frac{1}{2} \left[\bar{q}(x + a\hat{\mu})(1 + \gamma_\mu)U_\mu^\dagger(x) \frac{\lambda_a}{2} q(x) - \bar{q}(x)(1 - \gamma_\mu)U_\mu(x) \frac{\lambda_a}{2} q(x + a\hat{\mu}) \right], \quad (23b)$$

while only the local current is used at the source. The $\mathcal{O}(a)$ -improvement and renormalization of the vector currents in the flavor basis is complicated by the fact that flavor singlet and non-singlet contributions renormalize differently: it is more convenient to work in the basis introduced in section 3.2. For the local discretization, the renormalized (“R”) currents read [64]

$$j_{\mu,R}^{3,L} = Z_V (1 + 3\bar{b}_V am_q^{\text{av}} + b_V am_{q,\ell}) j_\mu^{3,I,L}, \quad (24a)$$

$$\begin{pmatrix} j_\mu^8 \\ j_\mu^0 \end{pmatrix}_R^L = Z_V \begin{pmatrix} 1 + 3\bar{b}_V am_q^{\text{av}} + b_V \frac{a(m_{q,\ell} + 2m_{q,s})}{3} & (\frac{b_V}{3} + f_V) \frac{2a(m_{q,\ell} - m_{q,s})}{\sqrt{3}} \\ r_V d_V \frac{a(m_{q,\ell} - m_{q,s})}{\sqrt{3}} & r_V + r_V(3\bar{d}_V + d_V) am_q^{\text{av}} \end{pmatrix} \begin{pmatrix} j_\mu^8 \\ j_\mu^0 \end{pmatrix}_I^L, \quad (24b)$$

where the improved (indicated by the label “I”) non-singlet and singlet local currents are

$$j_\mu^{a,I,L} = j_\mu^{a,L} + ac_V^L \tilde{\partial}_\nu \Sigma_{\nu\mu}^a, \quad j_\mu^{0,I,L} = j_\mu^{0,L} + ac_V^L \tilde{\partial}_\nu \Sigma_{\nu\mu}^0, \quad (25)$$

with the antisymmetric tensor current $\Sigma_{\mu\nu}^a = -(1/2)\bar{q}[\gamma_\mu, \gamma_\nu](\lambda_a/2)q$, and the breaking of flavor SU(3) symmetry introduces a mixing between the singlet and non-singlet $I = 0$ components. Here, $m_{q,\ell}$ and $m_{q,s}$ are the bare subtracted light and strange quark masses, with $m_q^{\text{av}} \equiv (2m_{q,\ell} + m_{q,s})/3$ denoting their average, and $\tilde{\partial}_\mu$ is the symmetric lattice derivative. The conserved current is automatically renormalized, and its $\mathcal{O}(a)$ -improved version reads

$$j_{\mu,R}^{a,C} = j_\mu^{a,C} + ac_V^C \tilde{\partial}_\nu \Sigma_{\nu\mu}^a, \quad j_{\mu,R}^{0,C} = j_\mu^{0,C} + ac_V^C \tilde{\partial}_\nu \Sigma_{\nu\mu}^0. \quad (26)$$

We have used the non-perturbative determination of the renormalization and improvement coefficients Z_V , b_V , \bar{b}_V and c_V from ref. [65]. Although a non-perturbative determination of the renormalization coefficient r_V is not available, one can avoid relying on the renormalized singlet local current $j_{\mu,R}^{0,L}$ by inserting the conserved singlet current (and thus j_μ^Z) at the sink. Moreover, f_V and $\bar{c}_V^{C,L}$ are also not known. We set $f_V = 0$ and $\bar{c}_V^{C,L} = c_V^{C,L}$, which is valid up to $\mathcal{O}(g_0^6)$ corrections and introduces a negligible error.⁴ We propagate the error on the renormalization coefficients Z_V , b_V , \bar{b}_V quoted in ref. [65] to our estimate of the renormalized vector correlator. The values of the improvement coefficients are taken as a definition of the $\mathcal{O}(a)$ -improved theory and no error on c_V and \bar{c}_V is propagated. In our continuum extrapolations, described in section 4, we have not found any evidence for residual $\mathcal{O}(a)$ discretization effect.

Since our gauge ensembles do not include a dynamical charm quark, the charm contribution to the vector correlator is computed in the quenched approximation, with the charm-quark mass tuned using the experimental D_s meson mass and the local current renormalized using the mass-dependent Z_V^c , as explained in ref. [8].

3.4. Lattice setup

Our calculations are performed on a set of $N_f = 2 + 1$ ensembles from the Coordinated Lattice Simulations (CLS) initiative [67], with tree-level $\mathcal{O}(a^2)$ -improved Lüscher-Weisz gauge action and

⁴Both f_V and $\bar{c}_V^{C,L} - c_V^{C,L}$ arise from disconnected diagrams in which at least three gluons are exchanged. Thus, in perturbation theory this contribution is of $\mathcal{O}(g_0^6)$, see the discussion after eq. (27) in ref. [65].

	T/a	L/a	t_0^{sym}/a^2	a [fm]	L [fm]	m_π, m_K [MeV]	$m_\pi L$	ncfg (con., dis.)			
H101	96	32	2.860	0.086	2.8	415	5.8	2 000	-		
H102	96	32			2.8	355	440	5.0	1 900	1 900	
H105	96	32			2.8	280	460	3.9	1 000	1 000	
N101	128	48			4.1	280	460	5.8	1 155	1 155	
C101	96	48			4.1	220	470	4.6	2 000	2 000	
B450	64	32	3.659	0.076	2.4	415	5.1	1 600	-		
S400	128	32			2.4	350	440	4.3	1 720	1 720	
N451	128	48			3.7	285	460	5.3	1 000	1 000	
D450	128	64			4.9	215	475	5.3	500	500	
H200	96	32	5.164	0.064	2.1	420	4.4	1 980	-		
N202	128	48			3.1	410		6.4	875	-	
N203	128	48			3.1	345	440	5.4	1 500	1 500	
N200	128	48			3.1	285	465	4.4	1 695	1 695	
D200	128	64			4.1	200	480	4.2	2 000	1 000	
E250	192	96			6.2	130	490	4.1	485	485	
N300	128	48			8.595	0.050	2.4	420	5.1	1 680	-
N302	128	48					2.4	345	460	4.2	2 190
J303	192	64	3.2	260			475	4.2	1 040	1 040	
E300	192	96	4.8	175			490	4.3	600	600	

Table 1: List of CLS ensembles employed in this work, with approximate lattice spacings, spatial volume and pion and kaon masses. All ensembles realize open boundary conditions in time, except for B450, D450 and E250 on which the temporal boundary conditions are periodic. Values of t_0^{sym} and a are taken from ref. [66]. The number of configurations used for connected and disconnected vector correlator measurements is listed in the last two columns.

non-perturbatively $\mathcal{O}(a)$ -improved Wilson fermions [68]. A list of ensembles is shown in table 1. While boundary conditions (BCs) in the spatial directions are always periodic, most ensembles are characterized by open BCs in the time direction, which alleviates the issue of topological charge freezing at small lattice spacings [69]. Only ensembles B450, D450, and E250 are characterized by periodic (anti-periodic for fermions) BCs in time. We use four lattice spacings, ranging from $a \approx 0.086$ fm to ≈ 0.050 fm. The masses of the u and d quarks are taken to be degenerate in the calculation, and the pseudoscalar meson masses span the interval from $m_\pi = m_K \approx 415$ MeV at the SU(3)-symmetric point to the physical ones along a trajectory on which the sum of the bare u , d and s quark masses is kept constant. We set the scale using the value of the gradient flow scale t_0 [70], which has been determined as $(8t_0^{\text{phys}})^{1/2} = 0.415(4)(2)$ fm in ref. [66], using the pion and kaon decay constants.

The ensembles have been generated with a small twisted mass applied to the light quark doublet for algorithmic stability. The correct $N_f = 2 + 1$ QCD expectation values are obtained after including the reweighting factors for the twisted mass and for the RHMC algorithm used to simulate the strange quark, inclusive of the sign of the latter [71]. A negative reweighting factor associated with the simulation of the strange quark is found on less than 0.5% of the total gauge field configurations employed in this work, and on 3.6% of the configurations of C101, the most affected ensemble. The numerical impact of including the sign of the reweighting factor on the HVP function \bar{H} and on the meson masses is negligible with respect to the statistical error. On

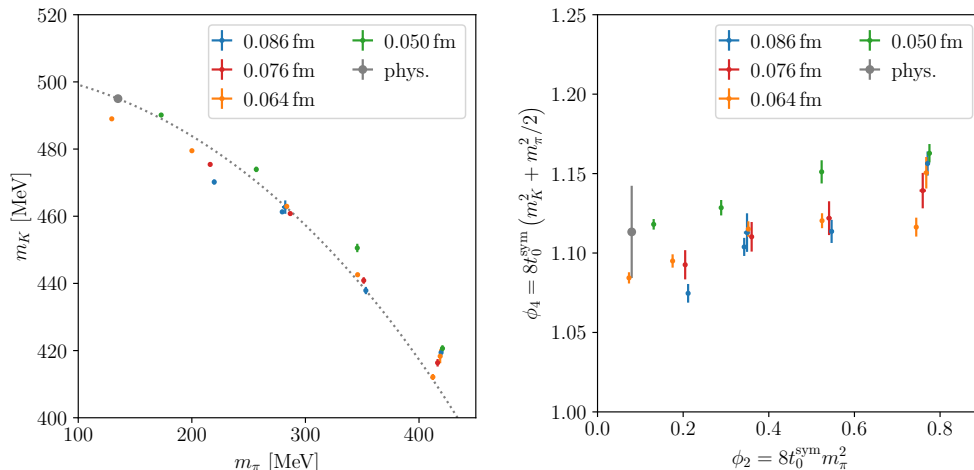


Figure 2: Landscape of the ensembles from the CLS initiative employed in this work.

the most affected ensembles, a few percent increase in the statistical error is observed, compatible with the loss in statistics due to the negative weight of some configurations. A few ensembles that had a larger fraction of configurations with negative weight were excluded entirely from this work.

In this work we use the connected Wick contractions of the vector-current two-point function that has been computed in ref. [8], albeit with significantly increased statistics, especially on the ensembles closer to the physical point. For more details on the connected correlator computation, we refer to ref. [8].

3.5. Quark-disconnected diagrams

The determination of quark-disconnected contributions (see eq. (22)) requires the evaluation of quark loops

$$L_{\mathcal{O}_f}(\vec{p}, t) = \sum_{\vec{x}} e^{i\vec{p}\cdot\vec{x}} \langle \mathcal{O}_f(\vec{x}, t) \rangle_F, \quad (27)$$

for some operator $\mathcal{O}_f(\vec{x}, t)$ involving a single quark flavor f , where $\langle \dots \rangle_F$ denotes the fermionic expectation value (in a given gauge-field background). Our computation of quark-disconnected loops has been performed using a variant of the method introduced in ref. [72] combining the one-end trick (OET) [73] which is commonly used with twisted-mass fermions [73–75] with a combination of the generalized hopping parameter expansion (gHPE) [76] and hierarchical probing (HP) [77]. The difference of two quark-disconnected loops can be written as a product

$$\text{tr}[\Gamma(D_1^{-1} - D_2^{-1})] = (m_2 - m_1) \text{tr}[\Gamma D_1^{-1} D_2^{-1}], \quad (28)$$

where D_f^{-1} denotes the inverse of the Dirac operator for a given quark flavor labeled $f = 1, 2$ with masses $m_1 \neq m_2$ and Γ is the desired combination of Dirac matrices. The OET yields a very efficient estimator of the r.h.s. of eq. (28) by inserting all-volume stochastic noise at the “one end” of the trace of the product $\Gamma D_1^{-1} D_2^{-1}$, where the identity (one) matrix in Dirac space is inserted. This estimator has a lower variance than the standard one that inserts the noise at the “ Γ end” of either side of eq. (28) [72], see appendix C for more details. In order to derive estimators for loops of a single, individual quark flavor, an efficient scheme has been proposed in

ref. [72] that relies on computing the OET estimator for a chain of $f = 1, \dots, N$ different quark flavors with $m_1 < m_2 < \dots < m_N$ and evaluating the single flavor trace for the heaviest flavor explicitly, from which it is possible to recursively reconstruct single-flavor traces for all other quark flavors. To this end, the hopping parameter expansion is used, which is known to be very efficient at large quark masses. It is based on a decomposition of D_N^{-1} into two terms [72]

$$D_N^{-1} = M_{2n,m} + D_N^{-1} H_m^{2n}, \quad (29)$$

where

$$M_{2n,m} = \frac{1}{D_{ee} + D_{oo}} \sum_{i=0}^{2n-1} H_m^i, \quad H_m = -(D_{eo} D_{oo}^{-1} + D_{oe} D_{ee}^{-1}), \quad (30)$$

and $D_{ee}, D_{eo}, D_{oe}, D_{oo}$ denote the blocks of the even-odd decomposition of the Dirac operator. In ref. [72] a probing scheme has been introduced that yields an exact result for the (sparse) first term in eq. (29) for disconnected loops involving local operators. However, since we are also interested in computing observables involving point-split currents, a more general method is required. Therefore, we evaluate the first term, $M_{2n,m}$, using hierarchical probing on spin and color diluted stochastic volume sources. For the second term it is sufficient to use naive stochastic volume sources, and the required inversion can be reused in the evaluation of $\text{tr}[\Gamma(D_{N-1}^{-1} - D_N^{-1})]$, i.e. the last term of the chain of OET estimators.

We find that this method is significantly more efficient than e.g. plain hierarchical probing, which we have applied in previous studies in refs. [8, 78]. For the local and conserved vector currents, which are of interest for the present study, a minor reduction in the resulting errors is already observed for the case of a single light quark, while a much more significant improvement is observed when the OET is applied to the $l - s$ combination. In the case of the conserved vector current, the errors from the plain hierarchical probing with 512 Hadamard vectors on two stochastic volume sources exceeds the one from the (OET+gHPE+HP)-based method by a factor of ≈ 2 , indicating that even with 512 Hadamard vectors the gauge noise had not nearly been reached for this observable. Using OET estimators, we reach the gauge noise for all the disconnected quark loops relevant to this work. However, even more striking is the difference in computational cost which is improved by at least a factor five.

Within this study we observe a large gain in precision on the disconnected contribution to \bar{I}^{88} , since it is the product of two λ_8 currents that requires the estimation only of the first loop difference, proportional to $m_s - m_\ell$. The disconnected contribution to \bar{I}^{08} instead has only one factor of λ_8 , and another factor of the SU(3)-singlet current that requires the evaluation of the full telescopic sum and is inherently more noisy. This is clearly visible in the different size of the error band of the two disconnected contributions in figure 5.

Finally, we remark that the disconnected contribution to both HVP functions considered here vanishes for $m_s = m_\ell$, i.e. at the SU(3)-symmetric point.

3.6. Signal-to-noise ratio and bounding method

The vector correlator is affected by the well-known exponential deterioration of the signal-to-noise ratio (S/N) with Euclidean time t [79, 80]. In the case of the connected contribution, the S/N deteriorates roughly like $\exp\{-(E_0 - m_\pi)t\}$, where E_0 is the lowest energy level in the vector channel. The problem worsens at lower pion masses. Moreover, for the quark-disconnected contribution, the statistical error is independent of the source-sink separation. This is significant, since the kernel $K(t, Q^2)$ behaves like t^2 at long distances. In order to have a bounded error on the disconnected contribution to the vector correlator it is necessary to truncate the TMR integration, if one wants to avoid having to increase the Monte Carlo (MC) sampling statistics exponentially with time. Solving the S/N problem is an active field of research. One promising

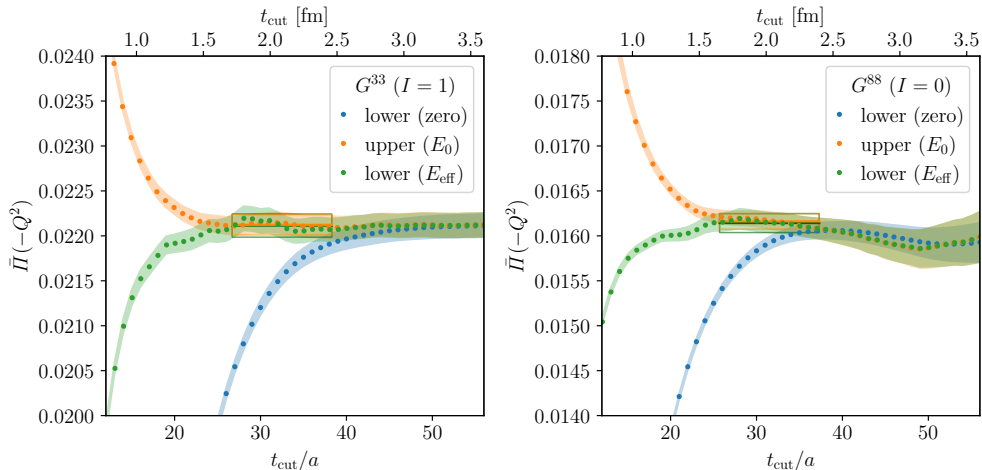


Figure 3: Bounding method on the $I = 1$ (left) and $I = 0$ (right) components for ensemble D200 at $Q^2 = 0.5 \text{ GeV}^2$. The upper bound (orange points and band) is chosen as the ground state obtained from the finite volume analysis (left) or as the ρ meson mass (right). The lower bound (green points and band) is computed using the effective mass at every time slice. The time slices on which the upper and lower bound are averaged are indicated by the limits of the average lines and error boxes. The less stringent lower bound given by the integral truncated up to t is also given (blue points and band).

direction is *multi-level* MC sampling [81–85] which has recently been applied to the closely related problem of computing the HVP contribution to $(g - 2)_\mu$ [86]. To use multi-level MC sampling efficiently, it is crucial that the estimators of connected and disconnected diagrams are in a regime dominated by the gauge noise. As explained in section 3.5, this is indeed the case for disconnected diagrams calculated using the OET estimator. In turn, this strengthens the case for improving the estimator of connected diagrams to reach the gauge noise, as a first step towards a future application of multi-level MC methods.

The *bounding method* has established itself as the primary method to alleviate the S/N problem in HVP computations using the TMR [21, 24, 87]. The method consists of substituting the correlator $G(t)$ at $t > t_{\text{cut}}$ with $G(t_{\text{cut}})$ multiplied by an exponential function that decays with the time distance. By giving the appropriate exponents to this product, we can obtain either a lower or an upper bound of the correlator,

$$0 \leq G(t_{\text{cut}})e^{-E_{\text{eff}}(t_{\text{cut}})(t-t_{\text{cut}})} \leq G(t) \leq G(t_{\text{cut}})e^{-E_0(t-t_{\text{cut}})}, \quad t \geq t_{\text{cut}}, \quad (31)$$

with the effective mass $aE_{\text{eff}}(t) = \log(G(t)/G(t+a))$ and the ground state in a given channel E_0 . Once both bounds are saturated within errors, the corresponding estimate HVP contribution can be computed as a function of t_{cut} . An improved estimate of the HVP function is obtained by averaging both bounds over an interval of about 0.8 fm in t_{cut} , starting from a timeslice where the two innermost bounds coincide at least within half the combined uncertainty. An example is given in figure 3 for the $I = 1$ and $I = 0$ components. We select the bounding method interval for fixed $Q^2 = 0.5 \text{ GeV}^2$, where, as noted in section 3.1, the weight of the correlator tail is relatively high, and use the same interval at all Q^2 values, since the results depend only weakly on Q^2 .

A dedicated spectroscopy analysis that yields the energy levels in finite volume is not available for all ensembles used in this work. In the absence of a precise estimate for E_0 , we note that any

energy level $\leq E_0$ provides a valid, albeit less stringent upper bound. Thus, when applying the bounding method, we may supply any realistic estimate for E_0 , as long as it does not exceed the true ground state energy. Our specific values of E_0 depend on the isospin and ensemble studied. In the $I = 1$ channel $\bar{\Pi}^{33}$, we substitute either the ρ meson mass m_ρ or the two-pion state $E_{\pi\pi}$ for E_0 , depending on the pion mass and box size of the ensemble. Their respective estimates are obtained from our finite-size effects analysis. For some ensembles we can employ the spectroscopy computation of ref. [88] to obtain a precise estimate of m_ρ while keeping our own bootstrap distribution to propagate the errors correctly. The ensembles where $E_{\pi\pi}$ is the ground state are C101, D200, E250 and E300. We could confirm that the two-pion state used is lighter than its non-interacting counterpart $2\sqrt{m_\pi^2 + (2\pi/L)^2}$.

When applying the bounding method to the $I = 0$ contribution $\bar{\Pi}^{88}$, we have identified E_0 with m_ρ , which is motivated by several observations. First, since $m_\rho \lesssim m_\omega$, this is a more conservative choice. Second, while we have computed the $I = 0$ correlator including quark-disconnected diagrams on some ensembles, the results are too noisy for applying the finite-volume analysis to determine the spectrum. Thirdly, while we could also consider the lightest three-pion state with vector isoscalar quantum numbers in the non-interacting case [89], i.e.

$$E_{3\pi} = 2\sqrt{m_\pi^2 + (2\pi/L)^2} + \sqrt{m_\pi^2 + 2(2\pi/L)^2}. \quad (32)$$

we find that $m_\rho < E_{3\pi}$ on our ensembles, mainly due to the extra energy coming from the momenta needed to get the correct quantum numbers.

While the effective mass E_{eff} that provides the lower bound can be obtained from the asymptotic behavior of the correlator, its determination is hampered by the S/N problem at long distances. In these cases we substitute it by the effective mass computed on a earlier timeslice, which is in fact larger and therefore a more conservative choice.

Besides the $\bar{\Pi}^{33}$ and $\bar{\Pi}^{88}$ contributions, we apply the method to the quark-connected $\bar{\Pi}_{\text{con}}^{88}$, assuming that asymptotically it behaves like the $\bar{\Pi}^{33}$ contribution. This allows us to obtain a more precise estimate of the quark-disconnected contribution $\bar{\Pi}_{\text{dis}}^{88}$, by subtracting the bounding method estimate of $\bar{\Pi}_{\text{con}}^{88}$ from the one of $\bar{\Pi}^{88}$.

It is possible to apply the bounding method also to the $\bar{\Pi}^{08}$ contribution, with some additional caveats. Indeed, the G^{08} correlator does not have the positive-definite spectral representation that is needed for eq. (31) to be valid in general. We know, however, that G^{08} has the same E_0 as G^{88} and that the corresponding amplitude a_0 is positive. Furthermore, the correlator G^{08} approaches its asymptotic behavior $\sim a_0 \exp\{-E_0 t\}$ from below. Likewise, E_{eff} approaches E_0 from below. It follows that, for any $t \geq t_{\text{cut}}$, the correlator $G^{08}(t)$ is bounded by $G^{08}(t_{\text{cut}})e^{-E_{\text{eff}}(t_{\text{cut}})(t-t_{\text{cut}})}$ and $G^{08}(t_{\text{cut}})e^{-E_0(t-t_{\text{cut}})}$ from above and below, respectively, which is opposite to eq. (31). We exploit this fact to apply the bounding method to the $\bar{\Pi}^{08}$ contribution, choosing to average the bounds in the same interval of t_{cut} values used for $\bar{\Pi}^{88}$, which, as direct inspection shows, is a conservative choice. Similarly to the case of $\bar{\Pi}^{88}$, we apply the bounding method also to the connected contribution $\bar{\Pi}_{\text{con}}^{08}$ and, after taking the difference with $\bar{\Pi}^{08}$, obtain a more precise estimate of $\bar{\Pi}_{\text{dis}}^{08}$.

Finally, we note that the charm correlator does not require any specific treatment of the tail since it has a very fast exponential decay and higher precision. The pion masses and energy levels that enter the bounding method are listed for each ensemble in table 2.

3.7. Correction for finite-size effects

Lattice QCD simulations are performed in a periodic box of finite volume L^3 and finite Euclidean time extent T . In order to obtain reliable estimates for $\Delta\alpha_{\text{had}}$, the results must be corrected for finite-size effects. The leading effect is a shift of the vector correlator that, for the volumes

	am_π	$aE_{2\pi}$	$aE_{3\pi}$	am_ρ	m_ρ/m_π	$g_{\rho\pi\pi}$
H101	0.183 6(5)	0.537 6(7)	0.870 4(9)	0.375(2)	2.04(1)	4.81(2)
H102	0.154 6(6)	0.499 8(7)	0.817 6(10)	0.358(3)	2.32(2)	4.85(4)
H105	0.123 5(13)	0.463 9(14)	0.767 9(19)	0.338(11)	2.74(9)	5.00(19)
N101	0.122 4(5)	0.358 4(6)	0.580 3(9)	0.340(4)	2.78(4)	4.91(6)
C101	0.096 2(6)	0.324 8(8)	0.533 5(11)	*0.326(3)	3.48(4)	4.81(4)
B450	0.161 1(4)	0.507 9(6)	0.829 0(8)	0.337(1)	2.09(1)	4.82(1)
S400	0.135 9(4)	0.477 6(5)	0.786 8(7)	0.312(4)	2.29(3)	5.02(5)
N451	0.110 9(3)	0.343 1(4)	0.558 9(5)	0.302(4)	2.73(4)	4.97(7)
D450	0.083 6(4)	0.257 9(5)	0.420 0(7)	0.303(8)	3.63(10)	4.72(19)
H200	0.136 3(5)	0.478 1(5)	0.787 4(8)	0.286(3)	2.10(2)	4.86(4)
N202	0.134 2(3)	0.375 0(4)	0.603 6(6)	0.280(3)	2.08(2)	4.87(6)
N203	0.112 7(2)	0.345 4(3)	0.562 1(4)	*0.268(1)	2.39(2)	4.91(4)
N200	0.092 3(3)	0.320 4(3)	0.527 3(4)	*0.252(2)	2.82(5)	4.92(9)
D200	0.065 1(3)	0.235 7(3)	0.389 0(4)	*0.250(2)	3.92(5)	4.86(5)
E250	0.042 2(3)	0.155 7(3)	0.257 4(4)	*0.251(4)	5.74(13)	4.99(9)
N300	0.106 2(2)	0.337 1(3)	0.550 5(4)	0.222(3)	2.09(3)	4.98(6)
N302	0.087 2(3)	0.314 6(4)	0.519 3(5)	0.216(3)	2.47(4)	4.96(9)
J303	0.064 8(2)	0.235 3(2)	0.388 5(3)	*0.200(2)	2.99(4)	5.12(7)
E300	0.043 7(2)	0.157 4(2)	0.259 7(2)	0.198(2)	4.54(5)	4.77(2)

Table 2: From left to right, label of the CLS ensemble, pion mass, energy of the two- and three-pion non-interacting finite-volume states, and rho meson mass used in the bounding method. $E_{3\pi}$ is obtained employing eq. (32). The estimate of m_ρ is obtained from a fit to the local-local discretization of the correlator G^{33} as described in section 3.7.1, except when a value is available from a dedicated study [88]. In this case, the entry is marked by an asterisk (see also table VII in ref. [8]). In the last two columns we list m_ρ/m_π and $g_{\rho\pi\pi}$ which serve as input parameters for the Gounaris-Sakurai model used in the MLL-GS method to correct for finite-size effect. For this purpose, we always use the parameters obtained from the fit to G^{33} .

and pion masses considered here, is of order $\exp\{-m_\pi L\}$ and dominated by the $\pi\pi$ channel. It follows that the $I = 1$ contribution $\bar{\Pi}^{33}$ is mostly affected by finite-size effects. To correct for this, we follow a strategy similar to ref. [8, 62, 63]. To this end, we compute the difference between the $I = 1$ vector correlator in infinite and finite volume as a function of Euclidean time t . Depending on the value of t in physical units, different methods are considered to determine the finite-size correction reliably.

The $\pi\pi$ contribution to the $I = 1$ vector correlator can be computed in chiral perturbation theory (χ PT), both in finite and infinite volume. In our earlier works [8, 63, 90], we used χ PT at next-to-leading order (NLO) to correct the correlator at short Euclidean times for finite-size effects, applying the formula given in eq. (C.4) of ref. [63] (see also ref. [62]). This very simple model corresponds to the correction from noninteracting pions and is known to only account for a fraction of the finite-volume correction to $\bar{\Pi}(-Q^2)$ at Q^2 values of $\mathcal{O}(1 \text{ GeV}^2)$ [91]. A better estimate of the correction can be obtained using χ PT at next-to-next-to-leading order (N²LO) [28, 92], or using the Hansen-Patella (HP) method described in section 3.7.2. We choose to employ the latter for the finite-size correction on the correlator at short time distances. For the correction at long time distances, we use either the HP method or the same method as in refs. [8, 63], described

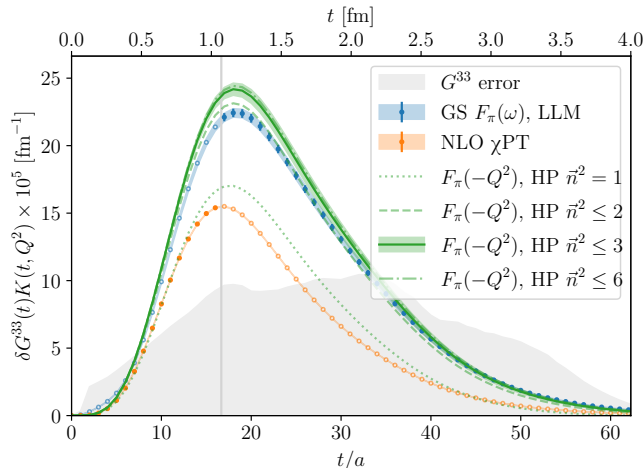


Figure 4: Comparison of the TMR integral at $Q^2 = 1 \text{ GeV}^2$ of the finite-size correction to the G^{33} correlator on the D200 ensemble as a function of the TMR integration time. The MLL-GS method discussed in section 3.7.1 (blue points and band) agrees well with the HP method discussed in section 3.7.2 (green line and band), while the NLO χ PT result using eq. (C.4) from ref. [63] (orange points and line) underestimates the finite-size correction except at very short time distances. The vertical gray line is at $t_i = (m_\pi L/4)^2/m_\pi$. For comparison, the gray shaded area indicates the statistical error on the G^{33} correlator.

in the next section.

3.7.1. Meyer-Lellouch-Lüscher formalism with Gounaris-Sakurai parametrization

An accurate description of the finite-size correction on the correlator tail is obtained making use of a more realistic model for the time-like pion form factor $F_\pi(\omega)$. In infinite volume the $\pi\pi$ contribution to the $I = 1$ correlator has the spectral function representation [93, 94]

$$G^{33}(t, \infty) = \int_0^\infty d\omega \omega^2 \rho(\omega^2) e^{-\omega t}, \quad \rho(\omega^2) = \frac{1}{48\pi^2} \left(1 - \frac{4m_\pi^2}{\omega^2}\right)^{\frac{3}{2}} |F_\pi(\omega)|^2, \quad (33)$$

while the finite volume correlator is a sum of exponentials

$$G^{33}(t, L) = \sum_n |A_n|^2 e^{-\omega_n t}, \quad (34)$$

with the finite-volume energies ω_n and amplitudes A_n . In ref. [95] it was realized that the amplitudes A_n are proportional to the timelike pion form factor $F_\pi(\omega)$, with the proportionality given by a Lellouch-Lüscher factor [96, 97]. Thus, knowledge of the pion form factor allows one to work out the finite-size correction. As in our earlier work [8, 63], we use the Gounaris-Sakurai (GS) parametrization [98] of $F_\pi(\omega)$, which depends on only two parameters m_ρ/m_π and $g_{\rho\pi\pi}$, and refer to this approach as the Meyer-Lellouch-Lüscher Gounaris-Sakurai (MLL-GS) method. The two parameters are determined empirically from a fit to our correlator data. In the absence of a better way to isolate its $\pi\pi$ contribution, we restrict the fit to the tail of the correlator, and we

cut off, using a smoothed step function, the spectral function representation in eq. (33) at some energy corresponding to the inelastic threshold. Correspondingly, the sum over Lüscher energies and Lellouch-Lüscher amplitudes in eq. (34) is limited to the same cut-off energy. Non-elastic interactions become important around the heuristic value $m_\rho + m_\pi$ [61], which we use in the smooth cut-off function. The parameters that we obtain in this way are tabulated in table 2.

We emphasize that we do not assume that the GS parametrization can be used to accurately model the tail of the correlator. Instead, we use the model only to correct for the relatively small finite-volume effect on the correlator. In the future, we plan to further reduce the model dependence, employing, where available, a full lattice determination of $F_\pi(\omega)$ [88, 99] instead of the GS parametrization. The $F_\pi(\omega)$ -based model provides a good spectral representation of the correlator up to the inelastic threshold, thus we use it for the correlator correction at $t > t_i$, with $t_i = (m_\pi L/4)^2/m_\pi$, as in refs. [8, 63].

3.7.2. Hansen-Patella method

An alternative method to correct for the finite-size effect on the correlator has been proposed by Hansen and Patella [100, 101]. Here the leading finite-volume effects are determined to all orders with respect to the interactions of a generic, relativistic effective field theory of pions. Their result is an expansion in the squared momentum vector, $|\vec{n}|^2 = 1, 2, 3, 6, \dots$, with each term of order $\exp\{-|\vec{n}|m_\pi L\}$, and the first neglected effect arising from a sunset diagram of order $\exp\{-\sqrt{2 + \sqrt{3}}m_\pi L\} \approx \exp\{-1.93m_\pi L\}$. The coefficient of each term in the expansion is given by the forward Compton amplitude of the pion, which is decomposed into a pole and a regular piece. Following ref. [101], the dominant contribution is coming from the pole, and is expressed in terms of the electromagnetic form factor $F(-Q^2)$ of the pion in the spacelike region $Q^2 > 0$. In this work, we model the latter using the monopole representation that describes the data in ref. [102],

$$F(-Q^2) = \frac{1}{1 + Q^2/M^2(m_\pi^2)}, \quad M^2(m_\pi^2) = 0.517(23) \text{ GeV}^2 + 0.647(30) m_\pi^2, \quad (35)$$

albeit in $N_f = 2$ QCD. The remaining regular piece, which is independent of the pion form factor, is at most 1% of the pole contribution and can be safely neglected. As in the case of the MLL-GS method, this relatively crude modelling is sufficient, given that it is only used to estimate the finite-size correction.

While the expansion converges to the leading-order finite-size correction to the correlator at any Euclidean time t , the convergence is faster at short time distances. Therefore, we use the sum of the first three terms, $\vec{n}^2 = 1, 2$ and 3 , to estimate the finite-size correction to the TMR integrand for either the whole t -range, or for $t < t_i$. The $\vec{n}^2 = 3$ term is the last term that we can compute that is parametrically larger than the unknown sunset diagram contribution, and its size is thus taken as a conservative systematic error from the series truncation. This has a comparable size to the statistical error from our measurement of m_π .

The finite-size correction to the TMR integrand of $\vec{H}^{33}(1 \text{ GeV}^2)$ on the D200 ensemble as a function of t is shown in figure 4 for the three different methods considered here, including the HP partial series for different values of $|\vec{n}|$, and compared to the statistical error on the $I = 1$ correlator multiplied by the TMR kernel. It is important to recall that the MLL-GS and HP methods rely on very different input for the pion form factor in the time-like and space-like regimes, respectively. Thus, the good agreement between the MLL-GS approach and the HP method for $\vec{n}^2 \leq 3$, especially for $t \gtrsim 2 \text{ fm}$ demonstrates the robustness of the evaluation of finite-volume corrections based on these two procedures. By contrast, the correction obtained from χ PT is significantly smaller. The integral of the correction, at $Q^2 = 1 \text{ GeV}^2$, computed using χ PT, the HP method and the MLL-GS approach is listed for each ensemble in table 3. Regarding

$\times 10^5$	χ PT	whole t range		t_i [fm]	$t < t_i$	$t > t_i$	combined
		HP	MLL-GS				
H101	3.37	12.0(5)	10.5(2)	1.01	4.91(10)	5.7(1)	11.3(1.6)
H102	8.23	26.9(1.4)	23.9(5)	0.85	6.44(18)	17.5(4)	25.4(3.4)
H105	21.30	61.6(5.0)	57.3(3.2)	0.68	6.74(36)	50.7(3.1)	59.5(5.6)
N101	4.27	8.6(3)	8.2(2)	1.52	5.38(15)	2.9(1)	8.5(5)
C101	13.78	25.2(1.4)	23.9(7)	1.20	9.29(34)	15.1(5)	24.8(1.6)
B450	6.10	24.3(1.1)	21.0(4)	0.79	4.72(11)	16.1(3)	22.5(3.8)
S400	13.37	49.8(3.0)	45.6(1.2)	0.66	6.22(21)	39.1(1.1)	47.6(5.2)
N451	6.79	15.2(6)	14.1(3)	1.22	6.77(16)	7.6(2)	14.8(1.2)
D450	7.34	12.2(5)	11.6(3)	1.63	6.66(21)	5.0(2)	11.9(7)
H200	11.36	59.9(3.7)	49.3(1.1)	0.56	4.81(17)	44.2(1.0)	54.4(12.2)
N202	2.11	6.6(2)	5.8(1)	1.24	3.57(8)	2.3(1)	6.2(8)
N203	5.70	16.2(7)	14.3(2)	1.04	5.78(13)	8.7(2)	15.3(2.1)
N200	14.40	37.1(2.2)	33.5(8)	0.85	6.94(23)	26.7(7)	35.4(4.1)
D200	20.73	36.1(2.4)	34.1(6)	1.07	10.26(39)	24.6(4)	35.5(2.3)
E250	25.26	31.7(2.5)	34.1(8)	1.56	11.11(50)	22.3(6)	32.6(2.7)
N300	6.34	26.4(1.2)	22.5(6)	0.76	4.75(11)	17.6(5)	24.4(4.5)
N302	15.37	58.2(3.8)	48.2(1.4)	0.62	5.96(22)	42.2(1.3)	53.2(11.4)
J303	19.16	45.3(3.1)	42.6(1.0)	0.83	8.38(32)	34.5(9)	44.1(3.3)
E300	21.17	32.3(2.2)	31.3(4)	1.25	10.42(40)	21.4(3)	32.1(1.6)

Table 3: Finite-size corrections to the $I = 1$ HVP function $\bar{\Pi}^{33}(-Q^2) \times 10^5$ at $Q^2 = 1 \text{ GeV}^2$ for each individual gauge ensemble. Columns 2–4 show the finite-size effects estimated using NLO χ PT, the Hansen-Patella (HP) method and the Meyer-Lellouch-Lüscher Gounaris-Sakurai (MLL-GS) formalism, respectively. In the following columns we list the corrections for time distances shorter than t_i , estimates using the HP method, as well as for distances greater t_i obtained via the MLL-GS formalism. In the last column we specify the chosen combination to correct for finite-size effects on $\bar{\Pi}^{33}$, obtained from the HP method at $t < t_i$, and the average of the HP and MLL-GS values, with the difference added to the error as an additional systematic, at $t > t_i$.

the finite-size correction over the whole range of t , one observes that the MLL-GS and the HP methods produce similar results, while the χ PT estimates are between 25–75% of the other two. With this in mind, we define our best estimate for the correction of the finite-volume effects of $\bar{\Pi}^{33}$ in the following way: for short time distances ($t <$) we use the HP-method estimate, for long time distances ($t >$) we take the average between the HP-method and MLL-GS values including the difference between the two as an additional source of systematic error, added in quadrature. The χ PT estimate is not used at all. These short- and long-distance corrections are given for each ensemble in table 3, with our best estimate in the last column.

We can directly test the reliability of the finite-size corrections, by comparing the predictions of the MLL-GS and HP models to results obtained for two different volumes at otherwise identical simulation parameters. The corresponding pairs of ensembles are H105 and N101 (at $m_\pi \approx 280 \text{ MeV}$), as well as H200 and N202 (at the SU(3)-symmetric point). For both sets, we confirmed that the TMR integral contribution, which clearly differs before correcting for finite-size effects, agrees within errors after the correction is applied.

We do not correct for subleading finite-size effects in the $I = 0$ contributions $\bar{\Pi}^{88}$ and $\bar{\Pi}^{08}$,

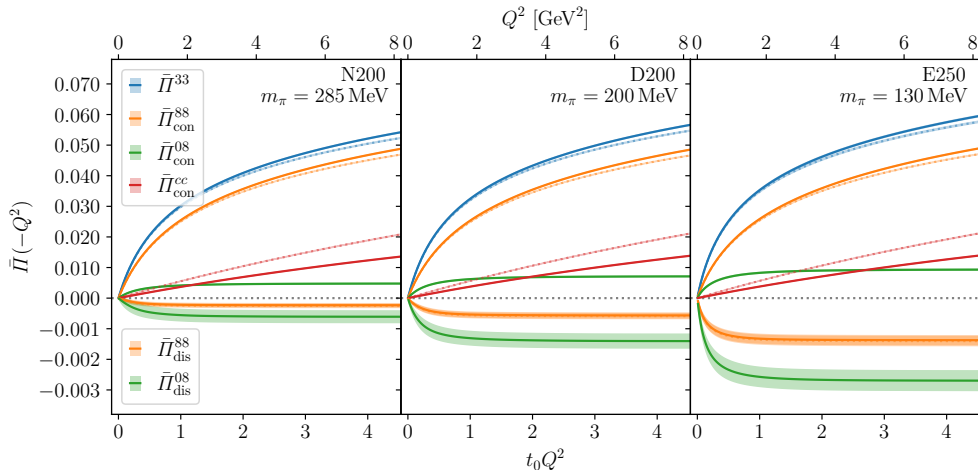


Figure 5: Running with energy Q^2 of different contributions to $\bar{\Pi}(-Q^2)$ on three different ensembles at $a \approx 0.064$ fm. The conserved-local discretization is shown and, when available, the local-local discretization in a lighter color shade. The negative side of the vertical axis of the plot is inflated by a factor 10 with respect to the positive side.

except for the case of SU(3)-symmetric ensembles, where $\bar{\Pi}^{88}$ and $\bar{\Pi}^{33}$, and thus the respective finite-size-effect corrections, coincide. On these ensembles, the $\bar{\Pi}^{33}$ and $\bar{\Pi}^{88}$ finite-size effects are further enhanced by a factor of 1.5, due to the contribution from kaon loops. Away from the SU(3)-symmetric point, the long-distance behavior of the partially-quenched G_{con}^{88} and G_{con}^{08} correlators is expected to be dominated by the $I = 1$ contribution, with a prefactor of $1/3$ and $1/\sqrt{3}$ respectively. Therefore, we include a finite-size correction for $\bar{\Pi}_{\text{con}}^{88}$, which is equal to $1/3$ of that of $\bar{\Pi}^{33}$ and which cancels the opposite-sign correction on $\bar{\Pi}_{\text{dis}}^{88}$. The same procedure is applied to $\bar{\Pi}_{\text{con}}^{08}$ and $\bar{\Pi}_{\text{dis}}^{08}$.

3.8. Lattice results

We are now in a position to present our finite-volume corrected results on all our ensembles. Figure 5 shows the running of different contributions to $\bar{\Pi}(-Q^2)$, defined through the correlators in eq. (20), as a function of Q^2 on three different lattices at the same lattice spacing with increasingly lighter pions. While $\bar{\Pi}(-Q^2)$ is dimensionless, the TMR kernel $K(t, Q^2)$ in eq. (17) and Q^2 itself are dimensionful quantities, thus scale setting is needed to translate Q^2 -values in GeV² to lattice units. For this purpose, we insert into the kernel the dimensionless product $t_0 Q^2$,⁵ where the gradient flow scale t_0 introduced in section 3.4 has been computed on each ensemble, see appendix A and table 8. Results on each ensemble at $Q^2 = 1$ GeV² are given in table 4. For $\bar{\Pi}^{08}$, both connected and disconnected, only the results with the conserved-local discretization are available, for the reasons discussed in section 3.3. At the SU(3)-symmetric point $\bar{\Pi}_{\text{con}}^{88} = \bar{\Pi}^{33}$, and $\bar{\Pi}_{\text{dis}}^{88}$ as well as both components of $\bar{\Pi}^{08}$ vanish exactly. The corresponding entries in the table are set to zero. As one moves away from the SU(3)-symmetric point, the $\bar{\Pi}^{33}$ contribution increases, while the $\bar{\Pi}_{\text{conn}}^{88}$ contribution becomes smaller. The quenched charm contribution turns out to be relatively independent of the pion mass and increases linearly in the range of Q^2 values. The (negative) quark-disconnected contributions are also shown, on a scale

⁵With the exception of the charm contribution and its extrapolation for which $t_0^{\text{sym}} Q^2$ is used, see section 4.1.2.

$\times 10^5$	$\bar{\Pi}^{33}$	$\bar{\Pi}_{\text{con}}^{88}$	$\bar{\Pi}_{\text{dis}}^{88}$	$\bar{\Pi}^{88}$	$\bar{\Pi}_{\text{con}}^{08}$	$\bar{\Pi}_{\text{dis}}^{08}$	$\bar{\Pi}^{08}$
H101	2 855(6)	2 855(6)	0	2 855(6)	0	0	0
	2 769(7)	2 769(7)	0	2 769(7)			
H102	2 985(10)	2 749(7)	-12(2)	2 737(6)	209(5)	-39(7)	170(8)
	2 899(10)	2 663(7)	-12(2)	2 651(7)			
H105	3 156(21)	2 667(11)	-13(8)	2 654(13)	429(12)	-50(20)	379(21)
	3 069(21)	2 581(11)	-15(8)	2 566(13)			
N101	3 170(10)	2 683(5)	-31(4)	2 652(6)	430(6)	-70(15)	360(18)
	3 086(10)	2 597(5)	-33(4)	2 564(6)			
C101	3 349(13)	2 682(7)	-60(7)	2 622(9)	588(8)	-134(23)	454(24)
	3 264(14)	2 597(7)	-63(7)	2 534(10)			
B450	2 764(9)	2 764(9)	0	2 764(9)	0	0	0
	2 696(9)	2 696(9)	0	2 696(9)			
S400	2 903(13)	2 659(8)	-14(2)	2 645(8)	216(6)	-36(9)	180(10)
	2 836(14)	2 593(9)	-15(2)	2 578(8)			
N451	3 096(7)	2 628(3)	-22(3)	2 606(4)	412(4)	-50(11)	363(11)
	3 030(7)	2 562(3)	-23(3)	2 539(4)			
D450	3 279(10)	2 605(4)	-37(6)	2 568(6)	591(6)	-76(19)	516(18)
	3 214(10)	2 539(4)	-41(6)	2 498(6)			
H200	2 697(21)	2 697(21)	0	2 697(21)	0	0	0
	2 651(21)	2 651(21)	0	2 651(21)			
N202	2 736(12)	2 736(12)	0	2 736(12)	0	0	0
	2 689(13)	2 689(13)	0	2 689(13)			
N203	2 878(9)	2 620(7)	-10(2)	2 610(7)	225(5)	-26(9)	199(11)
	2 830(10)	2 573(7)	-10(2)	2 563(7)			
N200	3 023(11)	2 549(5)	-22(5)	2 527(6)	414(7)	-56(19)	359(20)
	2 977(11)	2 502(5)	-24(5)	2 478(6)			
D200	3 248(12)	2 535(5)	-53(8)	2 481(9)	621(8)	-131(22)	490(23)
	3 200(12)	2 487(5)	-56(8)	2 432(9)			
E250	3 530(21)	2 586(7)	-132(14)	2 454(14)	826(14)	-257(31)	569(31)
	3 482(21)	2 540(7)	-136(14)	2 404(14)			
N300	2 596(13)	2 596(13)	0	2 596(13)	0	0	0
	2 569(13)	2 569(13)	0	2 569(13)			
N302	2 737(16)	2 470(8)	-12(5)	2 458(8)	234(8)	-9(17)	225(16)
	2 710(16)	2 442(8)	-12(5)	2 430(8)			
J303	3 028(18)	2 455(8)	-35(5)	2 420(10)	498(10)	-96(14)	402(18)
	3 002(18)	2 429(8)	-37(5)	2 392(10)			
E300	3 268(27)	2 462(9)	-66(16)	2 396(16)	702(16)	-171(48)	530(52)
	3 242(27)	2 434(9)	-67(16)	2 368(16)			

Table 4: Estimate of connected and disconnected contribution to $\bar{\Pi}(-Q^2) \times 10^5$ at $Q^2 = 1 \text{ GeV}^2$ for the conserved-local (first line) and, when available, local-local (second line) discretization. Contributions tabulated as 0 vanish exactly due to SU(3)-symmetry. The contributions are estimated applying the bounding method as explained in section 3.6 and the correction for finite-size effects as of section 3.7.

enlarged by a factor 10. It is worth noting that $\bar{\Pi}_{\text{disc}}^{88}(-Q^2)$ is constant for $Q^2 \gtrsim 0.5 \text{ GeV}^2$, as predicted by perturbation theory.

4. Results at the physical point

Thanks to the availability of ensembles with four different lattice spacings and several quark masses, we can reliably extrapolate our results in section 3.8 to vanishing lattice spacing and physical values of the pseudoscalar meson masses. We define the target “physical” point in the isospin limit fixing $m_\pi = m_{\pi^0}$ and $m_K^2 - m_\pi^2/2 = (m_{K^+}^2 + m_{K^0}^2)/2 - m_{\pi^+}^2/2$ [103–105], which results in $m_\pi = 134.9768(5) \text{ MeV}$ and $m_K = 495.011(10) \text{ MeV}$ [7]. The pion mass of one of our ensembles is slightly below the physical value, which allows us to interpolate the results.

For $\bar{\Pi}^{33}(-Q^2)$, $\bar{\Pi}^{88}(-Q^2)$ and $\bar{\Pi}^{08}(-Q^2)$, we perform a combined extrapolation, including both discretizations of the vector current for $\bar{\Pi}^{33}(-Q^2)$ and $\bar{\Pi}^{88}(-Q^2)$. In the combined fit, we employ an ansatz that implies the same continuum limit for both discretizations, and that encodes the constraints $\bar{\Pi}^{33}(-Q^2) = \bar{\Pi}^{88}(-Q^2)$ and $\bar{\Pi}^{08}(-Q^2) = 0$ at the SU(3)-symmetric point. The charm contribution $\bar{\Pi}^{cc}(-Q^2)$ is treated independently as described in section 4.1.2.

4.1. Extrapolation strategy

At any fixed value of Q^2 we extrapolate each HVP function in the lattice spacing and the pseudoscalar meson masses to the physical point. We parametrize the lattice spacing dependence in terms of the gradient flow time at the SU(3)-symmetric point, t_0^{sym}/a^2 , as determined in ref. [66] and listed in table 1. As discussed in section 3.3, the on-shell quantities considered in this work are $\mathcal{O}(a)$ -improved, and hence we expect leading discretization effects $\mathcal{O}(a^2)$, up to logarithmic corrections [106, 107]. While our favored ansatz includes only an $\mathcal{O}(a^2)$ term, we also investigate the influence of higher powers in the lattice spacing, as well as a term proportional to $a^2 \log a$. More details are given in section 4.1.1.

The dependence of the HVP function contributions on the meson masses m_π and m_K is modelled using the proxy quantities $\phi_2 = 8t_0 m_\pi^2$ and $\phi_4 = 8t_0(m_K^2 + m_\pi^2/2)$. At the isospin-symmetric reference point defined above, the target values of our extrapolation are $\phi_2^{\text{phys}} = 0.0806(17)$ and $\phi_4^{\text{phys}} = 1.124(24)$, where the conversion to physical units is performed using $(8t_0^{\text{phys}})^{1/2} = 0.415(4)(2) \text{ fm}$ from ref. [66].⁶

For the CLS ensembles considered in this work ϕ_4 is approximately constant, with values between -3.5% and $+5.5\%$ of the target value ϕ_4^{phys} . Therefore, we only employ a linear term in ϕ_4 to model small deviations from the line of constant physics $m_K^2 + m_\pi^2/2 = \text{const}$. The interpolation of the pion-mass dependence across a larger range to the target value ϕ_2^{phys} is more complex and quantity-dependent. While it is possible to describe the HVP function in χ PT including vector mesons as resonances in the effective theory [109, 110], this applies only for $Q^2 \lesssim m_\pi^2$ and is thus of limited relevance in our case. Therefore, we choose to model the dependence by a polynomial in ϕ_2 . However, understanding the behavior of the various contribution towards the SU(2) chiral limit and the SU(3)-symmetric point helps constrain the model choice.

The isovector ($I = 1$) contribution $\bar{\Pi}^{33}$ dominates the HVP function, especially on ensembles that are close to the physical masses. Indeed, $\bar{\Pi}^{33}(-Q^2)$ diverges logarithmically in m_π in

⁶We note that the authors of ref. [66] obtain $(8t_0^{\text{phys}})^{1/2}$ from an extrapolation to a slightly different reference point, defined by $\bar{m}_\pi = 134.8(3) \text{ MeV}$ and $\bar{m}_K = 494.2(3) \text{ MeV}$ [108], which corresponds to $\bar{\phi}_2 = 0.0804(18)$ and $\bar{\phi}_4 = 1.120(24)$. Using the data in table II of ref. [66], we have translated the published value of $(8t_0^{\text{phys}})^{1/2}$ to the reference point used in this paper, which results in an increase by 0.2% in ϕ_2^{phys} and ϕ_4^{phys} . At our level of precision, the effect on the final results can safely be neglected.

the limit $m_\pi \rightarrow 0$ [111]. Therefore, we model the $I = 1$ contribution for the conserved-local discretization with an additional non-polynomial divergent term proportional to $\log \phi_2$,

$$\begin{aligned} \bar{\Pi}^{33,\text{CL}}(a^2/t_0^{\text{sym}}, \phi_2, \phi_4) = & \bar{\Pi}^{\text{sym}} + \delta_2^{\text{CL}} a^2/t_0^{\text{sym}} \\ & + \gamma_1^{33}(\phi_2 - \phi_2^{\text{sym}}) + \gamma_{\log}^{33} \log \phi_2/\phi_2^{\text{sym}} + \eta_1(\phi_4 - \phi_4^{\text{sym}}), \end{aligned} \quad (36)$$

and similarly for the local-local discretization, with δ_2^{CL} replaced by δ_2^{LL} . We also considered other possibilities for the divergent $m_\pi \rightarrow 0$ limit, such as including a $1/\phi_2 \sim 1/m_\pi^2$ term in addition to or instead of the $\log \phi_2$ one [112]. However, we observed that on our range of pion masses including only the $\log \phi_2$ term results in the best fit to the data.

The isoscalar ($I = 0$) contribution, $\bar{\Pi}^{88}$, has a finite limit for $m_\pi \rightarrow 0$ [111]. Therefore, we do not include any divergent term and use instead a polynomial quadratic in ϕ_2 , since we observe that a simple linear scaling does not describe the data. This results in

$$\begin{aligned} \bar{\Pi}^{88,\text{CL}}(a^2/t_0^{\text{sym}}, \phi_2, \phi_4) = & \bar{\Pi}^{\text{sym}} + \delta_2^{\text{CL}} a^2/t_0^{\text{sym}} \\ & + \gamma_1^{88}(\phi_2 - \phi_2^{\text{sym}}) + \gamma_2^{88}(\phi_2 - \phi_2^{\text{sym}})^2 + \eta_1(\phi_4 - \phi_4^{\text{sym}}), \end{aligned} \quad (37)$$

for the conserved-local discretization, and analogously for the local-local case.

When eqs. (36) and (37) are considered in isolation, $\bar{\Pi}^{\text{sym}}$, ϕ_2^{sym} and ϕ_4^{sym} define an arbitrary subtraction point, for which only one of the three parameters can be fixed by each fit. As the label ‘‘sym’’ suggests, we identify this point with the SU(3)-symmetric point in the continuum limit, which implies the constraint $2\phi_4^{\text{sym}} = 3\phi_2^{\text{sym}}$. Moreover, $\bar{\Pi}^{33,\text{sym}} \equiv \bar{\Pi}^{88,\text{sym}}$, such that all three parameters $\bar{\Pi}^{\text{sym}}$, ϕ_2^{sym} and ϕ_4^{sym} can be fully determined in a combined fit.

Finally, the $\bar{\Pi}^{08,\text{CL}}$ contribution includes one SU(3)-singlet current that vanishes linearly in $m_s - m_\ell$ towards the SU(3)-symmetric point. To leading order this is proportional to $m_K^2 - m_\pi^2$ or equivalently $\phi_4 - 3/2\phi_2$, thus we model $\bar{\Pi}^{08,\text{CL}}$ using a simple linear dependence

$$\bar{\Pi}^{08,\text{CL}}(a^2/t_0^{\text{sym}}, \phi_2, \phi_4) = \lambda_1(\phi_4 - 3/2\phi_2). \quad (38)$$

In this case, we fit the only available discretization (conserved-local) without including a term describing the dependence on the lattice spacing as no discretization effects are observed within statistical errors. Moreover, we do not observe any significant deviation from the linear behavior.

The relative errors on the pion and kaon masses, as well as the scale t_0 that enter ϕ_2 and ϕ_4 , are of the same order as the uncertainties of the $\bar{\Pi}$ contributions. Thus, we fit the quantities ϕ_2 , ϕ_4 , $\bar{\Pi}_{\text{CL}}^{33}$, $\bar{\Pi}_{\text{LL}}^{33}$, $\bar{\Pi}_{\text{CL}}^{88}$, $\bar{\Pi}_{\text{LL}}^{88}$ and $\bar{\Pi}_{\text{CL}}^{08}$ simultaneously, except for ensembles at the SU(3)-symmetric point where only the independent quantities $\phi_2 = (2/3)\phi_4$, $\bar{\Pi}_{\text{CL}}^{33} = \bar{\Pi}_{\text{CL}}^{88}$ and $\bar{\Pi}_{\text{LL}}^{33} = \bar{\Pi}_{\text{LL}}^{88}$ are fitted. We include the correlations between quantities on the same ensemble, which limits the size of the covariance matrix C_l on ensemble l to either 7×7 or 3×3 in the SU(3)-symmetric case. Still, we find relatively poor fit quality unless we use a shrunk estimator of the covariance matrix by scaling the off-diagonal elements of C_l according to [113, 114]

$$\tilde{C}_l(\lambda) = (1 - \lambda)C_l + \lambda \text{diag}(C_l). \quad (39)$$

We found that the χ^2/dof of the fit as a function of the shrinkage parameter λ is approximately constant in an interval of small λ values, before increasing for $\lambda \rightarrow 0$. Therefore, we select $\lambda = 0.05$ as a small value in the constant region. The errors on the optimal fit parameters and the extrapolation results are obtained applying the bootstrap procedure to the fit, and are thus unaffected by this modification to the covariance matrix.

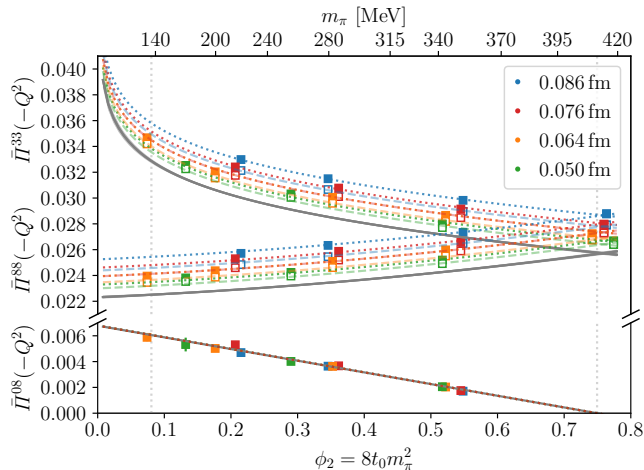


Figure 6: Plot of $\bar{\Pi}^{33}(-Q^2)$, $\bar{\Pi}^{88}(-Q^2)$ (left) and $\bar{\Pi}^{08}(-Q^2)$ (right) at $Q^2 = 1 \text{ GeV}^2$ on different ensembles as a function of the pion mass, together with the results of the combined fit. With respect to the values in table 4, the data points in the plot include a small shift to the same value of ϕ_4 . Filled symbols and dotted lines denote the conserved-local discretization, while open symbols and dashed lines denote the local-local one.

4.1.1. Study of the fit model systematics

The choice of the fit ansatz introduces a systematic error that we estimate by considering several variations of the fit model.

The choice of a fit ansatz that constrains both discretizations to have the same continuum limit is motivated by theory. However, we also check this by performing independent fits including only one of the two discretizations, and observing that the continuum-extrapolated results agree well within errors between different discretizations and with the combined fit ones. This further supports our choice for the fit ansatz used for the final fit and all the variations in the following.

Our main extrapolation model includes only the leading $\mathcal{O}(a^2)$ discretization effects using two parameters δ_2^{CL} and δ_2^{LL} , one for each discretization of the correlator, common to all flavor contributions in eqs. (36) and (37). We observe that this model fits the data well in the energy range below Q^2 between 2–3 GeV^2 . We also tested a fit model with independent discretization effects parameters for each flavor contribution, which resulted in parameters compatible within errors. Fits to $\bar{\Pi}^{08}$ were performed without including terms describing discretization effects (see eq. (38)), since no dependence on the lattice spacing could be detected within statistical errors. Similarly, the fit parameters describing the mass dependence for both CL and LL discretizations were chosen to be the same. This is consistent with the choice of not including mass-dependent cut-off effects, and it is supported by the fact that a fit with independent parameters resulted in compatible results.

For Q^2 values larger than 2–3 GeV^2 , we observe a rapid deterioration of the quality of the fit. We interpret this as evidence that discretization effects at larger values of Q^2 are not dominated by a^2 effects, but that higher powers in the lattice spacing are also relevant. Indeed, a modification of eqs. (36), (37) and (38) to include both terms proportional to a^2 and to a^3 fits the data well on an extended range up to $Q^2 \approx 7 \text{ GeV}^2$, as was already observed in ref. [90]. Specifically, we find that an ansatz including δ_2^{CL} and δ_2^{LL} , as well as two additional parameters δ_3^{CL} and δ_3^{LL}

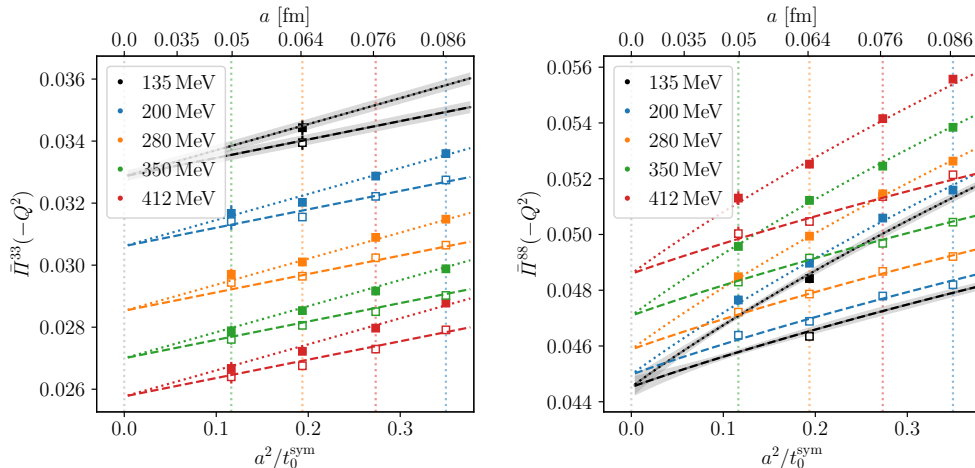


Figure 7: Plots of $\bar{\Pi}^{33}(-Q^2)$ at $Q^2 = 1 \text{ GeV}^2$ (left) and $\bar{\Pi}^{88}(-Q^2)$ at $Q^2 = 5 \text{ GeV}^2$ (right) on different ensembles as a function of the lattice spacing, together with the results of the combined fit. The left panel shows an example in which the $\mathcal{O}(a^2)$ fit model is used, while a term proportional to a^3 has been included in the right plot as well. Different colors distinguish different pion masses from a set of five reference values. Using the functional form determined by the fit, each data point has been shifted to the closest value of ϕ_2 matching one of the reference pion masses, and to the same value of ϕ_4 . Filled symbols and dotted lines denote the conserved-local discretization, while open symbols and dashed lines denote the local-local one.

yields the best fit quality for $\bar{\Pi}^{33}$, $\bar{\Pi}^{88}$ and $\bar{\Pi}^{08}$. However, including a^3 discretization effects may lead to overfitting the data at lower values of Q^2 , where a term proportional to a^2 is found to successfully describe discretization effects.

Therefore, for our final results we switch from the results obtained via a purely $\mathcal{O}(a^2)$ ansatz at low Q^2 to those obtained via an ansatz with both $\mathcal{O}(a^2)$ and $\mathcal{O}(a^3)$ lattice artifacts by applying a smoothed step function centered around 2.5 GeV^2 ,

$$\Theta(Q^2) = \frac{1}{2} + \frac{1}{2} \tanh\left(\frac{Q^2 - 2.5 \text{ GeV}^2}{1.0 \text{ GeV}^2}\right). \quad (40)$$

Both fits agree well within one standard deviation below $\approx 3 \text{ GeV}^2$, and start to disagree above that, in accordance with the poor quality of the $\mathcal{O}(a^2)$ fit in the high-energy region. As a consequence, the values of $\bar{\Pi}$ extrapolated to the physical point at $Q^2 > 2.5 \text{ GeV}^2$ are statistically less precise than values extrapolated at $Q^2 < 2.5 \text{ GeV}^2$, as it is clearly visible in figure 11.

To test for possible violations of the leading $\mathcal{O}(a^2)$ scaling due to the missing $\mathcal{O}(a)$ -improvement parameters f_V and $\tilde{c}_V^{C,L}$ we also considered a fit ansatz with both a and a^2 terms. We observe that this does not describe the data any better than the $\mathcal{O}(a^2)$ fit, so we conclude that residual $\mathcal{O}(a)$ discretization effects are not significant at our level of precision.

Following ref. [107], we also considered a logarithmically-enhanced term of the form $\tilde{c}_{\bar{\Pi}}(Q^2) \cdot (a^2/t_0^{\text{sym}}) \log(t_0^{\text{sym}}/a^2)/2$, with the Q^2 -dependent coefficient fixed to the free-theory prediction

$$\tilde{c}_{\bar{\Pi}}^{\text{CL}}(Q^2) = \frac{7}{480\pi^2} t_0^{\text{sym}} Q^2, \quad \tilde{c}_{\bar{\Pi}}^{\text{LL}}(Q^2) = \frac{1}{48\pi^2} t_0^{\text{sym}} Q^2, \quad (41)$$

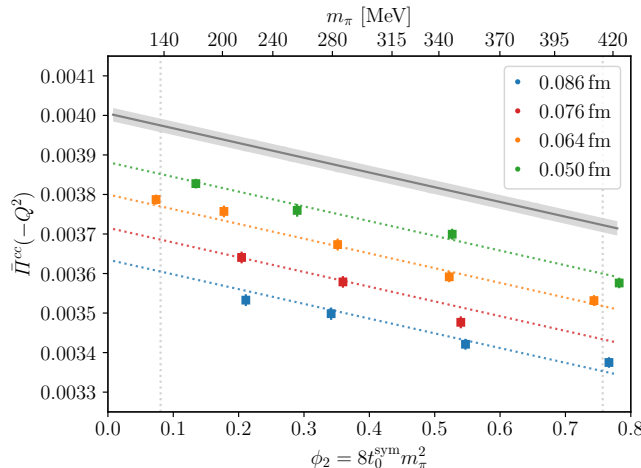


Figure 8: Same as figure 6 for the charm contribution $\bar{\Pi}^{cc}(-Q^2)$ at $Q^2 = 1 \text{ GeV}^2$.

for both $\bar{\Pi}^{33}$ and $\bar{\Pi}^{88}$. Including this term in eqs. (36), (37) and (38), we do not observe any significant change in the fit quality over the entire range of Q^2 values. The HVP functions extrapolated to the physical point are shifted downwards by less than 0.4%, which is always smaller than the statistical error.

We also tested a variation of the fit model ansatz applying a cut on the range of pion masses, leaving out those ensembles with $m_\pi > 400 \text{ MeV}$. For both the low Q^2 and high Q^2 fits we observe a mild deviation with respect to the fit without the mass cut, always smaller than the statistical error. As was done in ref. [8], we take this as an estimate of the systematic error due to the chiral and continuum extrapolation and add it to our error budget.

4.1.2. Extrapolation of the charm contribution

Compared to the isovector and isoscalar channels, the (quenched) charm contribution $\bar{\Pi}_{\text{con}}^{cc}$ is smaller and much more precise. We do not include it in the combined fit and extrapolate it separately instead, neglecting the small correlation between $\bar{\Pi}^{cc}$ and the other channels. For the fit to the conserved-local discretization we use a linear model in ϕ_2 , i.e.

$$\bar{\Pi}_{\text{con}}^{cc}(a^2/t_0^{\text{sym}}, \phi_2) = \bar{\Pi}_{\text{con}}^{cc, \text{sym}} + \delta_2^{cc, \text{CL}} a^2/t_0^{\text{sym}} + \gamma_1^{cc}(\phi_2 - \phi_2^{\text{sym}}). \quad (42)$$

The local-local discretization shows a less favorable extrapolation, as there is a $\approx 40\%$ difference between the coarsest lattice spacings and the continuum limit, while the conserved-local only shows a $\approx 10\%$ difference. As in our previous work [8], we exclude the local-local discretization from the subsequent analysis and the final results. As in eqs. (36), (37) and (38), we employ t_0^{sym} from [66] as a proxy for the size of the discretization effects for each $\bar{\Pi}_{\text{con}}^{cc}$ data point. However, we also use t_0^{sym} instead of the t_0 value computed on each ensemble to set the Q^2 scale input in the TMR kernel, and to determine the ϕ_2 of each ensemble entering eq. (42). While using t_0^{sym} introduces correlations between ensembles at the same lattice spacing, we found that it significantly reduces the curvature of the data with respect to ϕ_2 and allows us to use the linear fit model in eq. (42) [115]. We take into account the additional correlations increasing the size of our covariance matrix in a straightforward manner. For all other aspects, the method used to extrapolate the isovector and isoscalar contributions is directly carried over to the charm

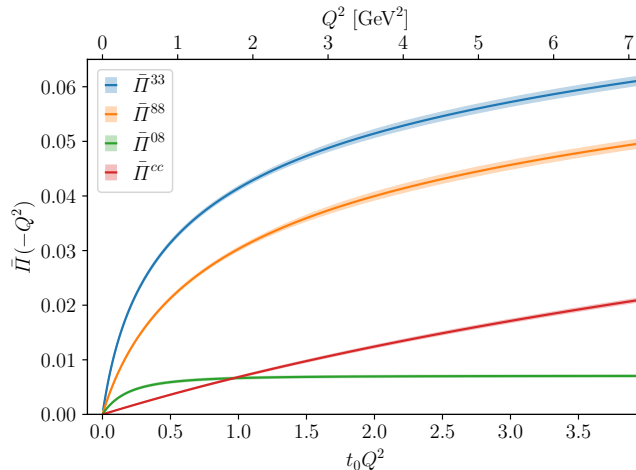


Figure 9: Contributions to the running extrapolated at the physical point as a function of the momentum transfer squared Q^2 . The contributions are normalized without including the charge factors, according to eqs. (20).

contribution. For this component we perform a cut at $m_\pi < 400$ MeV and < 300 MeV to estimate any systematics of the fit. The three extrapolations give compatible results.

4.2. The running with energy

The results of the extrapolation of the HVP functions $\bar{\Pi}^{33}$, $\bar{\Pi}^{88}$, $\bar{\Pi}^{08}$ and $\bar{\Pi}^{cc}$ to the physical point are plotted as a function of Q^2 in figure 9. Furthermore, the corresponding numerical estimates are listed in table 5 for several values of Q^2 . These numbers constitute the main result of this paper. The quoted errors include all statistical and systematic uncertainties on the result extrapolated to the continuum limit, provided that exact isospin symmetry is assumed. According to the flavor decomposition described in section 3.2, one can use these results to construct the hadronic running of α and $\sin^2 \theta_W$. The corresponding results for $\Delta\alpha_{\text{had}}(-Q^2)$ and $\Delta_{\text{had}} \sin^2 \theta_W(-Q^2)$ are plotted in figure 10 and listed in table 6, including the uncertainty due to isospin-breaking effects.

The results in tables 5 and 6 for an extended set of 109 values of Q^2 between 0.01 GeV^2 and 7 GeV^2 are given in appendix F.

In the following two subsections we discuss the estimation of the systematic errors due to scale setting, the quenching of the charm quark and neglecting isospin breaking.

4.2.1. Scale-setting error

To set the relative scale between the ensembles employed in this work, we use t_0 [70] which can be computed to very high precision with a small computing investment, see appendix A and table 8. In order to convert t_0 into physical units, we use $(8t_0^{\text{phys}})^{1/2} = 0.415(4)(2) \text{ fm}$, which has been determined in ref. [66] on a subset of ensemble used in this work, using a combination of the pion and kaon decay constants f_π and f_K . Therefore, we have a 1.1% error on our absolute scale.

Since the (subtracted) HVP function is a dimensionless quantity, scale setting enters only indirectly, through the value of Q^2 in physical units that appears in the TMR kernel, and in the

Q^2 [GeV ²]	$t_0 Q^2$	$\bar{\Pi}^{33}$	$\bar{\Pi}^{88}$
0.1	0.055 3	0.007 64 (9) (8) (4)(0)[13]	0.004 06 (4)(0) (4)(0) [6]
0.4	0.221 2	0.020 61(15)(11)(10)(1)[21]	0.012 59 (8)(1)(11)(1)[14]
1.0	0.553	0.032 87(17)(10)(21)(3)[29]	0.022 51 (9)(3)(19)(3)[21]
2.0	1.106	0.042 9 (2) (1) (3)(1) [4]	0.031 69(17)(5)(27)(5)[33]
3.0	1.659	0.048 8 (5) (0) (4)(1) [6]	0.037 4 (5)(1) (3)(1) [6]
4.0	2.212	0.052 9 (6) (0) (4)(1) [7]	0.041 4 (6)(1) (4)(1) [7]
5.0	2.764	0.056 0 (6) (0) (5)(1) [8]	0.044 5 (6)(1) (4)(1) [8]
6.0	3.317	0.058 6 (6) (0) (5)(2) [8]	0.047 1 (6)(1) (4)(2) [8]
7.0	3.87	0.060 8 (6) (0) (5)(2) [8]	0.049 3 (6)(1) (4)(2) [8]
Q^2 [GeV ²]	$t_0 Q^2$	$\bar{\Pi}^{08}$	$\bar{\Pi}^{cc}$
0.1	0.055 3	0.001 75(4)(0) (7)(0) [8]	0.000 421(2)(1) (9)(-) [9]
0.4	0.221 2	0.004 40(7)(0)(14)(0)[15]	0.001 652(7)(2)(33)(-)[34]
1.0	0.553	0.006 06(8)(0)(15)(0)[17]	0.003 97 (2)(1) (8)(-) [8]
2.0	1.106	0.006 72(8)(0)(15)(0)[17]	0.007 49 (3)(1)(14)(-)[14]
3.0	1.659	0.006 90(8)(0)(15)(0)[17]	0.010 64 (4)(1)(19)(-)[19]
4.0	2.212	0.006 98(8)(0)(15)(1)[17]	0.013 48 (5)(2)(23)(-)[24]
5.0	2.764	0.007 01(8)(0)(15)(1)[17]	0.016 08 (6)(2)(26)(-)[27]
6.0	3.317	0.007 03(8)(0)(15)(1)[17]	0.018 46 (6)(2)(29)(-)[29]
7.0	3.87	0.007 04(8)(0)(15)(1)[17]	0.020 66 (7)(2)(31)(-)[32]

Table 5: Contributions to the running extrapolated to the physical point. The first quoted uncertainty is the statistical error, the second is the systematic error from varying the fit model estimated in section 4.1.1, the third is the scale-setting error (see section 4.2.1), and the fourth is the systematic from missing charm sea-quark loops (see section 4.2.2). The final uncertainty, quoted in square brackets, is the combination of the previous ones.

Q^2 [GeV ²]	$t_0 Q^2$	$\Delta\alpha_{\text{had}}$	$\Delta_{\text{had}} \sin^2 \theta_W$
0.1	0.055 3	0.000 842 (9) (7) (4)(0) (2)[13]	-0.000 849(10) (8) (5)(0)(1)[14]
0.4	0.221 2	0.002 342(15)(10)(12)(1) (7)[23]	-0.002 368(17)(11)(18)(2)(3)[27]
1.0	0.553	0.003 864(17) (8)(22)(4)(12)[32]	-0.003 93 (2) (1) (3)(0)(1) [4]
2.0	1.106	0.005 21 (2) (0) (3)(1) (2) [4]	-0.005 30 (3) (0) (4)(1)(1) [5]
3.0	1.659	0.006 05 (6) (0) (4)(1) (2) [7]	-0.006 14 (6) (0) (5)(1)(1) [8]
4.0	2.212	0.006 66 (7) (0) (4)(1) (2) [9]	-0.006 76 (8) (0) (6)(1)(1)[10]
5.0	2.764	0.007 16 (8) (0) (5)(2) (2) [9]	-0.007 24 (8) (0) (6)(2)(1)[10]
6.0	3.317	0.007 57 (8) (0) (5)(2) (2) [9]	-0.007 64 (8) (0) (6)(2)(1)[11]
7.0	3.87	0.007 93 (8) (0) (4)(2) (2) [9]	-0.007 99 (8) (0) (6)(2)(1)[11]

Table 6: Total HVP contribution to the running of α and $\sin^2 \theta_W$. After the statistical error and the fit, scale-setting and charm-sea-quark systematic errors propagated from the $\bar{\Pi}$ results in table 5, the fifth uncertainty is the systematic error from missing isospin-breaking effects (see section 4.2.3). The final uncertainty quoted is the combination of the previous ones.

extrapolation to the physical point through the definition of the point in the (m_π, m_K) plane that corresponds to an isosymmetric version of the physical world.

In analogy to the case of $a_\mu^{\text{HVP,LO}}$ considered in section B.2 of ref. [63], the error Δl_0 on the scale $l_0 = (8t_0)^{1/2}$ propagates to $\bar{\Pi}$ according to

$$\frac{\Delta \bar{\Pi}}{\bar{\Pi}} \simeq \left| \frac{l_0}{\bar{\Pi}} \frac{d\bar{\Pi}}{dl_0} \right| \frac{\Delta l_0}{l_0} = \left| \frac{2t_0 Q^2}{\bar{\Pi}} \frac{\partial \bar{\Pi}}{\partial(t_0 Q^2)} + \frac{2\phi_2}{\bar{\Pi}} \frac{\partial \bar{\Pi}}{\partial \phi_2} + \frac{2\phi_4}{\bar{\Pi}} \frac{\partial \bar{\Pi}}{\partial \phi_4} \right| \frac{\Delta l_0}{l_0}. \quad (43)$$

The first term in the absolute value on the r.h.s. is proportional to the slope of $\bar{\Pi}$ as a function of Q^2 . For all contributions, it is positive and monotonically decreasing with Q^2 , relatively more important at low Q^2 , where $\bar{\Pi}$ varies faster, than at high Q^2 . For $\bar{\Pi}^{\gamma\gamma}$, it evaluates to ≈ 0.9 at $Q^2 = 1 \text{ GeV}^2$, decreasing to ≈ 0.6 at $Q^2 = 7 \text{ GeV}^2$ and increasing to ≈ 1.7 at $Q^2 = 0.1 \text{ GeV}^2$. Empirically, we observe that the third term in the r.h.s. of eq. (43) is of the same order and negative, which has the effect of partially cancelling the Q^2 contribution and reducing the scale setting error. Specifically for the $\bar{\Pi}^{33}$ contribution, also the second term in the r.h.s. of eq. (43) is non-negligible and negative as the $I = 1$ contribution at small m_π increases faster with decreasing ϕ_2 .

To reliably estimate the scale setting error including cases in which the three terms nearly cancel, we employ bootstrap sampling, which allows us to go beyond the first-order error propagation in eq. (43). Artificial bootstrap samples with a normal distribution are generated for $(8t_0^{\text{phys}})^{1/2}$ and, in turn, ϕ_2^{phys} and ϕ_4^{phys} , which define the physical point in the fit model, and $t_0 Q^2$. The induced distribution of $\bar{\Pi}(Q^2)$ is obtained evaluating the optimized fit model at $(\phi_2^{\text{phys}}, \phi_4^{\text{phys}})$ samples from these distributions, and using numerical derivatives in the case of the $t_0 Q^2$ distribution to account for the small deviation of the samples with respect to set of values at which the extrapolation is performed. The resulting scale setting error is the third error contribution given for each quantity in tables 5 and 6. The scale-setting error as a function of energy for both $\bar{\Pi}^{\gamma\gamma}$ and $\bar{\Pi}^{Z\gamma}$ is compared to other sources of uncertainty in figure 11. In both cases, the systematic error from scale setting is larger than the statistical for $0.5 \text{ GeV}^2 \lesssim Q \lesssim 2.5 \text{ GeV}^2$, while the statistical error dominates at $Q \gtrsim 2.5 \text{ GeV}^2$.

4.2.2. Charm quark loop effects

Our computation is performed using gauge ensembles with $N_f = 2 + 1$ flavors of dynamical quarks, such that the light and strange quarks are present in the “sea”, while for the charm quark only the connected Wick contraction of the valence contribution is included in the result. We include the missing contributions from charm sea quarks, as well as disconnected diagrams involving charm valence quarks as a systematic uncertainty in our error budget.

As explained in detail in appendix E we quantify the charm quenching effect phenomenologically, by estimating the contributions from D -meson loops to the connected vector correlator involving (u, d, s) quarks. In particular, we determine the contributions of $D^+ D^-$, $D^0 \bar{D}^0$ and $D_s^+ D_s^-$ loops to the R -ratio and, in turn, the subtracted HVP function, by treating the D -meson form factors in scalar QED. Other non-perturbative effects, such as changes in the ω and ϕ masses in QCD with $N_f = 2 + 1$, due to mixing with the J/ψ and higher charmonium vector resonances are found to be negligible. For $Q^2 = 5 \text{ GeV}^2$ we estimate that the size of the charm sea contribution is only about 3 permil of the corresponding (u, d, s) quark contribution.

Regarding the charm disconnected valence quark contribution, we note that the BMW collaboration has reported it to be less than one percent of the light and strange disconnected contributions to $a_\mu^{\text{HVP,LO}}$ [21]. We assume that the effect is of similar size for the hadronic running of the electromagnetic and weak couplings. Since the light and strange disconnected correlators already contribute at most one percent to the total hadronic running, the contribution

from disconnected charm loops is expected to be 0.01%. This is subleading with respect to the quenched charm systematic error already included in table 6.

4.2.3. Isospin-breaking effects

As discussed in section 3.4, our simulations are performed in the limit of strong isospin symmetry, i.e. we work with degenerate up and down quark masses ($m_u = m_d = m_\ell$) and neglect effects caused by quantum electrodynamics (QED). To estimate the systematic effect due to this assumption, we have evaluated the HVP functions in QCD+QED on a subset of our isospin-symmetric ensembles based on the techniques described in [116–121]. We use the QED_L prescription [122] to regularize the IR divergence of non-compact lattice QED. Furthermore, we choose the same boundary conditions for the photon field as for the QCD gauge field. In a next step, QCD+QED obtained from reweighted isosymmetric QCD is expanded up to leading order around isosymmetric QCD in terms of the electromagnetic coupling e^2 as well as the shifts in the bare quark masses Δm_u , Δm_d and Δm_s , as applied by the RM123 collaboration [120, 121]. This procedure results in Feynman diagrams which represent perturbative quark mass shifts and the interaction between quarks and photons [123–126].

To match both theories we utilize a scheme based on leading-order χ PT, including leading order strong and electromagnetic isospin breaking corrections [105, 123]. On each ensemble, we match the results for $m_{\pi^0}^2$ and $m_{K^+}^2 + m_{K^0}^2 - m_{\pi^+}^2$ in both theories, which serve as proxies for the average light and strange quark masses, respectively. These conditions are compatible with the definition of the “physical” point of isosymmetric QCD in section 4. We extend this scheme by the corresponding proxy for the light quark mass splitting $m_{K^+}^2 - m_{K^0}^2 - m_{\pi^+}^2 + m_{\pi^0}^2$ [123] and set it to its physical value. As we consider leading-order effects, the electromagnetic coupling does not renormalize and, hence, is fixed via the fine-structure constant $e^2 = 4\pi\alpha$ [121]. Isospin-breaking effects in the determination of the scale are neglected.

We have computed the leading-order QCD+QED quark-connected contribution to $\bar{\Pi}^{\gamma\gamma}$ and $\bar{\Pi}^{Z\gamma}$ for the three ensembles D450, N200 and H102 as well as the pseudo-scalar meson masses required for the above hadronic renormalization scheme. The considered Feynman diagrams are evaluated by means of stochastic $U(1)$ quark sources with support on a single time slice and Z_2 photon sources that are used to stochastically estimate the all-to-all photon propagator in Coulomb gauge. To reduce the stochastic noise, covariant approximation averaging [127] in combination with the truncated solver method [128] is applied. The noise problem of the vector-vector correlation function at large time separations is treated via a reconstruction using a single exponential function. A more detailed description of the computation is given in refs. [123, 124, 129]. Since the renormalization procedure of the local vector current in our QCD+QED computation is based on a comparison of the local-local and the conserved-local discretisations of the vector-vector correlation function and hence differs from the purely isosymmetric QCD calculation [65] we determine the relative correction by isospin breaking in the QCD+QED setup. We observe that the size of the relative first-order corrections for $\bar{\Pi}^{\gamma\gamma}$ [123] and $\bar{\Pi}^{Z\gamma}$ is largest on D450. To rate the systematic error of disregarding isospin-breaking corrections, which is added to the error budget of the final result, we multiply the obtained relative correction on D450 by the final results obtained from the isosymmetric QCD calculation. In figure 11, we compare this error for both $\bar{\Pi}^{\gamma\gamma}$ and $\bar{\Pi}^{Z\gamma}$ to other sources of uncertainty as a function of energy. We find that isospin-breaking effects make a larger contribution to the running of α compared to $\sin^2\theta_W$. However, this systematic uncertainty makes only a small contribution to the total error. It is comparable to the statistical error of $\Delta\alpha_{\text{had}}$ for $Q^2 \lesssim 2.5 \text{ GeV}^2$ but the scale setting uncertainty presently dominates in this regime.

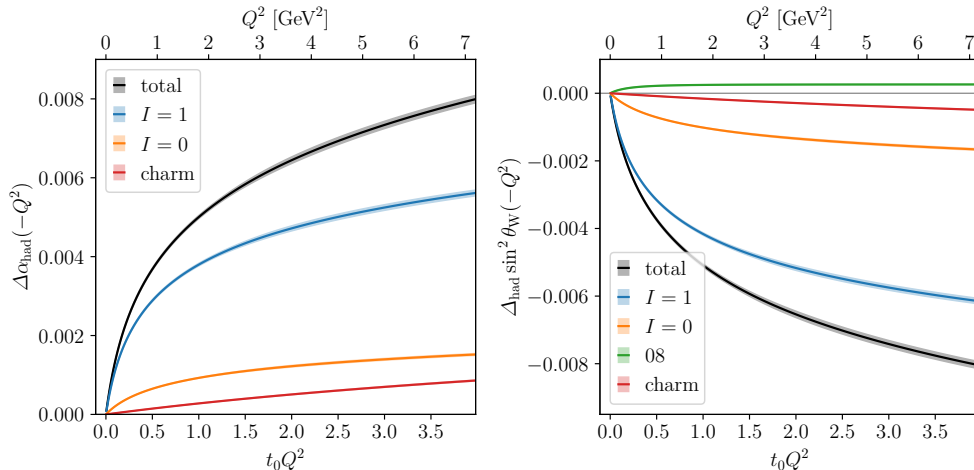


Figure 10: Total HVP contribution to the running of α (left panel) and $\sin^2 \theta_W$ (right panel) as a function of Q^2 , together with the $I = 1$, $I = 0$, charm and, for $\sin^2 \theta_W$, $Z\gamma$ -mixing contributions.

4.2.4. Rational approximation of the running

In addition to sampling the HVP function at the Q^2 values in table 6, we provide an analytic function of Q^2 that can be used to interpolate the HVP function to any value of Q^2 in the range up to 7 GeV^2 . For this purpose, we use a rational function

$$\bar{\Pi}(-Q^2) \approx R_M^N(Q^2) = \frac{\sum_{j=0}^M a_j Q^{2j}}{1 + \sum_{k=1}^N b_k Q^{2k}}, \quad (44)$$

where the numerator and the denominator are polynomials of degree M and N respectively, with $b_0 = 1$ in the denominator. This choice is motivated by the fact that the HVP function $\Pi(-Q^2)$ can be expressed as a Stieltjes series with a finite radius of convergence through a once-subtracted dispersion relation [130]. This guarantees the existence of a convergent series of multi-point Padé approximants with rigorous error bounds [131, 132], which is particularly useful when the sampling of the HVP function is constrained to the lattice discrete momenta, see ref. [130]. The TMR method used in this work gives us more flexibility in the choice of the momenta to sample, and allows for a very straightforward way to obtain the rational approximation, by solving the over-constrained system [133]

$$\sum_i \frac{1}{\delta \bar{\Pi}(-Q_i^2)} \left[\sum_{j=0}^M a_j Q_i^{2j} - \left(1 + \sum_{k=1}^N b_k Q_i^{2k} \right) \bar{\Pi}(-Q_i^2) \right] = 0, \quad (45)$$

via a least-squared fit, weighted by the inverse of the total error $\delta \bar{\Pi}$ at each Q_i and in the range of energies $0 < Q^2 \leq 7 \text{ GeV}^2$. The minimization uses the constraint that $R_M^N(Q^2)$ has poles at $Q_i^2 < 0$. Since the subtracted HVP function $\bar{\Pi}$ vanishes by definition at $Q^2 = 0$, we set $a_0 = 0$.

We observe that a rational function of degree $M = 3$ and $N = 3$ describes the data very well. Using the set of 109 values of Q^2 between 0.01 GeV^2 and 7 GeV^2 that we sampled, we find that higher-order coefficients are small and poorly determined by eq. (45). The resulting rational

approximation for $\bar{\Pi}^{\gamma\gamma}$ is

$$\bar{\Pi}^{\gamma\gamma}(-Q^2) \approx \frac{0.1094(23)x + 0.093(15)x^2 + 0.0039(6)x^3}{1 + 2.85(22)x + 1.03(19)x^2 + 0.0166(12)x^3}, \quad x = \frac{Q^2}{\text{GeV}^2}, \quad (46)$$

where the errors assigned to the coefficients in the numerator and denominator, together with the correlation matrix

$$\text{corr}^{\gamma\gamma} \begin{pmatrix} a_1 \\ a_2 \\ a_3 \\ b_1 \\ b_2 \\ b_3 \end{pmatrix} = \begin{pmatrix} 1 & & & & & \\ 0.455 & 1 & & & & \\ 0.17 & 0.823 & 1 & & & \\ 0.641 & 0.946 & 0.642 & 1 & & \\ 0.351 & 0.977 & 0.915 & 0.869 & 1 & \\ 0.0489 & -0.0934 & 0.0667 & -0.044 & -0.115 & 1 \end{pmatrix} \quad (47)$$

reproduce the error band very accurately.⁷ For $\bar{\Pi}^{Z\gamma}$, the rational approximation is

$$\bar{\Pi}^{Z\gamma}(-Q^2) \approx \frac{0.0263(6)x + 0.025(5)x^2 + 0.00089(34)x^3}{1 + 2.94(29)x + 1.12(27)x^2 + 0.015(8)x^3}, \quad x = \frac{Q^2}{\text{GeV}^2}, \quad (48)$$

with the correlation matrix

$$\text{corr}^{Z\gamma} \begin{pmatrix} a_1 \\ a_2 \\ a_3 \\ b_1 \\ b_2 \\ b_3 \end{pmatrix} = \begin{pmatrix} 1 & & & & & \\ 0.48 & 1 & & & & \\ 0.278 & 0.734 & 1 & & & \\ 0.619 & 0.964 & 0.644 & 1 & & \\ 0.402 & 0.983 & 0.815 & 0.91 & 1 & \\ 0.236 & 0.416 & 0.882 & 0.389 & 0.486 & 1 \end{pmatrix}. \quad (49)$$

The deviation of the approximation from our measured values is compared to the different sources of uncertainty in figure 11. We find that the deviation is always much smaller than the combined error: For instance, for $Q^2 > 1.5 \text{ GeV}^2$ it is less than 1/5 of the combined error, and less than 0.3% of that of the actual data.

4.2.5. Dependence on the definition of the physical point

As discussed in section 4, the results quoted in tables 5 and 6 have been obtained by extrapolation to a reference point in the isospin-symmetric limit. The shift in $\bar{\Pi}^{\gamma\gamma}(Q^2)$ and $\bar{\Pi}^{Z\gamma}(Q^2)$ corresponding to a small change in the choice of convention for the physical point can be estimated from the derivatives of the extrapolated values with respect to ϕ_2 and ϕ_4 . An effective description of the derivatives as a function of Q^2 is given by the rational approximations

$$\frac{\partial \bar{\Pi}^{\gamma\gamma}(-Q^2)}{\partial \phi_2} = -\frac{0.2676x + 0.3960x^2}{1 + 6.944x + 12.06x^2}, \quad \frac{\partial \bar{\Pi}^{\gamma\gamma}(-Q^2)}{\partial \phi_4} = -\frac{0.06393x}{1 + 1.569x}, \quad (50)$$

$$\frac{\partial \bar{\Pi}^{Z\gamma}(-Q^2)}{\partial \phi_2} = -\frac{0.06388x + 0.08935x^2}{1 + 6.880x + 11.83x^2}, \quad \frac{\partial \bar{\Pi}^{Z\gamma}(-Q^2)}{\partial \phi_4} = -\frac{0.01887x}{1 + 1.663x}, \quad (51)$$

where $x = Q^2/\text{GeV}^2$.

Combined with the derivatives with respect to the momentum transfer variable $t_0 Q^2$, which can be easily obtained from eqs. (46) and (48), the given rational approximations can also be used to account for a small variation of the global scale according to eq. (43).

⁷For both eqs. (46) and (48), we observe that a rational approximation with the same coefficients and errors except for $b_3 = 0$ approximates the data equally well. We choose to include the b_3 since this makes the extrapolation to higher Q^2 better behaved. However, we stress that the rational approximations in eqs. (46) and (48) are valid only in the range of $Q^2 \leq 7 \text{ GeV}^2$ and are not suitable for an extrapolation outside this range.

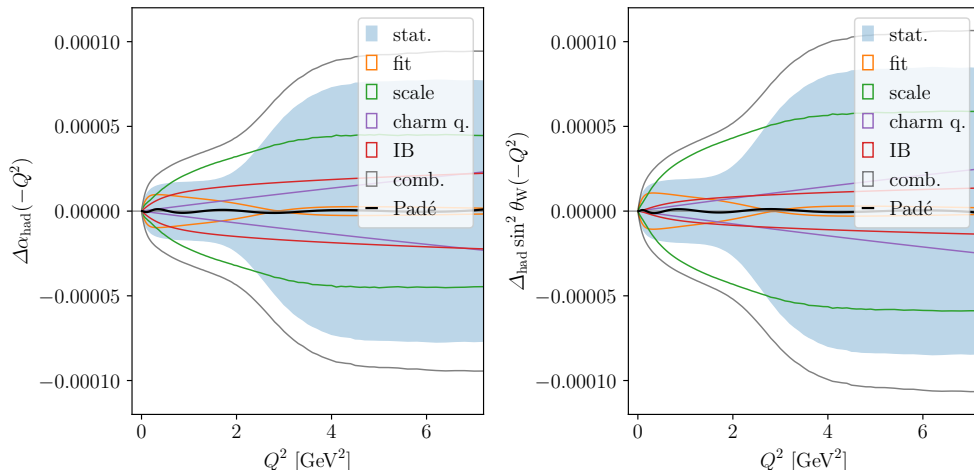


Figure 11: The deviation of the rational approximation of $\Delta\alpha_{\text{had}}(-Q^2)$ (left) and $\Delta_{\text{had}} \sin^2 \theta_W(-Q^2)$ (right) from the data, plotted as a function of Q^2 and compared to the statistical error (blue-shaded area) as well as different sources of systematic uncertainty: fit model (orange-bordered area), scale setting (green-bordered area) and isospin breaking (red-bordered area). The plots show that statistical errors increase when a term of $\mathcal{O}(a^3)$ is added to the leading discretization effect of $\mathcal{O}(a^2)$ in the fit model for $Q \gtrsim 2.5 \text{ GeV}^2$. The gray lines represent the total error.

5. Comparison and discussion

The main results of this paper are the contributions from u , d , s and c quarks to the hadronic running of the QED coupling α and the electroweak mixing angle $\sin^2 \theta_W$, as a function of the space-like momentum $Q^2 > 0$, computed in lattice QCD. In this section, we present a detailed comparison of our results to those from other lattice calculations, and to phenomenological analyses based on dispersion theory and hadronic cross section data.

5.1. Hadronic running of the electromagnetic coupling

Our estimates for $\Delta\alpha_{\text{had}}(-Q^2)$ can be directly compared to the lattice calculation results by BMWc, given in table S3 in the supplementary material of ref. [21], after correcting the latter for finite-size effects determined in that same reference. Ratios between results obtained by BMWc and our estimates are plotted in the upper left panel in figure 12, for the total contribution as well as for its various components. While there is good agreement for the isoscalar ($I = 0$) component, a slight tension at the level of 1–2 standard deviations is observed in the isovector ($I = 1$) channel that dominates the total contribution. We note that estimates by BMWc are smaller by 2–3% for $Q^2 \lesssim 3 \text{ GeV}^2$. For the charm contribution, our results are up to 2% larger than BMWc’s, but they are compatible within the errors, which are dominated by scale setting. The comparison of the absolute values of the two lattice results is depicted in the right panel of figure 12, which shows the slightly smaller error of the BMWc result. The most recent result from BMWc [6], also shown in the right panel of figure 12, has a smaller error but it is only available at $Q^2 = 1 \text{ GeV}^2$. We also mention that the first lattice calculation of the quark-connected HVP contributions to running of α and $\sin^2 \theta_W$ up to $Q^2 = 10 \text{ GeV}^2$ was published by Burger *et al.* [19], who reported

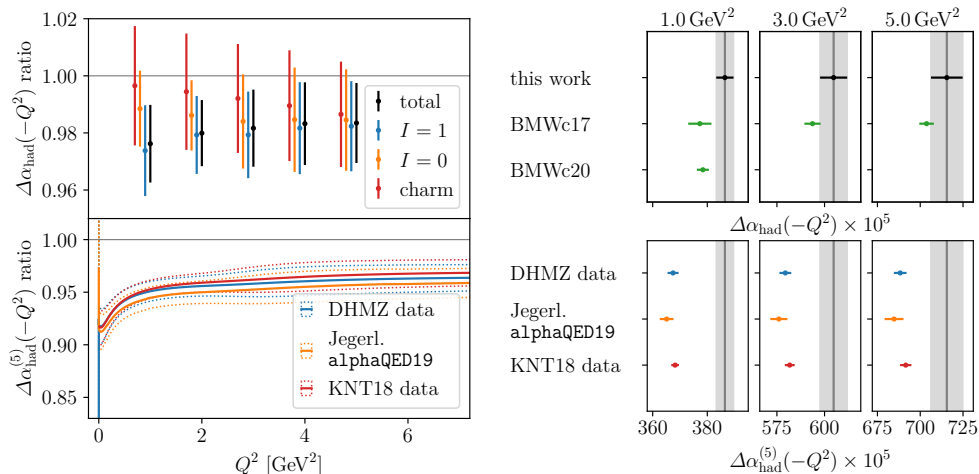


Figure 12: Left, upper panel: ratio of the hadronic running $\Delta\alpha_{\text{had}}$ computed by BMWc [21] divided by our results, for five different momenta. In addition to the total contribution, we show the isovector ($I = 1$), isoscalar ($I = 0$) and charm quark components. Left, lower panel: the total hadronic running $\Delta\alpha_{\text{had}}^{(5)}$ from various phenomenological estimates [12, 31, 134] and the lattice result of ref. [21], normalized by the result of this work. Right: Compilation of results for the four-flavor $\Delta\alpha_{\text{had}}$ lattice computations [6, 21] (above) and the five-flavor $\Delta\alpha_{\text{had}}^{(5)}$ phenomenological estimates (below) at selected values of Q^2 . The gray vertical error band for the result of this work includes the small bottom quark contribution as an additional systematic error, see section 5.1 for details.

a 2–3% error dominated by systematic effects. However, we do not include this result in our comparison since the disconnected contribution has not been determined in that reference.

In the lower left panel of figure 12 we show the ratios of three recent phenomenological determinations of $\Delta\alpha_{\text{had}}^{(5)}(-Q^2)$ and the rational approximation of our result as continuous curves. Our result lattice results for $\Delta\alpha_{\text{had}}(-Q^2)$ includes the contributions from u , d , s and c quarks. In order to account for the contributions from bottom quarks that are needed to complete the estimate for $\Delta\alpha_{\text{had}}^{(5)}(-Q^2)$, we use results by the HPQCD collaboration for the lowest four time moments of the HVP [135]. We determine the contribution from bottom quarks by constructing Padé approximants from the moments, which results in a few-permil effect on the total hadronic running of the coupling (up to 2.6 permil at the largest $Q^2 = 7 \text{ GeV}^2$). This effect is larger than the 0.4 permil effect reported for the HVP contribution to the muon $g - 2$ [136] due to the fact that the running coupling scale Q^2 is not well separated from the bottom quark mass, in contrast to the muon mass case.⁸ However, this effect is a small fraction of the percent-level total error on $\Delta\alpha_{\text{had}}(-Q^2)$ and we include it as an additional source of systematic error.

Results from Davier *et al.* [12, 137] (labelled “DHMZ data”), Keshavarzi *et al.* [31, 138] (KNT18 data), and based on Jegerlehner’s `alphaQEDc19` software package [13, 134] show good agreement among each other, but are between 3 and 6% lower than our estimate.⁹ After taking the errors

⁸As a crosscheck, we have reproduced the bottom quark contribution to the muon $g - 2$ reported by HPQCD [136].

⁹The estimate of $\Delta\alpha_{\text{had}}^{(5)}(-Q^2)$ in the space-like region corresponding to ref. [12] was kindly provided to us by Davier, Hoecker, Malaescu, and Zhang. We are grateful to Keshavarzi, Nomura and Teubner for providing the

Q_0^2	pQCD'[Adler]	KNT18[data]
0.1	–	0.026 798(110)
0.4	–	0.025 372(107)
0.5	–	0.025 045(106)
1.0	0.023 928(223)	0.023 889(103)
2.0	0.022 492(149)	0.022 578(97)
3.0	0.021 640(129)	0.021 754(93)
4.0	0.021 020(116)	0.021 144(89)
5.0	0.020 528(107)	0.020 656(86)
6.0	0.020 117(99)	0.020 247(83)
7.0	0.019 763(93)	0.019 894(80)

Table 7: The contribution from $[\Delta\alpha_{\text{had}}^{(5)}(-M_Z^2) - \Delta\alpha_{\text{had}}^{(5)}(-Q_0^2)]$ for various threshold energy Q_0^2 . The second column is based on the pQCD'[Adler] approach in eq. (53). The third column is obtained with KNT18[data] approach in eq. (54). See the text for details.

into account, we observe a sizeable tension of up to 3.5 standard deviation between our lattice calculation and phenomenological estimates for space-like momenta in the range between 3 and 7 GeV². For smaller space-like momenta, the tension is even larger, due to the fact that the extrapolation to the continuum limit has been performed with an a^2 -term only, which results in a smaller error.

The electromagnetic coupling at the Z pole, $\Delta\alpha_{\text{had}}^{(5)}(M_Z^2)$, puts a limit on the sensitivity of global electroweak precision fits [13, 56, 139]. This quantity also receives growing interest with respect to searches for physics beyond the Standard Model (BSM) at a future International Linear Collider. Our lattice results for $\Delta\alpha_{\text{had}}(-Q^2)$ for space-like Q^2 up to 7 GeV² can be combined with either perturbative QCD or phenomenology to obtain the five-flavor hadronic running at the Z pole, $\Delta\alpha_{\text{had}}^{(5)}(M_Z^2)$ with no or much reduced reliance on experimental data.

The connection between $\Delta\alpha_{\text{had}}(-Q^2)$ and the hadronic running of α for five quark flavors at the Z pole in the time-like region can be established via the so-called Euclidean split technique (also known as Adler function approach) [9, 10]. As the name suggests, this technique allows for separating the contribution to the running at space-like kinematics, which is accessible to computational frameworks formulated in Euclidean spacetime such as lattice QCD, from the small subleading contribution associated with the space-like to time-like rotation at high energies. The method amounts to rewriting the hadronic contribution to the running at M_Z as

$$\Delta\alpha_{\text{had}}^{(5)}(M_Z^2) = \Delta\alpha_{\text{had}}^{(5)}(-Q_0^2) + \left[\Delta\alpha_{\text{had}}^{(5)}(-M_Z^2) - \Delta\alpha_{\text{had}}^{(5)}(-Q_0^2) \right] + \left[\Delta\alpha_{\text{had}}^{(5)}(M_Z^2) - \Delta\alpha_{\text{had}}^{(5)}(-M_Z^2) \right]_{\text{pQCD}}, \quad (52)$$

where the threshold energy Q_0^2 is typically around 5 GeV². The first term on the r.h.s. is proportional to the space-like HVP according to eq. (3). In the literature [9, 10], $\Delta\alpha_{\text{had}}^{(5)}(-Q_0^2)$ has been evaluated by employing the dispersive approach. Here, we evaluate this quantity using our lattice QCD results $\Delta\alpha_{\text{had}}(-Q_0^2)$ shown in table 6 as input, with the addition of the small bottom quark contribution as a systematic error.

The second term in eq. (52) is the high-energy contribution $[\Delta\alpha_{\text{had}}^{(5)}(-M_Z^2) - \Delta\alpha_{\text{had}}^{(5)}(-Q_0^2)]$. To estimate it, we follow Jegerlehner's idea [17] of utilizing the Adler function $D(Q^2)$ defined in eq. (4).

full covariance matrix of the R -ratio, allowing for a determination of $\Delta\alpha_{\text{had}}^{(5)}(-Q^2)$ consistent with ref. [31].

For sufficiently large Q^2 , the Adler function is calculable within perturbative QCD (pQCD) plus minor non-perturbative (NP) corrections [9, 140]. Our implementation of this approach, which we call pQCD'[Adler], is based on the public code `pQCDAdler` by Jegerlehner [141]. It takes into account full three-loop QCD with charm and bottom quark mass effects as well as massless four- and five-loop effects to improve high-energy tails. The code also accounts for the NP corrections via the operator product expansion and Padé approximants. We note that the pQCD'[Adler] approach does not rely on the R -ratio integral, and does not suffer from the systematics of the cross-section data.

Once the Adler function $D(Q^2)$ has been determined, we can calculate

$$\left[\Delta\alpha_{\text{had}}^{(5)}(-M_Z^2) - \Delta\alpha_{\text{had}}^{(5)}(-Q_0^2) \right]_{\text{pQCD}'} = \frac{\alpha}{3\pi} \int_{Q_0^2}^{M_Z^2} \frac{dQ^2}{Q^2} D(Q^2), \quad (53)$$

where α is the QED coupling in the Thomson limit, and pQCD' indicates that perturbative QCD has been augmented by small NP corrections when estimating $D(Q^2)$. Our results for $[\Delta\alpha_{\text{had}}^{(5)}(-M_Z^2) - \Delta\alpha_{\text{had}}^{(5)}(-Q_0^2)]$ obtained in this way are shown in the second column in table 7. The quoted errors, which amount to about 0.5% at $Q_0^2 = 5 \text{ GeV}^2$, originate from uncertainties in the strong coupling at the Z pole and heavy-quark pole masses, which are used as input quantities. For smaller Q_0^2 , the uncertainty associated with NP corrections to $D(Q_0^2)$ grows significantly, hence we cannot access very small values of Q_0^2 due to the Landau pole appearing in the strong coupling.

In addition to using pQCD'[Adler] for the evaluation of $[\Delta\alpha_{\text{had}}^{(5)}(-M_Z^2) - \Delta\alpha_{\text{had}}^{(5)}(-Q_0^2)]$, we also consider the dispersive integral

$$\left[\Delta\alpha_{\text{had}}^{(5)}(-M_Z^2) - \Delta\alpha_{\text{had}}^{(5)}(-Q_0^2) \right] = \frac{\alpha}{3\pi} (M_Z^2 - Q_0^2) \int_{m_{\pi^0}^2}^{\infty} ds \frac{R(s)}{(s + Q_0^2)(s + M_Z^2)}. \quad (54)$$

This allows for a consistency check of the pQCD'[Adler] approach described above. The appearance of Q_0^2 in the denominator of the integrand implies that contributions from the R -ratio at low energies are suppressed along with any experimental uncertainties in their determination. To compute the dispersion integral in eq. (54), we use the R -ratio data from KNT18 [31]. Since ref. [31] does not quote a result for $[\Delta\alpha_{\text{had}}^{(5)}(-M_Z^2) - \Delta\alpha_{\text{had}}^{(5)}(-Q_0^2)]$, we have performed the integration of the R -ratio ourselves, using the full covariance matrix [138] in the error estimate. In the following, we shall refer to this method as “KNT18[data]”. The corresponding results are shown in the third column of table 7. The results are consistent with the pQCD' approach (second column) within the uncertainty.

Finally, we focus on the second combination in square brackets in eq. (52), which provides the link between the space-like and time-like regions at M_Z . We quote the pQCD estimate by Jegerlehner [13, 55],

$$\left[\Delta\alpha_{\text{had}}^{(5)}(M_Z^2) - \Delta\alpha_{\text{had}}^{(5)}(-M_Z^2) \right]_{\text{pQCD}} = 0.000\,045(2). \quad (55)$$

With these ingredients in hand, we can provide an estimate for the phenomenologically relevant quantity $\Delta\alpha_{\text{had}}^{(5)}(M_Z^2)$, using our lattice estimate for $\Delta\alpha_{\text{had}}^{(5)}(-Q_0^2)$ as input in eq. (52). In figure 13, we show $\Delta\alpha_{\text{had}}^{(5)}(M_Z^2)$ as a function of the Euclidean squared momentum transfer Q_0^2 . In the left panel the contribution from $[\Delta\alpha_{\text{had}}^{(5)}(-M_Z^2) - \Delta\alpha_{\text{had}}^{(5)}(-Q_0^2)]$ has been determined in perturbative QCD via the Adler function (pQCD'[Adler]), while in the right panel the same quantity has been evaluated using the R -ratio data and correlation matrix from KNT18 in eq. (54). The blue bands represent the total error obtained by adding in quadrature all uncertainties that

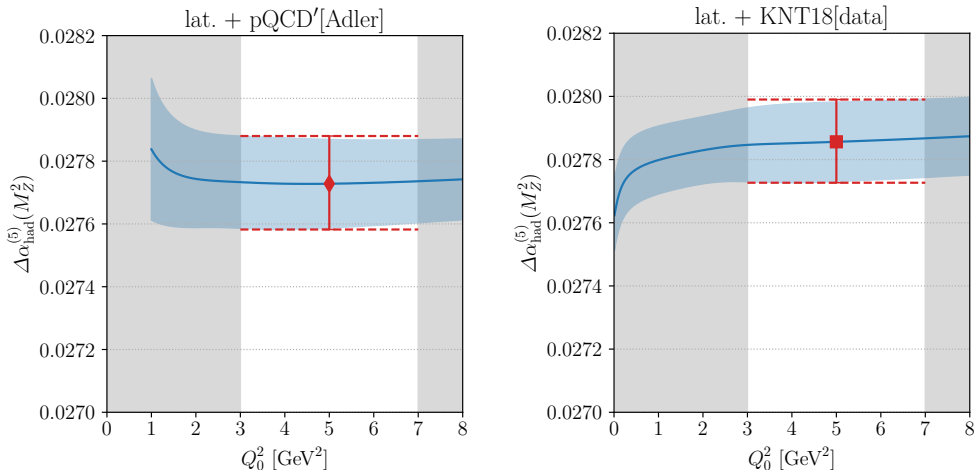


Figure 13: The hadronic contribution to the running coupling for five flavors at the Z pole mass, $\Delta\alpha_{\text{had}}^{(5)}(M_Z^2)$, evaluated according to eq. (52) and using our lattice result for $\Delta\alpha_{\text{had}}^{(5)}(-Q_0^2)$, plotted as a function of the threshold energy Q_0^2 . Left: The higher energy contribution $[\Delta\alpha_{\text{had}}^{(5)}(-M_Z^2) - \Delta\alpha_{\text{had}}^{(5)}(-Q_0^2)]$ computed via the pQCD' approach in eq. (53) using the pQCDAdler software package [141]. Right: Results based on the KNT18[data] approach of eq. (54) using the R -ratio data with full covariance matrix [31, 138]. The red symbols in each panel are taken to produce the final estimates for each method, while the maxima and minima of the blue bands within the non-shaded region are used to estimate the uncertainty.

enter eq. (52). In both cases we find that the estimates for $\Delta\alpha_{\text{had}}^{(5)}(M_Z^2)$ are very stable for $Q_0^2 \gtrsim 3 \text{ GeV}^2$. The slight upward trend and the loss of precision observed for $Q_0^2 \lesssim 2 \text{ GeV}^2$ when using the pQCD'[Adler] approach is symptomatic of the failure of pQCD at strong couplings. Alternatively, when employing the dispersive approach of eq. (54), one observes a decreasing trend for $Q_0^2 \lesssim 2 \text{ GeV}^2$, which is due to the enhanced contributions from low-lying resonances (ρ , ω , ϕ) in eq. (54) as Q_0^2 is lowered. For our final results in both approaches we choose $Q_0^2 = 5 \text{ GeV}^2$ and estimate the uncertainty associated with the choice of Q_0^2 from the maxima and minima of the blue bands in the region $3\text{--}7 \text{ GeV}^2$. In this momentum range, our lattice results for the hadronic running can be extrapolated reliably to the continuum limit. Furthermore, this choice of interval guarantees that our final estimate is not affected by the Landau pole when using the pQCD'[Adler] approach, nor is it dominated by the experimentally determined R -ratio when employing eq. (54) instead.

For our main result of the hadronic running of the QED coupling at the Z pole we adopt the pQCD'[Adler] approach and quote

$$\begin{aligned} \Delta\alpha_{\text{had}}^{(5)}(M_Z^2)|_{\text{Lat+pQCD}'[\text{Adler}]} &= 0.02773(9)_{\text{lat}}(2)_{\text{bottom}}(12)_{\text{pQCD}'[\text{Adler}]} \\ &= 0.02773 \pm 0.00015. \end{aligned} \quad (56)$$

The first error is the total uncertainty of our lattice estimate of $\Delta\alpha_{\text{had}}^{(5)}(-5 \text{ GeV}^2)$ as listed in table 7, while the second error accounts for the neglected contribution from bottom quark effects. The error labeled pQCD'[Adler] is associated with the evaluation of $[\Delta\alpha_{\text{had}}^{(5)}(-M_Z^2) - \Delta\alpha_{\text{had}}^{(5)}(-5 \text{ GeV}^2)]$ (see the second column in table 7), augmented by the maximum deviations from the central value

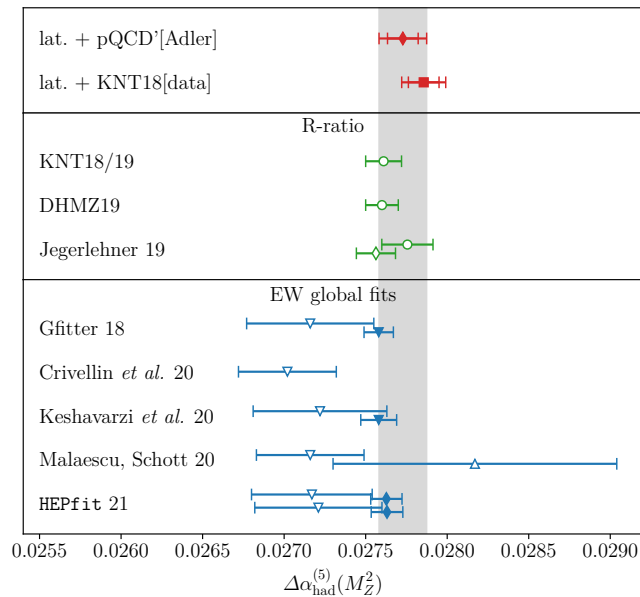


Figure 14: Compilation of results for $\Delta\alpha_{\text{had}}^{(5)}(M_Z^2)$. The first two data points (red symbols) represent the results from the Euclidean split technique using our lattice estimate for $\Delta\alpha_{\text{had}}^{(5)}(-Q_0^2)$. Green circles denote results based on the standard dispersive approach, where the R -ratio integration is performed over the entire momentum range. From top to bottom, we plot the results from refs. [11, 31], [12], and [13]. The estimate based on the Adler function in ref. [13] is shown as a green diamond. Blue symbols represent the results from global EW fits, published in refs. [34–36, 142, 143] (see the text for further details). The upper triangle point from ref. [36] does not use the Higgs mass. The gray band represents our final result quoted in eq. (56).

in the region $Q_0^2 \in [3, 7] \text{ GeV}^2$.

For completeness, we also list the result obtained via the KNT18[data] approach, which yields

$$\begin{aligned} \Delta\alpha_{\text{had}}^{(5)}(M_Z^2)|_{\text{Lat+KNT18[data]}} &= 0.02786(9)_{\text{lat}}(2)_{\text{bottom}}(10)_{\text{KNT18[data]}} \\ &= 0.02786 \pm 0.00013, \end{aligned} \quad (57)$$

where the meaning of the errors is similar to eq. (56). The relative difference to the result obtained via the Adler function amounts to less than 0.5% and is indicative of the different treatment of the non-lattice contribution in eq. (52).

In figure 14, we present a compilation of results for $\Delta\alpha_{\text{had}}^{(5)}(M_Z^2)$ obtained using our lattice estimate of the HVP, the standard dispersive approach, as well as global EW fits. The first two symbols (red filled diamond/square) show our results represented by eqs. (56) and (57).

We shall first focus on our main result — the red filled diamond (Lattice + pQCD[Adler]). The inner and outer error bars represent the total uncertainty and the combination of the first two errors in eq. (56), respectively. The total error of about 0.5% is close to the precision of the dispersive approach (open green circles/diamond). Our main result is consistent with the latter and also broadly agrees with the estimates from global EW fits (blue upper/lower triangles).

It is instructive to compare our main result — which is represented by the gray vertical band

— with Jegerlehner’s evaluation [13], also based on the Euclidean split method and represented by the open green diamond in the figure. The two estimates differ chiefly by the contribution at the hadronic energy scale $Q_0^2 = 5 \text{ GeV}^2$: while our result is based on lattice QCD, the open green diamond has been obtained from the R -ratio. In figure 12, we have observed a clear tension between the two evaluations (black vs. orange). However, from eq. (56) one easily reads off that $\Delta\alpha_{\text{had}}^{(5)}(-Q_0^2)$ contributes at most 60% to the total uncertainty of $\Delta\alpha_{\text{had}}^{(5)}(M_Z^2)$, resulting in smaller tension, due to the additional, albeit correlated, uncertainty from the high-energy contribution.

Next, we compare our results to the estimate from global EW fits. This category includes results from the Gfitter group [142], ref. [34] (obtained using the `HEPfit` code [144]), refs. [35, 36] (employing the Gfitter library), and ref. [143] (with two different scenarios). The blue open lower triangles in figure 14 were all obtained by a fit to EW precision data, treating $\Delta\alpha_{\text{had}}^{(5)}(M_Z^2)$ as a free parameter. This allows for $\Delta\alpha_{\text{had}}^{(5)}(M_Z^2)$ to be determined exclusively from the other EW precision observables, and favors smaller values compared to both lattice and R -ratio determinations. The precision of these estimates of $\Delta\alpha_{\text{had}}^{(5)}(M_Z^2)$ is lower compared to results extracted from the lattice and the R -ratio. With the exception of ref. [34], all results are compatible with our value within 1.3σ . Therefore, we conclude that lattice calculations of the HVP contribution to the hadronic running of α and the muon $g - 2$ are not in contradiction with global EW fits [34]. The data point from ref. [36] marked by the blue open upper triangle results from treating both the Higgs mass M_H and $\Delta\alpha_{\text{had}}^{(5)}(M_Z^2)$ as fit parameters without priors. It shows that if the precise experimental input for M_H is not used, the resulting determination of $\Delta\alpha_{\text{had}}^{(5)}(M_Z^2)$ favors a larger value with a significantly larger uncertainty [36]. Fits represented by blue filled triangles employ priors for $\Delta\alpha_{\text{had}}^{(5)}(M_Z^2)$ centered about the R -ratio estimate [35, 142]. It is interesting to note that the output for $\Delta\alpha_{\text{had}}^{(5)}(M_Z^2)$ is very close to the input R -ratio estimate. Finally, the authors of ref. [143] apply the Euclidean split technique in eq. (52), by combining the perturbative running with the lattice result by BMWc [21] at $Q_0^2 = 4 \text{ GeV}^2$. In this way they obtain $\Delta\alpha_{\text{had}}^{(5)}(M_Z^2) = 0.02766(10)$, which is consistent with our result in eq. (56). Using this value as prior for the fit, the posterior probability is shown in figure 14 with a blue filled diamond for two different scenarios. The observed pull of 1.1 – 1.3σ further supports the conclusion that lattice results are not inconsistent with global EW fits [143]. Alternatively, one could use our estimate $\Delta\alpha_{\text{had}}^{(5)}(M_Z^2)$ as a prior, which is left to future work.

5.2. Hadronic running of the electroweak mixing angle

The lattice formalism gives us full control over the quark flavor charge factors that are used to construct the quark-level vector currents in eqs. (6) and (12). The ability to perform an exact separation of the vacuum polarization function $\overline{\Pi}^{\gamma Z}$ in terms of individual valence quark flavors (see section 3) is an inherent feature of the lattice approach. It eliminates the need to perform a reweighting of exclusive channels in hadronic cross section data, which is a source of systematic uncertainty in phenomenological determinations of the hadronic running of $\sin^2 \theta_W$. In section 4.2 we have reported our results for the hadronic contribution to the running of the electroweak mixing angle, $\Delta_{\text{had}} \sin^2 \theta_W(-Q^2)$, as a function of the space-like momentum $Q^2 > 0$. Our result can thus replace estimates from the data-driven approach in studies that apply the running with energy to determine the electroweak mixing angle θ_W in the Thomson limit, with the understanding that current lattice QCD results are limited to $Q^2 \approx 7 \text{ GeV}^2$. In the following, we compare our data with previous results in the literature.

Phenomenological estimates of $\Delta_{\text{had}} \sin^2 \theta_W(-Q^2)$ can be obtained by applying Jegerlehner’s `alphaQEDc19` software package [134], see ref. [13]. Since `alphaQEDc19` provides $\Delta\alpha_{\text{had}}$ and $\Delta\alpha_{2,\text{had}}$ as primary quantities with their respective error estimates, we perform the comparison with our

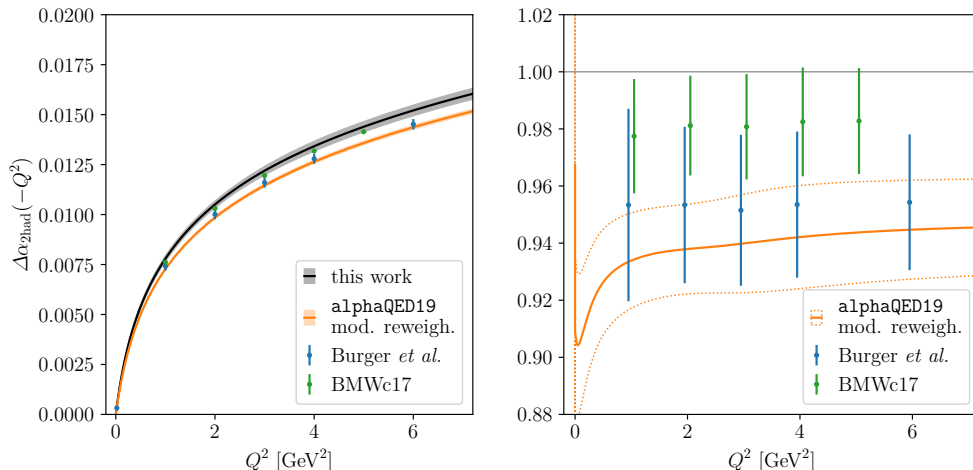


Figure 15: Left: Hadronic contributions to the running of the weak coupling α_2 from our computation, compared to lattice results from ref. [19], as well as the phenomenological estimate determined using `alphaQEDc19` [13, 134], as a function of the space-like momentum transfer Q^2 . Right: Ratios of the phenomenological estimate and of the lattice computation in ref. [19] over our result.

lattice determination for the running of the SU(2) gauge coupling α_2 . As explained in ref. [13], the software package implements a modified flavor separation scheme assuming SU(3) flavor symmetry [58], which differs from the “perturbative” separation scheme advocated in refs. [40, 42, 45]. This modification is motivated by the observation that it brings the phenomenological estimate into better agreement with previous lattice results, see for instance the comparison plot in figure 9 of ref. [19] and the discussion in ref. [13].

A comparison between the `alphaQEDc19` estimate of $\Delta_{\text{had}} \sin^2 \theta_W(-Q^2)$ and our lattice results is shown in figure 15. In performing this comparison, one has to take into account that the result of ref. [13] has been obtained using $\sin^2 \theta_{\text{eff}}^\ell = 0.23153$ [145] as a reference value in the normalization of eq. (11). This amounts to a 3% difference which is accounted for in the plot. We observe that, even though the modified reweighting brings the phenomenological estimate closer to our lattice results, it still falls short by about 8% at smaller Q^2 and 4% at higher values.

In figure 15 we include points from previous lattice calculations. While the BMWc paper [21] does not quote results for the running of α_2 , or for the $\bar{\Pi}^{08}$ component, we can still estimate the α_2 contribution using the fact that the Wick-connected component is $\bar{\Pi}^{08, \text{con}} = \sqrt{3}/2(\bar{\Pi}^{33} - \bar{\Pi}_{\text{con}}^{88})$, together with the observation from our data that the same component varies between 130% at $Q^2 = 1 \text{ GeV}^2$ and 125% at $Q^2 \geq 5 \text{ GeV}^2$ of $\bar{\Pi}^{08}$. For the data points for $\Delta\alpha_{2, \text{had}}$ plotted in figure 15, we correct for this by adding a $\mathcal{O}(0.5\%)$ positive contribution with negligible errors to the BMWc data points, which brings them into good agreement with our result, especially at larger Q^2 . The result by Burger *et al.* [19] is missing the quark-disconnected contribution, as in the $\Delta\alpha_{1, \text{had}}$ case. Thus, it is plausible that their estimate is lower than our result. Since the SU(3)-symmetric flavor-separation scheme implemented in `alphaQEDc19` was motivated by the findings of earlier lattice calculations [19, 61, 146], the missing quark-disconnected contributions in those references might explain the observed shortfall between the phenomenological estimate on the one hand, and the more comprehensive results of our work and ref. [21] on the other.

Another possible strategy to estimate the hadronic contribution to the running of θ_W at low

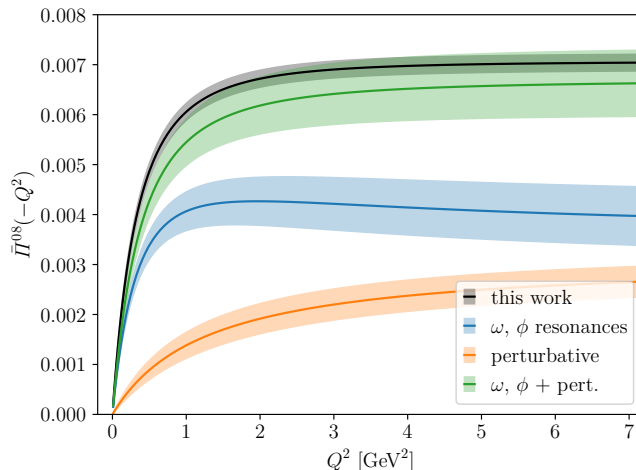


Figure 16: HVP mixing function $\bar{\Pi}^{08}$ as a function of Q^2 from our lattice computations, compared to the phenomenological model described in appendix D. Two contributions to the model are also shown in isolation: the finite perturbative QCD one, and the narrow resonances one resulting from the ω and ϕ mesons with opposite signs.

energies is to combine the phenomenological evaluation of $\Delta\alpha_{\text{had}}(-Q^2)$ from R -ratio experimental data with extra input providing the exact flavor separation and reweighting obtained from precise lattice data. From eq. (20) we observe that the difference between $\bar{\Pi}^{\gamma\gamma}$ and $\bar{\Pi}^{Z\gamma}$ is proportional to the $I = 0$ mixing HVP function $\bar{\Pi}^{08}$ given in table 5, plus a small charm quark contribution. In figure 16, we plot our results for $\bar{\Pi}^{08}$ as a function of Q^2 up to 7 GeV^2 . To our knowledge, this is the most precise ab-initio computation of this quantity and the first to include both connected and disconnected contributions. In the same plot we also show a phenomenological model estimate, which is discussed in detail in appendix D. The error band represents the statistical uncertainty on the model, which is dominated by the experimental error on the partial decay widths into e^+e^- of the ω and ϕ vector resonances. The model is obtained assuming that the quark-disconnected diagrams of type (s, s) and (ℓ, s) are negligible, and this assumption is shown to give a good estimate in an analogous model for the $a_\mu^{\text{HVP,LO}}$ strange and light isoscalar contributions. Even neglecting this sources of systematic uncertainty, the plot shows clearly that the lattice results are in good agreement with the model over the whole range of Q^2 values, but significantly more precise.

$\bar{\Pi}^{08}(Q^2)$ over the whole Q^2 range is well approximated within 15% of its total error by a rational approximation of order $[2/2]$ of the kind employed in section 4.2.4, i.e.

$$\bar{\Pi}^{08}(-Q^2) = \frac{0.0217(11)x + 0.0151(12)x^2}{1 + 2.93(8)x + 2.15(12)x^2}, \quad x = \frac{Q^2}{\text{GeV}^2}, \quad (58)$$

where the numerator a_i and denominator b_j parameters are strongly correlated according to

$$\text{corr} \begin{pmatrix} a_1 \\ a_2 \\ b_1 \\ b_2 \end{pmatrix} = \begin{pmatrix} 1 & & & \\ 0.97 & 1 & & \\ 0.97 & 0.984 & 1 & \\ 0.944 & 0.994 & 0.98 & 1 \end{pmatrix}. \quad (59)$$

At large Q^2 , $\bar{\Pi}^{08}$ varies very slowly with Q^2 . For $Q^2 \rightarrow \infty$, the rational approximation tends to

the finite value $a_2/b_2 = 0.00704(17)$ which coincides with the value at our largest $Q^2 = 7 \text{ GeV}^2$

$$\bar{I}^{08} = 0.00704(17) \quad (60)$$

and is only 2% larger than the value at $Q^2 = 3 \text{ GeV}^2$. We take this value as our main result for the $I = 0$ $Z\gamma$ -mixing HVP function at large Q^2 .

6. Conclusions

In this paper we have presented a computation of the leading hadronic contribution to the running of the QED coupling α and of the electroweak mixing angle θ_W from first principles using lattice QCD.

For the QED coupling, our main result is presented in eqs. (46) and (47) in terms of a rational approximation of $\Delta\alpha_{\text{had}}(-Q^2)$ as a function of the space-like $Q^2 > 0$ up to $Q^2 \approx 7 \text{ GeV}^2$. Our results are slightly larger but still compatible with an earlier calculation by BMWc. However, there is a significant tension with the predictions based on the data-driven method. Since the tension is larger at lower Q^2 , where our result is most sensitive to the scale setting error, a new determination of the t_0 scale that is underway [147] will help clarify the significance of this tension.

Combining our result obtained in a Q^2 -range between 3 to 7 GeV^2 range with perturbative QCD, we obtain an estimate for $\Delta\alpha_{\text{had}}^{(5)}(M_Z^2)$ in eq. (56) that does not rely on any experimental data as input, except for the calibration of the lattice scale. Our estimate, based on the Euclidean split technique and the perturbative Adler function, is consistent with and of similar precision (i.e. 0.55%) as estimates employing the data-driven approach. Thus, the tension in $\Delta\alpha_{\text{had}}(-Q^2)$ observed between our results and the R -ratio is largely washed out when running the result up to the Z pole.

For the electroweak mixing angle θ_W , we also provide a description in terms of a rational function of $\Delta_{\text{had}} \sin^2 \theta_W(-Q^2)$ for Q^2 up to 7 GeV^2 (see eqs. (48) and (49)). Here we take advantage of the fact that the different flavor structure of the (vector part of the) weak neutral current with respect to the electromagnetic current is easily implemented in the lattice approach. This results in estimates for $\Delta_{\text{had}} \sin^2 \theta_W(-Q^2)$ with a similar error budget as that for $\Delta\alpha_{\text{had}}(-Q^2)$, which is a vast improvement over what can be obtained with the data-driven method which relies on a heuristic flavor separation affected by large systematic uncertainties. Specifically, in eq. (58) we provide a rational representation for the flavor-singlet mixing contribution $\bar{I}^{08}(Q^2)$, which for a large Q^2 tends to the constant value in eq. (60). This result can be used in comprehensive studies of the running of the electroweak mixing angle in combination with the experimental R -ratio data to reduce the systematics from the flavor separation.

Acknowledgements

We thank Gilberto Colangelo, Jens Erler, Rodolfo Ferro-Hernández, Tim Harris, Martin Hoferichter, Fred Jegerlehner, Daniel Mohler, Massimo Passera, Thomas Teubner and Arianna Toniato for valuable discussions. Further thanks go to Simon Kuberski for the determination of auxiliary data that were used in our analysis. We are grateful to Bogdan Malaescu and the authors of refs. [12, 137] for sharing their data for the running of α at $Q^2 > 0$. We thank Alex Keshavarzi and the authors of refs. [31, 138] for sharing the R -ratio data with covariance matrix, which were used to calculate tabulated data for the running of α at $Q^2 > 0$. Calculations for this project have been performed on the HPC clusters Clover and HIMster-II at Helmholtz Institute Mainz and Mogon-II at Johannes Gutenberg-Universität (JGU) Mainz, on the HPC systems JUQUEEN and JUWELS

at Jülich Supercomputing Centre (JSC), and on Hazel Hen at Höchstleistungsrechenzentrum Stuttgart (HLRS) [148]. The authors gratefully acknowledge the support of the Gauss Centre for Supercomputing (GCS) and the John von Neumann-Institut für Computing (NIC) for project HMZ21 and HMZ23 at JSC and project GCS-HQCD at HLRS. Our programs use the deflated SAP + GCR solver from the OPENQCD package [149, 150], as well as the QMP and QDP++ library [151]. Our data analysis has been performed using Python and the libraries NumPy [152], SciPy [153], pandas [154, 155], mpmath [156] and uncertainties [157], and using GNU Parallel [158]. Plots have been produced using Matplotlib [159]. We are grateful to our colleagues in the CLS initiative for sharing ensembles. This work has been supported by Deutsche Forschungsgemeinschaft (German Research Foundation, DFG) through project HI 2048/1-2 (project No. 399400745) and through the Cluster of Excellence “Precision Physics, Fundamental Interactions and Structure of Matter” (PRISMA+ EXC 2118/1), funded within the German Excellence strategy (Project ID 39083149). The work of M.C. has been supported by the European Union’s Horizon 2020 research and innovation program under the Marie Skłodowska-Curie Grant Agreement No. 843134. A.G. received funding from the Excellence Initiative of Aix-Marseille University - A*MIDEX, a French “Investissements d’Avenir” programme, AMX-18-ACE-005 and from the French National Research Agency under the contract ANR-20-CE31-0016.

A. Pseudoscalar meson and gradient flow observables

Thanks to the high statistics on the vector correlator, the results presented in section 3.8 have a better than 1% precision on $\bar{H}(-Q^2)$ for all ensembles. This is comparable to the statistical error of the meson masses and decay constants on the ensembles in table 1, therefore it is sensible

	am_π	am_K	af_π	af_K	t_0/a^2	$(w_0/a)^2$
H101	0.183 56(48)	0.183 56(48)	0.063 87(19)	0.063 87(19)	2.847(5)	3.694(9)
H102	0.154 57(55)	0.191 64(48)	0.060 35(29)	0.063 92(21)	2.881(6)	3.759(11)
H105	0.123 53(128)	0.202 51(87)	0.058 24(48)	0.064 46(33)	2.889(7)	3.779(14)
N101	0.122 36(47)	0.201 89(28)	0.057 48(23)	0.064 20(19)	2.890(2)	3.789(5)
C101	0.096 16(65)	0.205 78(32)	0.054 59(27)	0.063 42(15)	2.913(3)	3.836(6)
B450	0.161 08(43)	0.161 08(43)	0.056 43(16)	0.056 43(16)	3.663(8)	4.845(18)
S400	0.135 92(43)	0.170 56(38)	0.053 81(35)	0.057 01(26)	3.686(7)	4.895(15)
N451	0.110 89(29)	0.178 27(18)	0.052 16(16)	0.057 67(9)	3.682(2)	4.896(5)
D450	0.083 62(39)	0.183 93(18)	0.049 67(25)	0.057 41(11)	3.696(3)	4.933(6)
H200	0.136 33(47)	0.136 22(67)	0.047 50(26)	0.047 52(27)	5.151(16)	7.003(42)
N202	0.134 23(30)	0.134 21(29)	0.048 32(16)	0.048 33(16)	5.165(12)	7.020(29)
N203	0.112 66(23)	0.144 13(19)	0.046 34(12)	0.049 07(11)	5.146(6)	6.982(15)
N200	0.092 34(28)	0.150 76(21)	0.044 14(14)	0.049 07(14)	5.164(6)	7.040(14)
D200	0.065 15(28)	0.156 15(16)	0.042 17(12)	0.049 10(11)	5.179(3)	7.099(7)
E250	0.042 17(28)	0.159 24(8)	0.040 08(22)	0.048 52(10)	5.203(2)	7.176(6)
N300	0.106 18(24)	0.106 18(24)	0.038 03(13)	0.038 03(13)	8.544(19)	11.821(48)
N302	0.087 25(34)	0.113 73(32)	0.036 32(15)	0.038 54(15)	8.526(19)	11.784(49)
J303	0.064 81(23)	0.119 64(20)	0.034 28(11)	0.038 66(14)	8.621(10)	12.101(31)
E300	0.043 67(16)	0.123 72(13)	0.032 37(12)	0.038 17(23)	8.622(6)	12.163(15)

Table 8: Meson masses and decay constants, and reference scales t_0 and w_0^2 .

δ [%]	m_π	m_K	f_π	f_K
H101	0.012	0.012	-0.11	-0.11
H102	0.051	0.000	-0.23	-0.12
H105	0.145	0.000	-0.60	-0.25
N101	0.010	0.000	-0.04	-0.02
C101	0.038	0.000	-0.15	-0.06
B450	0.031	0.031	-0.28	-0.28
S400	0.114	0.000	-0.53	-0.29
N451	0.021	0.000	-0.09	-0.03
D450	0.013	0.000	-0.05	-0.02
H200	0.096	0.096	-0.86	-0.86
N202	0.005	0.005	-0.05	-0.05
N203	0.024	0.000	-0.11	-0.05
N200	0.070	0.000	-0.29	-0.12
D200	0.056	0.000	-0.22	-0.08
E250	0.031	0.000	-0.12	-0.05
N300	0.033	0.033	-0.29	-0.29
N302	0.131	0.000	-0.60	-0.31
J303	0.086	0.000	-0.35	-0.14
E300	0.041	0.000	-0.16	-0.06

Table 9: Finite-size effects on mesonic observables.

to include this source of uncertainty in the extrapolation to the physical point. To implement the strategy presented in section 4, we performed a dedicated computation of pseudoscalar density and axial current two-point functions, that we used to obtain m_π , m_K , f_π and f_K to subpercent precision. Crucially, this allows us to include the correlation between these observables and the values of $\bar{\Pi}(-Q^2)$ on the same ensemble into the analysis. The axial current is non-perturbatively $\mathcal{O}(a)$ -improved using c_A from ref. [160] and renormalized using Z_A and b_A from refs. [161, 162]. The values of the meson masses and decay constants are tabulated in table 8.

For a similar reason, we computed the gradient-flow quantities t_0 [70] and w_0 [163] that set the scale, entering in the Q^2 scale that is input in the kernel and in positioning of the ensemble in the (m_π, m_K) plane, see also figure 2. We use the same procedure as in ref. [67]. Specifically, to minimize the effect of boundary effects and additional discretization effects from the boundary, on open BCs ensembles we use only the value of the action density with clover-type discretization $E(t, t_{\text{fl}})$ on a single time slice at $t = T/2$. On periodic BCs ensembles the four-dimensional volume average is used. The values of t_0 and w_0^2 are also tabulated in table 8, and, in the case of t_0 , they agree within errors with the values quoted in refs. [66, 67]. In the following, we choose to use t_0 .

The meson masses and meson decay constants in table 8 are also affected by finite-size effects. These effects are reliably computed in χ P T [164] and listed in table 9. They amount to a positive, permil-level shift on the masses and a negative sub-percent shift on the decay constants.

B. Autocorrelation study

We employ the Γ -method [165, 166] to estimate the integrated autocorrelation time, τ_{int} associated to $\Delta\alpha$ for each ensemble. Then, we use this information to estimate a common bin size. Taking

bin size		τ_{int}	bin size		τ_{int}
H101	25	1.70(26)	H200	30	1.20(19)
H102	25	1.73(27)	N202	35	1.86(45)
H105	20	1.32(27)	N203	20	1.15(17)
N101	15	0.79(11)	N200	15	0.77(10)
C101	20	0.79(10)	D200	10	0.58(6)
<hr/>			<hr/>		
B450	25	1.45(24)	E250	5	0.47(4)
S400	20	2.17(32)	N300	40	3.36(67)
N451	10	0.73(10)	N302	30	2.07(33)
D450	5	0.55(7)	J303	20	1.41(26)
<hr/>			<hr/>		
			E300	20	1.07(22)

Table 10: Bin size and integrated autocorrelation time in units of saved configurations for each of the ensembles included in our study. Configurations are saved every 4 molecular dynamics units (MDUs) (2 trajectories of length 2 MDUs), except for J303, for which configurations are separated by 8 MDUs (4 trajectories).

into account all autocorrelations, the expected increase of the uncertainty is estimated as

$$\Delta\Pi/\Delta\Pi_{\text{naive}} = \sqrt{2 \cdot \tau_{\text{int}}}, \quad (61)$$

where $\Delta\Pi$ is the true standard deviation and $\Delta\Pi_{\text{naive}}$ is the uncertainty without taking into account autocorrelations. The next step is to plot the ratio $\Delta\Pi(B)/\Delta\Pi_{\text{naive}}$ vs. the bin size, B . For a similar analysis see ref. [167]. We find perfect agreement between (61) and the region where $\Delta\Pi(B)/\Delta\Pi_{\text{naive}}$ plateaus.

The noise of the correlator at long distances could, in principle, hide the autocorrelations, artificially reducing τ_{int} . To avoid this we repeat the analysis several times, each time discarding more time slices at the tail of the correlator. However, we found that the result is largely independent of the amount of noise removed. We also observe a clear trend to smaller bin sizes as the physical point is approached. While this effect is in apparent contrast with the expected $\sim 1/a^2$ scaling with lattice spacings [67], it is most likely explained with the noisier observables and shorter MC chains of ensembles at finer lattice spacings and lighter pion masses.

C. Treatment of quark-disconnected diagrams

In this appendix we collect further technical details regarding the evaluation of quark loops

$$L_{\mathcal{O}_f}(\vec{p}, t) = \sum_{\vec{x}} e^{i\vec{p}\cdot\vec{x}} \langle \mathcal{O}_f(\vec{x}, t) \rangle_F, \quad (62)$$

for some operator $\mathcal{O}_f(\vec{x}, t)$ involving a single quark flavor f , which represents the computationally most expensive part of this study. A simple all-to-all estimator can be constructed using stochastic (four-dimensional) volume sources ξ_i , $i = 1, \dots, N_s$ which satisfy

$$\mathbb{E}[\xi_i^\dagger \xi_j] = \delta_{ij}, \quad (63)$$

A simple estimator for the quark loop function in eq. (62) is then given by the average over N_s noise sources,

$$L_{\mathcal{O}_f}(\vec{p}, t) = \frac{1}{N_s} \sum_{s=1}^{N_s} \sum_{\vec{x}} e^{i\vec{p}\cdot\vec{x}} \text{tr} [\xi_s^\dagger \Gamma_{\mathcal{O}} (D_f)_{xx}^{-1} \xi_s], \quad (64)$$

where D_f denotes the Dirac operator for a single quark flavor and $\Gamma_{\mathcal{O}}$ the desired combination of Dirac matrices corresponding to a local (bilinear) operator $\mathcal{O}_f(x) = \bar{\psi}(x)\Gamma\psi(x)$. The generalization to non-local operators (i.e. point-split currents or operators involving derivatives) is straightforward and does not require additional inversions. However, the resulting statistical error for this naive estimator behaves as $1/\sqrt{N_s}$, implying an insufficient rate of convergence for many observables (e.g. vector currents) with respect to the computational cost required to saturate to gauge noise.

Therefore, we have computed the quark-disconnected loops using a variant of the method introduced in ref. [72] combining the one-end trick (OET) [73] with a combination of the generalized hopping parameter expansion (gHPE) [76] and hierarchical probing [77]. We write the difference between the quark loop function of operators \mathcal{O}_1 and \mathcal{O}_2 with different flavors (with different quark masses m_1 and m_2 respectively) using eq. (28) to get the OET estimator

$$L_{\mathcal{O}_1}(\vec{p}, t) - L_{\mathcal{O}_2}(\vec{p}, t) = (m_1 - m_2) \frac{1}{N_s} \sum_{s=1}^{N_s} \sum_{\vec{x}} \sum_y e^{i\vec{p}\cdot\vec{x}} \text{tr} [\xi_s^\dagger (D_2)_{yx}^{-1} \Gamma_{\mathcal{O}} (D_1)_{xy}^{-1} \xi_s], \quad (65)$$

where in the r.h.s. we have used the cyclic property of the trace and inserted the volume sources satisfying eq. (63) at the other end of the propagator product with respect to the local operator insertion. Using the OET is it possible to saturate to the gauge noise for all relevant observables using at most $\mathcal{O}(100)$ sources. Note that this does not require any spin or color dilution but is achieved with plain stochastic $4d$ sources, which greatly reduces the computational cost compared to e.g. plain hierarchical probing. Using the gHPE, cf. eqs. (29-30), we generalize the method of ref. [72] to apply also to point-split currents by evaluating the first term on the r.h.s. of eq. (29) using hierarchical probing on spin and color diluted stochastic volume sources. We find that $N_h = 512$ probing vectors are sufficient to reach gauge noise for non-local operators, while for local operators the saturation occurs already at $N_h = 32$. For the second term it is sufficient to use naive stochastic volume sources, and the required inversion can be reused in the evaluation of $\text{tr} [\Gamma(D_{N-1}^{-1} - D_N^{-1})]$, i.e. the last term of the chain of OET estimators. Regarding the order of the gHPE, we found a choice of $n = 2$ to be most effective. In practice, we use always four quark flavors, i.e. light, strange, an additional, intermediate valence quark and a charm valence quark. For the (bare) mass of the intermediate quark flavor i we found that the following choice for the value of the intermediate κ_i

$$\frac{1}{\kappa_i} = \frac{1 - X}{\kappa_s} + \frac{X}{\kappa_c}, \quad X = 1/4, \quad (66)$$

works well for our ensembles. The values for $\kappa_{s,c}$ are listed in table 11 and most of the values for the charm quark have been previously published in ref. [8]. We use 512 stochastic volume sources for the light quark and double this number for each heavier quark flavor. Moreover, we average over stochastic sources such that effectively four independent blocks remain, which we found to be an acceptable compromise between storage requirements and the resulting loss of effective statistics in (unbiased) estimators for e.g. the quark-disconnected contribution to meson two-point functions. Since certain other projects require position space data on large lattices such a compromise is needed, i.e. to keep overall storage consumption at a feasible level when storing lattice-wide objects involving all sixteen local operators. One-link displaced operators have only been stored in momentum space.

The resulting method is significantly more efficient than e.g. plain hierarchical probing as applied in refs. [8, 78]. While the statistical errors for the scalar, pseudoscalar and axial vector currents are very consistent between the two methods, this is not the case for the vector and tensor currents. Considering the products of variance $\sigma_{\mathcal{O},\text{vev}}^2$ and computational cost t , an

	κ_ℓ	κ_s	κ_i	κ_c	q_{\max}^2
H102	0.136 865	0.136 549 339	0.132 901 611 768 002 995 31	0.123 041	12
H105	0.136 970	0.136 340 79	0.132 812 391 061 451 851 62	0.123 244	12
N101	0.136 970	0.136 340 79	0.132 812 391 061 451 851 62	0.123 244	16
C101	0.137 030	0.136 222 041	0.132 761 760 906 907 502 03	0.123 361	16
S400	0.136 984	0.136 702 387	0.133 647 904 383 104 573 91	0.125 252	12
N451	0.137 061 6	0.136 548 077 1	0.133 590 334 051 988 036 99	0.125 439	25
D450	0.137 126	0.136 420 428 639 937	0.133 539 983 207 319 069 73	0.125 585	36
N203	0.137 080	0.136 840 284	0.134 438 580 455 760 296 63	0.127 714	16
N200	0.137 140	0.136 720 86	0.134 391 915 521 748 571 56	0.127 858	16
D200	0.137 200	0.136 601 748	0.134 340 862 017 844 683 60	0.127 986	16
E250	0.137 232 867	0.136 536 633	0.134 311 782 582 228 314 33	0.128 052	36
N302	0.137 064	0.136 872 179 135 8	0.135 153 490 631 909 189 61	0.130 247	16
J303	0.137 123	0.136 754 660 8	0.135 098 429 622 226 632 37	0.130 362	16
E300	0.137 163	0.136 675 163 617 732 7	0.135 059 004 501 960 048 51	0.130 432	36

Table 11: Values of (valence) $\kappa_{\ell,s,i,c}$ for the ensembles for which disconnected loops have been produced, together with the lattice momentum cutoff q_{\max}^2 in units of $(2\pi/L)^2$ up to which momentum space data has been saved for both local and one-link displaced operators.

operator-dependent, effective speedup $s_{\mathcal{O}}$ can be defined as the ratio of this quantity for the “old” (hierarchical probing) and the “new” (OET+gHPE+HP)-based method

$$s_{\mathcal{O}} = \frac{(\sigma_{\mathcal{O},\text{vev}}^2 t)_{\text{old}}}{(\sigma_{\mathcal{O},\text{vev}}^2 t)_{\text{new}}}, \quad (67)$$

where $\sigma_{\mathcal{O},\text{vev}}^2$ denotes the variance of the vacuum expectation values at zero-momentum, i.e. for the observable

$$\text{vev} = \sum_t \langle L_{\mathcal{O}}(\vec{0}, t) \rangle. \quad (68)$$

Assuming independent measurements (i.e. a sufficiently large set of gauge configurations), this ratio determines the difference in absolute computational cost for the two methods for a given statistical target precision. The results are shown in fig. 17 for the same set of operators and flavors. Depending on the observable this effective speedup reaches an order of magnitude. The largest difference between the two methods is observed for the $l-s$ combination of vector currents with an improvement of more than 17 in case of the conserved vector current.

D. Phenomenological model of the $\bar{\Pi}^{08}$ contribution

Modelling the $\bar{\Pi}^{08}$ contribution using experimental data as input requires some assumptions. In this appendix we describe the phenomenological model that we compare to the lattice result in figure 16. Using the definitions in eqs. (21),

$$G_{I=0}^{\gamma\gamma} = \frac{1}{3}G^{88} \simeq \frac{1}{18}G^\omega + \frac{1}{9}G^\phi, \quad G^{08} \simeq \frac{1}{2\sqrt{3}} [G^\omega - G^\phi], \quad (69)$$

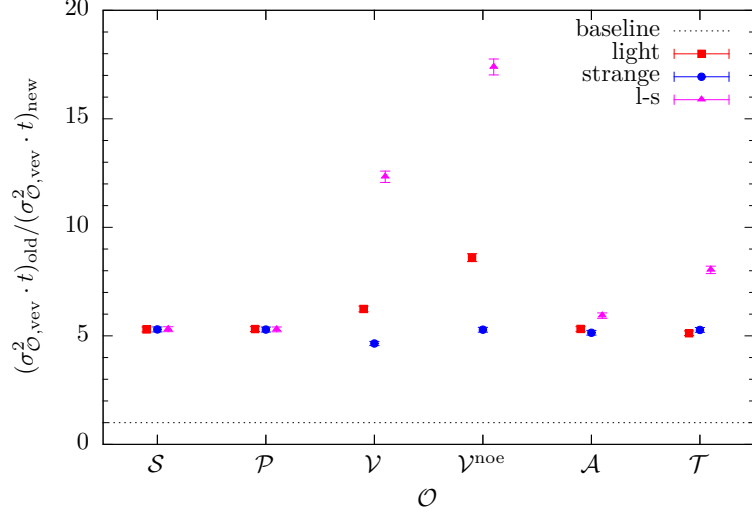


Figure 17: Speedup of the “new” (OET + gHPE + HP) method over the “old” (plain hierarchical probing) setup for scalar (\mathcal{S}), pseudoscalar (\mathcal{P}), vector (\mathcal{V}), conserved vector (\mathcal{V}^{noe}), axialvector (\mathcal{A}) and tensor (\mathcal{T}) quark bilinear operators. Results are shown for individual light and strange flavors as well as for the $l-s$ combination obtained directly from the OET. For operators that had reached gauge noise already for the old setup a speedup of roughly a factor five is obtained, while for the $l-s$ combination of the vector currents speedups of more than an order of magnitude are observed.

where $G^\omega = C^{\ell,\ell} + 2D^{\ell,\ell}$, $G^\phi = C^{s,s}$, and we neglected the disconnected diagram contributions $D^{\ell,s}$ and $D^{s,s}$. The $I = 0$ light and strange contributions are labeled with the vector meson that contributes the most to that channel, respectively the ω and the ϕ . Indeed, we can model the contribution to the hadronic cross-section in these channels with a narrow vector resonance contribution, plus the appropriate perturbative contribution

$$R_{I=0}^\ell(s) = \frac{1}{18} A_\omega m_\omega^2 \delta(s - m_\omega^2) + \theta(s - s_0) \frac{N_c}{18} (1 + \alpha_s/\pi), \quad (70)$$

$$R^s(s) = \frac{1}{9} A_\phi m_\phi^2 \delta(s - m_\phi^2) + \theta(s - s_1) \frac{N_c}{9} (1 + \alpha_s/\pi), \quad (71)$$

where the masses are $m_\omega = 782.65(12)$ MeV and $m_\phi = 1019.461(16)$ MeV [7]. The amplitudes A_ω and A_ϕ can be estimated observing that the contribution for a narrow resonance is proportional to its electronic decay width $\Gamma(V \rightarrow e^+e^-)$, resulting in

$$\frac{A_\omega}{18} = \frac{9\pi}{\alpha^2} \frac{\Gamma(\omega \rightarrow e^+e^-)}{m_\omega} = \frac{7.33(24)}{18}, \quad \frac{A_\phi}{9} = \frac{9\pi}{\alpha^2} \frac{\Gamma(\phi \rightarrow e^+e^-)}{m_\phi} = \frac{5.86(10)}{9}, \quad (72)$$

with $\Gamma(\omega \rightarrow e^+e^-) = 0.60(2)$ keV and $\Gamma(\phi \rightarrow e^+e^-) = 1.251(21)$ keV [7]. Setting $N_c = 3$, $\alpha_s = 0.30$ and the perturbative contribution thresholds $\sqrt{s_0} = 1.02$ GeV and $\sqrt{s_1} = 1.24$ GeV, eqs. (70) yield a respectively 50.2×10^{-10} and 53.4×10^{-10} for their contribution to $a_\mu^{\text{HVP,LO}}$. We can add these contributions to get 103.6×10^{-10} for the total uds isoscalar contribution to $a_\mu^{\text{HVP,LO}}$, where we have neglected the ℓ, s -type disconnected diagrams, consistent with the findings of ref. [168]. These numbers are in excellent agreement with lattice results [8]. We also

consider the exact sum rule for the spectral function of G^{08} ,

$$\int_0^\infty ds R^{08}(s) = \frac{1}{2\sqrt{3}} \left[A_\omega m_\omega^2 - A_\phi m_\phi^2 + N_c \left(1 + \frac{\alpha_s}{\pi} \right) (s_1 - s_0) \right] = 0, \quad (73)$$

where $R^{08}(s) = [18R_{I=0}^\ell(s) - 9R^s(s)]/(2\sqrt{3})$. This is satisfied within errors by the model, with the resonances contributing $-0.46(5) \text{ GeV}^2$ and the perturbative piece contributing 0.47 GeV^2 .

This gives us confidence in the model for the $\bar{\Pi}^{08}$ mixing function

$$\begin{aligned} \bar{\Pi}_{\text{model}}^{08}(-Q^2) &= \frac{Q^2}{12\pi^2} \int_0^\infty ds \frac{R^{08}(s)}{s(s+Q^2)} = \frac{1}{12\pi^2} \frac{1}{2\sqrt{3}} \\ &\times \left[A_\omega \frac{Q^2}{m_\omega^2 + Q^2} - A_\phi \frac{Q^2}{m_\phi^2 + Q^2} + N_c \left(1 + \frac{\alpha_s}{\pi} \right) \log \left(\frac{s_1(s_0 + Q^2)}{s_0(s_1 + Q^2)} \right) \right]. \quad (74) \end{aligned}$$

The perturbative contribution cancels except for differences in the light and strange quark thresholds, that leads to a finite contribution in the $Q^2 \rightarrow \infty$ limit. With the inclusion of a $\pm 100 \text{ MeV}$ correlated error in the $\sqrt{s_0}$ and $\sqrt{s_1}$ threshold that gives the error band in figure 16, the value is $\bar{\Pi}_{\text{pert.}}^{08} \rightarrow N_c(1 + \alpha_s/\pi) \log(s_1/s_0)/(12\pi^2 2\sqrt{3}) = 0.00313(28)$. Similarly, the ω and ϕ resonances contribution in the $Q^2 \rightarrow \infty$ limit is $\bar{\Pi}_{\omega,\phi}^{08} \rightarrow (A_\omega - A_\phi)/(12\pi^2 2\sqrt{3}) = 0.00357(64)$, for a total of $0.00669(70)$, with the $\mathcal{O}(10\%)$ error dominated by the experimental uncertainty on the ω and ϕ partial decay widths into e^+e^- . At $Q^2 = 7 \text{ GeV}^2$, our lattice result is $\bar{\Pi}^{08} = 0.00704(17)$ and very slowly varying with Q^2 , only 2% larger than the $Q^2 = 3 \text{ GeV}^2$ value, that makes it compatible with the model value but significantly more precise.

E. Phenomenological estimate of the charm quenching effect

Our goal in this appendix is to estimate the rough size of the effect of neglecting sea charm quarks on the running of α_{em} up to $Q_0^2 \approx 5 \text{ GeV}^2$. To this end, we may split up the subtracted vacuum polarisation into two terms,

$$\bar{\Pi}(-Q_0^2) = [\bar{\Pi}(-Q_0^2) - \bar{\Pi}(-1 \text{ GeV}^2)] + \bar{\Pi}(-1 \text{ GeV}^2). \quad (75)$$

The first term can be estimated using perturbation theory; the dynamical charm quark effects enter at order α_s^2 and is numerically small. For the second term, we will see that the contribution of the $D\bar{D}$ channels to the light-quark correlators amounts to a roughly one-permil effect if one neglects the virtuality dependence of the D -meson form factor.

We assume that the pion and kaon masses are used to set the (u, d, s) quark masses, and that the same low-energy scale-setting quantity is used in the $N_f = 2 + 1 + 1$ and the $N_f = 2 + 1$ theory. To be clear, we do not claim to have a quantitative estimate of the charm quenching effect on $\bar{\Pi}(-Q_0^2)$, which represents a non-perturbative problem. Rather, we have tried to identify some of the differences between the two theories and assume the size of these differences to be representative of the total quenching effect.

E.1. D meson loops

In the $N_f = 2 + 1 + 1$ theory, D^+D^- , $D^0\bar{D}^0$ and $D_s^+D_s^-$ pairs can contribute to the connected vector correlator of the (u, d, s) quarks, while these contributions are absent in the $N_f = 2 + 1$ theory. The real production of these heavy-light meson pairs makes a positive contribution to the

spectral function above the threshold of $\sqrt{s} = 2m_D$. The contribution to the R-ratio is

$$R_{D^+D^-}(s) = \frac{1}{4} \left(1 - \frac{4m_D^2}{s}\right)^{3/2} |F_{D^+}(s)|^2 \quad (76)$$

and a similar expression for the $D^0\bar{D}^0$ and $D_s^+D_s^-$ channels. Since the form factors F_D are not known precisely, we will set them to their values at $s = 0$, which amounts to treating these mesons in the scalar QED framework. With the form factors $F_{D^+}(s)$ and $F_{D_s^+}(s)$ set to $1/3$, since that is the charge of these mesons with respect to the (u, d, s) electromagnetic current, and similarly with $F_{D^0}(s)$ set to $-2/3$, we obtain for the subtracted HVP the contribution

$$\delta\bar{\Pi}^{\gamma\gamma}(-Q^2) = \frac{4}{9}f(Q^2/m_{D^0}^2) + \frac{1}{9}f(Q^2/m_{D^+}^2) + \frac{1}{9}f(Q^2/m_{D_s}^2), \quad (77)$$

with¹⁰

$$f(z) = \frac{1}{144\pi^2} \left[-8(1 + 3/z) + 3(1 + 4/z)^{3/2} \log\left(\frac{2 + z + \sqrt{z(4+z)}}{2}\right) \right]. \quad (78)$$

For $Q^2 = 1 \text{ GeV}^2$, we find

$$\delta\bar{\Pi}^{\gamma\gamma}(-1 \text{ GeV}^2) = 0.39 \times 10^{-4} \quad (79)$$

for the combined contribution of the $D_s^+D_s^-$, D^+D^- and $D^0\bar{D}^0$ channels. For comparison, the (u, d, s) -quark contribution to this quantity is roughly 0.040. Thus the contribution (79) represents a one-permil effect. For $Q^2 = 5 \text{ GeV}^2$, we find

$$\delta\bar{\Pi}^{\gamma\gamma}(-5 \text{ GeV}^2) = 1.81 \times 10^{-4}, \quad (80)$$

a 2.6 permil effect compared to about 0.070 for the (u, d, s) -quark contribution. In particular,

$$\delta\bar{\Pi}^{\gamma\gamma}(-1 \text{ GeV}^2) - \delta\bar{\Pi}^{\gamma\gamma}(-5 \text{ GeV}^2) = -1.42 \times 10^{-4}. \quad (81)$$

The numerical values provided here can be enhanced by the presence of $D\bar{D} 1^{--}$ resonances, such as the $\psi(3770)$; however, the latter is thought to be a ‘good $\bar{c}c$ resonance’, therefore having little coupling to the electromagnetic current carried by the (u, d, s) quarks. As an analogy, it may also be worth noting that the magnitude of the effective proton timelike form factor describing the cross-section $e^+e^- \rightarrow \bar{p}p$ starts at about 0.4 at threshold [169], and thus well below its value at $s = 0$.

The corresponding contribution for the running of the mixing angle is easily estimated considering the charges of the D mesons with respect to the weak isospin current, that results in

$$\delta\bar{\Pi}^{T_3\gamma}(-Q^2) = \frac{1}{12} [2f(Q^2/m_{D^0}^2) + f(Q^2/m_{D^+}^2) + f(Q^2/m_{D_s}^2)], \quad (82)$$

and using the relation $\delta\bar{\Pi}^{Z\gamma} = \delta\bar{\Pi}^{T_3\gamma} - \sin^2\theta_W\delta\bar{\Pi}^{\gamma\gamma}$.

E.2. Perturbative estimate

It is interesting to compare eq. (81) the difference of eqs. (79) and (80) to the purely perturbative prediction for the effect of unquenching the charm quark.

The required formulae for the contribution of heavy sea quarks to the spectral function of the (u, d, s) quarks can be found in ref. [170]. The ‘valence quarks’ (u, d, s) , i.e. those coupling to the electromagnetic current, are treated as massless. There is a virtual correction to the spectral

¹⁰For $z \rightarrow 0$, we have $f(z) = \frac{z}{480\pi^2} + \mathcal{O}(z^2)$.

function starting already at $s = 0$, and a contribution corresponding to the ‘real emission’ of a $\bar{c}c$ pair, which opens at $s = 4m^2$. Using the spectral representation, and setting $\alpha_s = 0.30$, $m_c = 1.25$ GeV we find

$$\bar{\Pi}^{\gamma\gamma}(-1 \text{ GeV}^2) - \bar{\Pi}^{\gamma\gamma}(-5 \text{ GeV}^2) = -0.19 \times 10^{-4}. \quad (83)$$

This prediction is about seven times smaller than the prediction in eq. (81) based on the D -meson loops treated in the scalar QED framework.

E.3. Change in the ω and ϕ masses and decays constants due to mixing with J/ψ

A further non-perturbative effect to be expected in QCD with dynamical charm quarks is a small shift in the masses and decay constants of the ω and ϕ mesons, relative to their respective values in QCD without dynamical charm quarks. Simply speaking, this may be viewed as a result of the ω and ϕ mixing with the J/ψ and possibly higher vector charmonium mesons. Parametrically, this effect is of order $1/m_{J/\psi}^2$, with a significant additional suppression associated with the small rate at which J/ψ decays. Even the mixing of the ω and ϕ mesons among themselves is known to be very small in the single flavor quark basis; see for instance the recent article [171] on this topic and references therein. Since it is difficult to isolate and quantitatively estimate the effect, we refrain from doing so here.

E.4. Synthesis

The largest potential charm-quenching correction we have identified comes from the D -meson loop, assuming conservatively virtuality-independent form factors. We will therefore use that correction as the basis of our estimate for the overall systematic uncertainty associated with the neglect of dynamical charm quark effects. Specifically, we will use eqs. (77)–(78) to estimate the charm-quenching error. As for the sign of the effect of quenching the charm quark, we remark that the specific effects considered in sections E.1 and E.2 both lead to $\bar{\Pi}(-Q^2)$ in the $N_f = 2 + 1$ theory being slightly underestimated. Nevertheless, we will quote symmetric systematic errors, since we are unable to perform a complete analysis.

As a final remark, we have not addressed the quark-disconnected contributions to the electromagnetic-current correlator involving one charm quark, i.e. $2 \langle j_\mu^8 j_\nu^c \rangle / (3\sqrt{3})$. At least in perturbation theory, such contributions are of order α_s^3 , i.e. of higher order than those considered in section E.2.

F. Extended table of results at the physical point

The results for the $\bar{\Pi}^{33}$, $\bar{\Pi}^{88}$, $\bar{\Pi}^{08}$ and $\bar{\Pi}^{cc}$, and for the total HVP contribution to the running of α and $\sin^2 \theta_W$, extrapolated to the physical point as explained in section 4, are given in tables 12 and 13 respectively for all the values of Q^2 sampled.

Table 12: Results for the $\bar{\Pi}^{33}$, $\bar{\Pi}^{88}$, $\bar{\Pi}^{08}$ and $\bar{\Pi}^{cc}$ HVP contribution extrapolated to the physical point for all the values of Q^2 sampled. The first quoted uncertainty is the statistical error, the second is the systematic error from varying the fit model estimated in section 4.1.1, the third is the scale-setting error (see section 4.2.1), and the fourth is the systematic from missing charm sea-quark loops (see section 4.2.2). The final uncertainty, quoted in square brackets, is the combination of the previous ones.

Q^2 [GeV ²]	$t_0 Q^2$	$\bar{\Pi}^{33}$	$\bar{\Pi}^{88}$	$\bar{\Pi}^{08}$	$\bar{\Pi}^{cc}$
0.01	0.005 53	0.000 904(14)(11) (7)(0)[19]	0.000 449 (6)(0) (5)(0) [7]	0.000 209 (6)(0) (9)(0)[11]	0.000 042 4(2)(1) (9)(-)[9]
0.015	0.008 29	0.001 342(20)(16)(10)(0)[28]	0.000 670 (8)(0) (7)(0)[11]	0.000 310 (9)(0)(13)(0)[15]	0.000 063 6(3)(1)(13)(-)[14]
0.02	0.011 06	0.001 77 (3) (2) (1)(0) [4]	0.000 888(11)(0) (9)(1)[14]	0.000 409(12)(0)(17)(0)[20]	0.000 084 7(4)(1)(18)(-)[18]
0.025	0.013 82	0.002 19 (3) (3) (2)(0) [4]	0.001 103(13)(0)(11)(1)[18]	0.000 506(14)(0)(20)(0)[25]	0.000 105 9(5)(1)(22)(-)[22]
0.03	0.016 59	0.002 61 (4) (3) (2)(0) [5]	0.001 316(16)(0)(13)(1)[21]	0.000 601(17)(0)(24)(0)[29]	0.000 127 0(6)(2)(26)(-)[27]
0.035	0.019 35	0.003 01 (4) (4) (2)(0) [6]	0.001 526(18)(0)(15)(1)[24]	0.000 694(19)(0)(28)(0)[34]	0.000 148 1(7)(2)(31)(-)[32]
0.04	0.022 12	0.003 41 (5) (4) (2)(0) [7]	0.001 735(20)(1)(17)(1)[27]	0.000 79 (2)(0) (3)(0) [4]	0.000 169 (1)(0) (3)(-)[4]
0.045	0.024 88	0.003 80 (5) (4) (2)(0) [7]	0.001 940(22)(1)(19)(1)[29]	0.000 88 (2)(0) (3)(0) [4]	0.000 190 (1)(0) (4)(-)[4]
0.05	0.027 64	0.004 18 (6) (5) (3)(0) [8]	0.002 144(25)(1)(21)(1)[32]	0.000 96 (3)(0) (4)(0) [5]	0.000 211 (1)(0) (4)(-)[4]
0.055	0.030 41	0.004 55 (6) (5) (3)(0) [9]	0.002 345(27)(1)(23)(2)[35]	0.001 05 (3)(0) (4)(0) [5]	0.000 232 (1)(0) (5)(-)[5]
0.06	0.033 17	0.004 92 (7) (6) (3)(0) [9]	0.002 54 (3)(0) (2)(0) [4]	0.001 13 (3)(0) (4)(0) [5]	0.000 253 (1)(0) (5)(-)[5]
0.065	0.035 9	0.005 28 (7) (6) (3)(0)[10]	0.002 74 (3)(0) (3)(0) [4]	0.001 22 (3)(0) (5)(0) [6]	0.000 274 (1)(0) (6)(-)[6]
0.07	0.038 7	0.005 64 (7) (6) (3)(0)[10]	0.002 94 (3)(0) (3)(0) [4]	0.001 30 (3)(0) (5)(0) [6]	0.000 296 (1)(0) (6)(-)[6]
0.075	0.041 5	0.005 98 (8) (6) (3)(0)[11]	0.003 13 (3)(0) (3)(0) [5]	0.001 38 (4)(0) (5)(0) [6]	0.000 317 (1)(0) (7)(-)[7]
0.08	0.044 2	0.006 33 (8) (7) (3)(0)[11]	0.003 32 (4)(0) (3)(0) [5]	0.001 45 (4)(0) (6)(0) [7]	0.000 337 (2)(0) (7)(-)[7]
0.085	0.047 0	0.006 66 (8) (7) (4)(0)[12]	0.003 51 (4)(0) (3)(0) [5]	0.001 53 (4)(0) (6)(0) [7]	0.000 358 (2)(1) (7)(-)[8]
0.09	0.049 8	0.006 99 (9) (7) (4)(0)[12]	0.003 69 (4)(0) (4)(0) [5]	0.001 60 (4)(0) (6)(0) [7]	0.000 379 (2)(1) (8)(-)[8]
0.095	0.052 5	0.007 32 (9) (8) (4)(0)[12]	0.003 88 (4)(0) (4)(0) [5]	0.001 68 (4)(0) (6)(0) [8]	0.000 400 (2)(1) (8)(-)[9]
0.1	0.055 3	0.007 64 (9) (8) (4)(0)[13]	0.004 06 (4)(0) (4)(0) [6]	0.001 75 (4)(0) (7)(0) [8]	0.000 421 (2)(1) (9)(-)[9]
0.12	0.066 3	0.008 86 (10) (9) (4)(0)[14]	0.004 78 (5)(0) (4)(0) [7]	0.002 02 (5)(0) (7)(0) [9]	0.000 505 (2)(1)(10)(-)[11]
0.14	0.077 4	0.010 01 (11) (9) (5)(0)[15]	0.005 46 (5)(0) (5)(0) [7]	0.002 28 (5)(0) (8)(0)[10]	0.000 588 (3)(1)(12)(-)[12]
0.16	0.088 5	0.011 09 (12)(10) (5)(0)[16]	0.006 13 (6)(0) (6)(0) [8]	0.002 51 (6)(0) (9)(0)[11]	0.000 671 (3)(1)(14)(-)[14]
0.18	0.099 5	0.012 11 (12)(10) (5)(1)[17]	0.006 76 (6)(1) (6)(1) [9]	0.002 73 (6)(0)(10)(0)[11]	0.000 754 (4)(1)(15)(-)[16]
0.2	0.110 6	0.013 08 (13)(10) (6)(1)[17]	0.007 38 (6)(1) (7)(1) [9]	0.002 94 (6)(0)(10)(0)[12]	0.000 837 (4)(1)(17)(-)[18]
0.22	0.121 6	0.014 00 (13)(11) (6)(1)[18]	0.007 98 (7)(1) (7)(1)[10]	0.003 13 (6)(0)(11)(0)[12]	0.000 919 (4)(1)(19)(-)[19]
0.24	0.132 7	0.014 87 (14)(11) (7)(1)[19]	0.008 55 (7)(1) (8)(1)[10]	0.003 31 (7)(0)(11)(0)[13]	0.001 002 (5)(1)(20)(-)[21]

continued

Table 12: (continued)

Q^2 [GeV ²]	$t_0 Q^2$	$\bar{\Pi}^{33}$	$\bar{\Pi}^{88}$	$\bar{\Pi}^{08}$	$\bar{\Pi}^{cc}$
0.26	0.1437	0.01570 (14)(11) (7)(1)[19]	0.00911 (7)(1) (8)(1)[11]	0.00348 (7)(0)(12)(0)[13]	0.001084 (5)(2)(22)(-)[23]
0.28	0.1548	0.01649 (14)(11) (8)(1)[19]	0.00965 (7)(1) (9)(1)[12]	0.00364 (7)(0)(12)(0)[14]	0.001165 (5)(2)(24)(-)[24]
0.3	0.1659	0.01725 (14)(11) (8)(1)[20]	0.01017 (7)(1) (9)(1)[12]	0.00378 (7)(0)(12)(0)[14]	0.001247 (6)(2)(25)(-)[26]
0.32	0.1769	0.01797 (15)(11) (9)(1)[20]	0.01068 (7)(1)(10)(1)[12]	0.00392 (7)(0)(13)(0)[14]	0.001328 (6)(2)(27)(-)[28]
0.34	0.1880	0.01867 (15)(11) (9)(1)[20]	0.01118 (8)(1)(10)(1)[13]	0.00405 (7)(0)(13)(0)[15]	0.001410 (6)(2)(29)(-)[30]
0.36	0.1990	0.01934 (15)(11) (9)(1)[21]	0.01166 (8)(1)(11)(1)[13]	0.00417 (7)(0)(13)(0)[15]	0.001490 (7)(2)(30)(-)[31]
0.38	0.2101	0.01999 (15)(11)(10)(1)[21]	0.01213 (8)(1)(11)(1)[14]	0.00429 (7)(0)(13)(0)[15]	0.001571 (7)(2)(32)(-)[33]
0.4	0.2212	0.02061 (15)(11)(10)(1)[21]	0.01259 (8)(1)(11)(1)[14]	0.00440 (7)(0)(14)(0)[15]	0.001652 (7)(2)(33)(-)[34]
0.42	0.2322	0.02121 (15)(11)(11)(1)[22]	0.01303 (8)(1)(12)(1)[14]	0.00450 (7)(0)(14)(0)[16]	0.00173 (1)(0) (4)(-)[4]
0.44	0.2433	0.02178 (15)(11)(11)(1)[22]	0.01346 (8)(1)(12)(1)[15]	0.00460 (7)(0)(14)(0)[16]	0.00181 (1)(0) (4)(-)[4]
0.46	0.2543	0.02234 (16)(11)(12)(1)[22]	0.01389 (8)(1)(12)(1)[15]	0.00469 (7)(0)(14)(0)[16]	0.00189 (1)(0) (4)(-)[4]
0.48	0.2654	0.02288 (16)(11)(12)(1)[23]	0.01430 (8)(2)(13)(1)[15]	0.00478 (7)(0)(14)(0)[16]	0.00197 (1)(0) (4)(-)[4]
0.5	0.2764	0.02341 (16)(11)(13)(1)[23]	0.01470 (8)(2)(13)(1)[16]	0.00486 (7)(0)(14)(0)[16]	0.00205 (1)(0) (4)(-)[4]
0.55	0.3041	0.02465 (16)(11)(14)(2)[24]	0.01567 (8)(2)(14)(2)[16]	0.00505 (7)(0)(15)(0)[16]	0.00225 (1)(0) (5)(-)[5]
0.6	0.3317	0.02580 (16)(11)(15)(2)[24]	0.01659 (8)(2)(15)(2)[17]	0.00522 (7)(0)(15)(0)[17]	0.00245 (1)(0) (5)(-)[5]
0.65	0.359	0.02688 (16)(11)(16)(2)[25]	0.01745 (9)(2)(15)(2)[18]	0.00537 (7)(0)(15)(0)[17]	0.00264 (1)(0) (5)(-)[5]
0.7	0.387	0.02789 (16)(11)(17)(2)[26]	0.01828 (9)(2)(16)(2)[18]	0.00550 (7)(0)(15)(0)[17]	0.00283 (1)(0) (6)(-)[6]
0.75	0.415	0.02884 (16)(10)(17)(2)[26]	0.01906 (9)(2)(16)(2)[19]	0.00562 (7)(0)(15)(0)[17]	0.00303 (1)(0) (6)(-)[6]
0.8	0.442	0.02973 (16)(10)(18)(2)[27]	0.01981 (9)(2)(17)(2)[19]	0.00573 (7)(0)(15)(0)[17]	0.00322 (1)(0) (6)(-)[7]
0.85	0.470	0.03058 (17)(10)(19)(3)[27]	0.02053 (9)(3)(17)(2)[20]	0.00582 (8)(0)(15)(0)[17]	0.00341 (2)(0) (7)(-)[7]
0.9	0.498	0.03138 (17)(10)(20)(3)[28]	0.02122 (9)(3)(18)(2)[20]	0.00591 (8)(0)(15)(0)[17]	0.00360 (2)(0) (7)(-)[7]
0.95	0.525	0.03214 (17)(10)(20)(3)[28]	0.02188 (9)(3)(18)(3)[21]	0.00599 (8)(0)(15)(0)[17]	0.00379 (2)(1) (7)(-)[8]
1.0	0.553	0.03287 (17)(10)(21)(3)[29]	0.02251 (9)(3)(19)(3)[21]	0.00606 (8)(0)(15)(0)[17]	0.00397 (2)(1) (8)(-)[8]
1.05	0.581	0.03357 (17)(10)(22)(3)[29]	0.02312 (9)(3)(19)(3)[22]	0.00612 (8)(0)(15)(0)[17]	0.00416 (2)(1) (8)(-)[8]
1.1	0.608	0.03423 (17) (9)(22)(3)[30]	0.02371 (9)(3)(20)(3)[22]	0.00618 (8)(0)(15)(0)[17]	0.00434 (2)(1) (8)(-)[9]
1.15	0.636	0.03487 (17) (9)(23)(3)[30]	0.02428 (9)(3)(20)(3)[23]	0.00623 (8)(0)(15)(0)[17]	0.00453 (2)(1) (9)(-)[9]
1.2	0.663	0.03548 (17) (9)(24)(4)[31]	0.02482 (9)(3)(21)(3)[23]	0.00628 (8)(0)(15)(0)[17]	0.00471 (2)(1) (9)(-)[9]
1.25	0.691	0.03607 (17) (9)(24)(4)[31]	0.02535 (10)(3)(21)(3)[24]	0.00633 (8)(0)(15)(0)[17]	0.00489 (2)(1) (9)(-)[10]
1.3	0.719	0.03663 (17) (9)(25)(4)[32]	0.02586 (10)(3)(22)(4)[24]	0.00637 (8)(0)(15)(0)[17]	0.00507 (2)(1)(10)(-)[10]

continued

Table 12: (continued)

Q^2 [GeV ²]	$t_0 Q^2$	$\bar{\Pi}^{33}$	$\bar{\Pi}^{88}$	$\bar{\Pi}^{08}$	$\bar{\Pi}^{cc}$
1.35	0.746	0.037 18 (17) (9)(25)(4)[32]	0.026 36 (10)(4)(22)(4)[25]	0.006 41 (8)(0)(15)(0)[17]	0.005 25 (2)(1)(10)(-)[10]
1.4	0.774	0.037 70 (17) (9)(26)(4)[33]	0.026 84 (10)(4)(23)(4)[25]	0.006 44 (8)(0)(15)(0)[17]	0.005 43 (2)(1)(11)(-)[11]
1.45	0.802	0.038 21 (17) (8)(27)(4)[33]	0.027 31 (10)(4)(23)(4)[26]	0.006 48 (8)(0)(15)(0)[17]	0.005 61 (2)(1)(11)(-)[11]
1.5	0.829	0.038 70 (17) (8)(27)(4)[34]	0.027 76 (11)(4)(23)(4)[26]	0.006 51 (8)(0)(15)(0)[17]	0.005 78 (2)(1)(11)(-)[11]
1.55	0.857	0.039 18 (18) (8)(28)(5)[34]	0.028 20 (11)(4)(24)(4)[27]	0.006 53 (8)(0)(15)(0)[17]	0.005 96 (3)(1)(11)(-)[12]
1.6	0.885	0.039 64 (18) (8)(28)(5)[35]	0.028 63 (11)(4)(24)(4)[27]	0.006 56 (8)(0)(15)(0)[17]	0.006 13 (3)(1)(12)(-)[12]
1.65	0.912	0.040 09 (18) (8)(29)(5)[35]	0.029 05 (12)(4)(25)(5)[28]	0.006 59 (8)(0)(15)(0)[17]	0.006 30 (3)(1)(12)(-)[12]
1.7	0.940	0.040 5 (2) (1) (3)(0) [4]	0.029 45 (13)(4)(25)(5)[29]	0.006 61 (8)(0)(15)(0)[17]	0.006 48 (3)(1)(12)(-)[13]
1.75	0.968	0.040 9 (2) (1) (3)(1) [4]	0.029 85 (13)(4)(25)(5)[29]	0.006 63 (8)(0)(15)(0)[17]	0.006 65 (3)(1)(13)(-)[13]
1.8	0.995	0.041 4 (2) (1) (3)(1) [4]	0.030 23 (14)(5)(26)(5)[30]	0.006 65 (8)(0)(15)(0)[17]	0.006 82 (3)(1)(13)(-)[13]
1.85	1.023	0.041 8 (2) (1) (3)(1) [4]	0.030 61 (15)(5)(26)(5)[31]	0.006 67 (8)(0)(15)(0)[17]	0.006 99 (3)(1)(13)(-)[14]
1.9	1.050	0.042 1 (2) (1) (3)(1) [4]	0.030 98 (15)(5)(26)(5)[31]	0.006 69 (8)(0)(15)(0)[17]	0.007 16 (3)(1)(14)(-)[14]
1.95	1.078	0.042 5 (2) (1) (3)(1) [4]	0.031 34 (16)(5)(27)(5)[32]	0.006 70 (8)(0)(15)(0)[17]	0.007 32 (3)(1)(13)(-)[14]
2.0	1.106	0.042 9 (2) (1) (3)(1) [4]	0.031 69 (17)(5)(27)(5)[33]	0.006 72 (8)(0)(15)(0)[17]	0.007 49 (3)(1)(14)(-)[14]
2.1	1.161	0.043 6 (2) (1) (3)(1) [4]	0.032 37 (20)(5)(28)(6)[35]	0.006 75 (8)(0)(15)(0)[17]	0.007 82 (3)(1)(14)(-)[15]
2.2	1.216	0.044 3 (2) (1) (3)(1) [4]	0.033 0 (2)(1) (3)(1) [4]	0.006 77 (8)(0)(15)(0)[17]	0.008 15 (3)(1)(15)(-)[15]
2.3	1.272	0.044 9 (3) (1) (3)(1) [4]	0.033 6 (3)(1) (3)(1) [4]	0.006 80 (8)(0)(15)(0)[17]	0.008 47 (3)(1)(16)(-)[16]
2.4	1.327	0.045 5 (3) (0) (4)(1) [5]	0.034 2 (3)(1) (3)(1) [4]	0.006 82 (8)(0)(15)(0)[17]	0.008 79 (4)(1)(16)(-)[16]
2.5	1.382	0.046 1 (3) (0) (4)(1) [5]	0.034 8 (3)(1) (3)(1) [5]	0.006 84 (8)(0)(15)(0)[17]	0.009 10 (4)(1)(17)(-)[17]
2.6	1.437	0.046 7 (3) (0) (4)(1) [5]	0.035 4 (3)(1) (3)(1) [5]	0.006 85 (8)(0)(15)(0)[17]	0.009 42 (4)(1)(17)(-)[17]
2.7	1.493	0.047 3 (4) (0) (4)(1) [5]	0.035 9 (4)(1) (3)(1) [5]	0.006 87 (8)(0)(15)(0)[17]	0.009 73 (4)(1)(17)(-)[18]
2.8	1.548	0.047 8 (4) (0) (4)(1) [6]	0.036 4 (4)(1) (3)(1) [5]	0.006 88 (8)(0)(15)(0)[17]	0.010 03 (4)(1)(18)(-)[18]
2.9	1.603	0.048 3 (4) (0) (4)(1) [6]	0.036 9 (4)(1) (3)(1) [6]	0.006 89 (8)(0)(15)(0)[17]	0.010 34 (4)(1)(19)(-)[19]
3.0	1.659	0.048 8 (5) (0) (4)(1) [6]	0.037 4 (5)(1) (3)(1) [6]	0.006 90 (8)(0)(15)(0)[17]	0.010 64 (4)(1)(19)(-)[19]
3.1	1.714	0.049 2 (5) (0) (4)(1) [6]	0.037 8 (5)(1) (4)(1) [6]	0.006 91 (8)(0)(15)(0)[17]	0.010 93 (4)(1)(19)(-)[20]
3.2	1.769	0.049 7 (5) (0) (4)(1) [6]	0.038 3 (5)(1) (4)(1) [6]	0.006 92 (8)(0)(15)(0)[17]	0.011 23 (4)(1)(20)(-)[20]
3.3	1.825	0.050 1 (5) (0) (4)(1) [7]	0.038 7 (5)(1) (4)(1) [7]	0.006 93 (8)(0)(15)(1)[17]	0.011 52 (4)(1)(20)(-)[20]
3.4	1.880	0.050 6 (5) (0) (4)(1) [7]	0.039 1 (5)(1) (4)(1) [7]	0.006 94 (8)(0)(15)(1)[17]	0.011 81 (5)(1)(21)(-)[21]
3.5	1.935	0.051 0 (5) (0) (4)(1) [7]	0.039 5 (6)(1) (4)(1) [7]	0.006 95 (8)(0)(15)(1)[17]	0.012 09 (4)(1)(21)(-)[21]

continued

Table 12: (continued)

Q^2 [GeV ²]	$t_0 Q^2$	$\bar{\Pi}^{33}$				$\bar{\Pi}^{88}$				$\bar{\Pi}^{08}$				$\bar{\Pi}^{cc}$			
3.6	1.990	0.051 4	(6)	(0)	(4)(1)	[7]	0.039 9	(6)(1)	(4)(1)	[7]	0.006 95	(8)(0)(15)(1)	[17]	0.012 38	(5)(1)(21)(-)	[22]	
3.7	2.046	0.051 8	(6)	(0)	(4)(1)	[7]	0.040 3	(6)(1)	(4)(1)	[7]	0.006 96	(8)(0)(15)(1)	[17]	0.012 66	(5)(2)(22)(-)	[22]	
3.8	2.101	0.052 1	(6)	(0)	(4)(1)	[7]	0.040 7	(6)(1)	(4)(1)	[7]	0.006 97	(8)(0)(15)(1)	[17]	0.012 94	(5)(2)(22)(-)	[23]	
3.9	2.156	0.052 5	(6)	(0)	(4)(1)	[7]	0.041 0	(6)(1)	(4)(1)	[7]	0.006 97	(8)(0)(15)(1)	[17]	0.013 21	(5)(2)(23)(-)	[23]	
4.0	2.212	0.052 9	(6)	(0)	(4)(1)	[7]	0.041 4	(6)(1)	(4)(1)	[7]	0.006 98	(8)(0)(15)(1)	[17]	0.013 48	(5)(2)(23)(-)	[24]	
4.1	2.267	0.053 2	(6)	(0)	(4)(1)	[8]	0.041 7	(6)(1)	(4)(1)	[7]	0.006 98	(8)(0)(15)(1)	[17]	0.013 75	(5)(2)(23)(-)	[24]	
4.2	2.322	0.053 6	(6)	(0)	(4)(1)	[8]	0.042 1	(6)(1)	(4)(1)	[7]	0.006 98	(8)(0)(15)(1)	[17]	0.014 02	(5)(2)(24)(-)	[24]	
4.3	2.377	0.053 9	(6)	(0)	(4)(1)	[8]	0.042 4	(6)(1)	(4)(1)	[8]	0.006 99	(8)(0)(15)(1)	[17]	0.014 29	(5)(2)(24)(-)	[25]	
4.4	2.433	0.054 2	(6)	(0)	(4)(1)	[8]	0.042 7	(6)(1)	(4)(1)	[8]	0.006 99	(8)(0)(15)(1)	[17]	0.014 55	(5)(2)(25)(-)	[25]	
4.5	2.488	0.054 5	(6)	(0)	(4)(1)	[8]	0.043 0	(6)(1)	(4)(1)	[8]	0.007 00	(8)(0)(15)(1)	[17]	0.014 81	(5)(2)(25)(-)	[25]	
4.6	2.543	0.054 9	(6)	(0)	(4)(1)	[8]	0.043 4	(6)(1)	(4)(1)	[8]	0.007 00	(8)(0)(15)(1)	[17]	0.015 07	(5)(2)(25)(-)	[26]	
4.7	2.599	0.055 2	(6)	(0)	(4)(1)	[8]	0.043 7	(6)(1)	(4)(1)	[8]	0.007 00	(8)(0)(15)(1)	[17]	0.015 32	(5)(2)(26)(-)	[26]	
4.8	2.654	0.055 5	(6)	(0)	(4)(1)	[8]	0.044 0	(6)(1)	(4)(1)	[8]	0.007 00	(8)(0)(15)(1)	[17]	0.015 58	(5)(2)(26)(-)	[26]	
4.9	2.709	0.055 8	(6)	(0)	(4)(1)	[8]	0.044 2	(6)(1)	(4)(1)	[8]	0.007 01	(8)(0)(15)(1)	[17]	0.015 83	(5)(2)(26)(-)	[27]	
5.0	2.764	0.056 0	(6)	(0)	(5)(1)	[8]	0.044 5	(6)(1)	(4)(1)	[8]	0.007 01	(8)(0)(15)(1)	[17]	0.016 08	(6)(2)(26)(-)	[27]	
5.2	2.875	0.056 6	(6)	(0)	(5)(1)	[8]	0.045 1	(6)(1)	(4)(1)	[8]	0.007 01	(8)(0)(15)(1)	[17]	0.016 57	(6)(2)(27)(-)	[27]	
5.4	2.986	0.057 1	(6)	(0)	(5)(1)	[8]	0.045 6	(6)(1)	(4)(1)	[8]	0.007 02	(8)(0)(15)(1)	[17]	0.017 06	(6)(2)(28)(-)	[28]	
5.6	3.096	0.057 7	(6)	(0)	(5)(2)	[8]	0.046 1	(6)(1)	(4)(1)	[8]	0.007 02	(8)(0)(15)(1)	[17]	0.017 53	(6)(2)(28)(-)	[28]	
5.8	3.207	0.058 2	(6)	(0)	(5)(2)	[8]	0.046 6	(6)(1)	(4)(1)	[8]	0.007 03	(8)(0)(15)(1)	[17]	0.018 00	(6)(2)(28)(-)	[29]	
6.0	3.317	0.058 6	(6)	(0)	(5)(2)	[8]	0.047 1	(6)(1)	(4)(2)	[8]	0.007 03	(8)(0)(15)(1)	[17]	0.018 46	(6)(2)(29)(-)	[29]	
6.2	3.428	0.059 1	(6)	(0)	(5)(2)	[8]	0.047 6	(7)(1)	(4)(2)	[8]	0.007 03	(8)(0)(15)(1)	[17]	0.018 92	(6)(2)(30)(-)	[30]	
6.4	3.538	0.059 6	(6)	(0)	(5)(2)	[8]	0.048 0	(6)(1)	(4)(2)	[8]	0.007 03	(8)(0)(15)(1)	[17]	0.019 36	(7)(2)(30)(-)	[31]	
6.6	3.65	0.060 0	(6)	(0)	(5)(2)	[8]	0.048 5	(6)(1)	(4)(2)	[8]	0.007 04	(8)(0)(15)(1)	[17]	0.019 80	(7)(2)(31)(-)	[31]	
6.8	3.76	0.060 4	(6)	(0)	(5)(2)	[8]	0.048 9	(6)(1)	(4)(2)	[8]	0.007 04	(8)(0)(15)(1)	[17]	0.020 24	(6)(2)(31)(-)	[32]	
7.0	3.87	0.060 8	(6)	(0)	(5)(2)	[8]	0.049 3	(6)(1)	(4)(2)	[8]	0.007 04	(8)(0)(15)(1)	[17]	0.020 66	(7)(2)(31)(-)	[32]	

Table 13: Results for the total HVP contribution to the running of α and $\sin^2 \theta_W$ extrapolated to the physical point for all the values of Q^2 sampled. Following the statistical error, and the systematic errors from varying the fit model estimated, scale-setting and missing charm sea-quark loops, the fifth uncertainty is the systematic error from missing isospin-breaking effects (see section 4.2.3). The final uncertainty, quoted in square brackets, is the combination of the previous ones.

Q^2 [GeV ²]	$t_0 Q^2$	$\Delta\alpha_{\text{had}}$	$\Delta_{\text{had}} \sin^2 \theta_W$
0.01	0.005 53	0.000 098 4(13)(10) (8)(0) (3)[19]	-0.000 099 2(15)(11) (7)(0)(0)[20]
0.015	0.008 29	0.000 146 2(20)(15)(11)(1) (4)[27]	-0.000 147 3(22)(17)(10)(1)(0)[29]
0.02	0.011 06	0.000 193 (3) (2) (1)(0) (1) [4]	-0.000 195 (3) (2) (1)(0)(0) [4]
0.025	0.013 82	0.000 239 (3) (2) (2)(0) (1) [4]	-0.000 241 (3) (3) (2)(0)(0) [5]
0.03	0.016 59	0.000 284 (4) (3) (2)(0) (1) [5]	-0.000 287 (4) (3) (2)(0)(0) [5]
0.035	0.019 35	0.000 329 (4) (3) (2)(0) (1) [6]	-0.000 331 (5) (4) (2)(0)(0) [6]
0.04	0.022 12	0.000 372 (5) (4) (2)(0) (1) [7]	-0.000 375 (5) (4) (2)(0)(0) [7]
0.045	0.024 88	0.000 415 (5) (4) (3)(0) (1) [7]	-0.000 418 (6) (4) (2)(0)(0) [8]
0.05	0.027 64	0.000 457 (6) (4) (3)(0) (1) [8]	-0.000 461 (6) (5) (3)(0)(0) [8]
0.055	0.030 41	0.000 499 (6) (5) (3)(0) (1) [8]	-0.000 503 (7) (5) (3)(0)(0) [9]
0.06	0.033 17	0.000 539 (7) (5) (3)(0) (1) [9]	-0.000 544 (7) (6) (3)(0)(0)[10]
0.065	0.035 9	0.000 579 (7) (5) (3)(0) (2)[10]	-0.000 584 (8) (6) (3)(0)(0)[10]
0.07	0.038 7	0.000 619 (7) (6) (4)(0) (2)[10]	-0.000 624 (8) (6) (4)(0)(0)[11]
0.075	0.041 5	0.000 657 (8) (6) (4)(0) (2)[11]	-0.000 663 (8) (6) (4)(0)(0)[11]
0.08	0.044 2	0.000 695 (8) (6) (4)(0) (2)[11]	-0.000 701 (9) (7) (4)(0)(0)[12]
0.085	0.047 0	0.000 733 (8) (6) (4)(0) (2)[11]	-0.000 739 (9) (7) (4)(0)(0)[12]
0.09	0.049 8	0.000 770 (9) (7) (4)(0) (2)[12]	-0.000 776 (9) (7) (5)(0)(0)[13]
0.095	0.052 5	0.000 806 (9) (7) (4)(0) (2)[12]	-0.000 813 (10) (8) (5)(0)(0)[13]
0.1	0.055 3	0.000 842 (9) (7) (4)(0) (2)[13]	-0.000 849 (10) (8) (5)(0)(1)[14]
0.12	0.066 3	0.000 979 (10) (8) (5)(0) (3)[14]	-0.000 987 (11) (9) (6)(0)(1)[15]
0.14	0.077 4	0.001 109 (11) (8) (6)(1) (3)[15]	-0.001 118 (12) (9) (7)(1)(1)[17]
0.16	0.088 5	0.001 232 (12) (9) (6)(1) (4)[16]	-0.001 243 (13)(10) (8)(1)(1)[18]
0.18	0.099 5	0.001 348 (12) (9) (6)(1) (4)[17]	-0.001 360 (13)(10) (9)(1)(1)[19]
0.2	0.110 6	0.001 459 (13) (9) (7)(1) (4)[18]	-0.001 472 (14)(10) (9)(1)(1)[20]
0.22	0.121 6	0.001 565 (13) (9) (8)(1) (5)[19]	-0.001 579 (15)(10)(10)(1)(2)[21]
0.24	0.132 7	0.001 666 (14)(10) (8)(1) (5)[19]	-0.001 681 (15)(11)(11)(1)(2)[22]
0.26	0.143 7	0.001 762 (14)(10) (9)(1) (5)[20]	-0.001 779 (15)(11)(12)(1)(2)[22]
0.28	0.154 8	0.001 855 (14)(10) (9)(1) (6)[20]	-0.001 873 (16)(11)(13)(1)(2)[23]
0.3	0.165 9	0.001 943 (14)(10)(10)(1) (6)[21]	-0.001 963 (16)(11)(14)(1)(2)[24]
0.32	0.176 9	0.002 029 (15)(10)(10)(1) (6)[21]	-0.002 050 (16)(11)(15)(1)(2)[24]
0.34	0.188 0	0.002 111 (15)(10)(11)(1) (7)[22]	-0.002 134 (16)(11)(15)(1)(3)[25]
0.36	0.199 0	0.002 191 (15)(10)(11)(1) (7)[22]	-0.002 214 (16)(11)(16)(1)(3)[26]
0.38	0.210 1	0.002 268 (15)(10)(12)(1) (7)[23]	-0.002 293 (17)(11)(17)(1)(3)[26]
0.4	0.221 2	0.002 342 (15)(10)(12)(1) (7)[23]	-0.002 368 (17)(11)(18)(2)(3)[27]
0.42	0.232 2	0.002 413 (16)(10)(13)(2) (8)[23]	-0.002 441 (17)(11)(18)(2)(3)[27]
0.44	0.243 3	0.002 483 (16)(10)(13)(2) (8)[24]	-0.002 512 (17)(11)(19)(2)(3)[28]
0.46	0.254 3	0.002 550 (16)(10)(13)(2) (8)[24]	-0.002 581 (17)(10)(20)(2)(3)[28]
0.48	0.265 4	0.002 616 (16)(10)(14)(2) (8)[25]	-0.002 648 (17)(10)(20)(2)(4)[29]
0.5	0.276 4	0.002 680 (16)(10)(14)(2) (8)[25]	-0.002 713 (17)(10)(21)(2)(4)[29]

continued

Table 13: (continued)

Q^2 [GeV ²]	$t_0 Q^2$	$\Delta\alpha_{\text{had}}$	$\Delta_{\text{had}} \sin^2 \theta_W$
0.55	0.304 1	0.002 831 (16) (9)(15)(2) (9)[26]	-0.002 867 (18)(10)(22)(2)(4)[30]
0.6	0.331 7	0.002 973 (16) (9)(16)(2) (9)[27]	-0.003 012 (18)(10)(23)(2)(4)[31]
0.65	0.359	0.003 106 (16) (9)(17)(2)(10)[27]	-0.003 149 (18)(10)(25)(3)(5)[32]
0.7	0.387	0.003 232 (17) (9)(18)(3)(10)[28]	-0.003 277 (18)(10)(26)(3)(5)[33]
0.75	0.415	0.003 351 (17) (9)(19)(3)(10)[29]	-0.003 399 (18)(10)(27)(3)(5)[34]
0.8	0.442	0.003 463 (17) (9)(20)(3)(11)[29]	-0.003 515 (18) (9)(28)(3)(5)[35]
0.85	0.470	0.003 571 (17) (9)(20)(3)(11)[30]	-0.003 62 (2) (1) (3)(0)(1) [4]
0.9	0.498	0.003 673 (17) (8)(21)(3)(11)[31]	-0.003 73 (2) (1) (3)(0)(1) [4]
0.95	0.525	0.003 771 (17) (8)(22)(3)(12)[31]	-0.003 83 (2) (1) (3)(0)(1) [4]
1.0	0.553	0.003 864 (17) (8)(22)(4)(12)[32]	-0.003 93 (2) (1) (3)(0)(1) [4]
1.05	0.581	0.003 954 (17) (8)(23)(4)(12)[32]	-0.004 02 (2) (1) (3)(0)(1) [4]
1.1	0.608	0.004 041 (17) (8)(24)(4)(12)[33]	-0.004 11 (2) (1) (3)(0)(1) [4]
1.15	0.636	0.004 124 (17) (8)(24)(4)(12)[33]	-0.004 19 (2) (1) (3)(0)(1) [4]
1.2	0.663	0.004 204 (17) (7)(25)(4)(13)[34]	-0.004 27 (2) (1) (3)(0)(1) [4]
1.25	0.691	0.004 282 (17) (7)(25)(4)(13)[34]	-0.004 35 (2) (1) (3)(0)(1) [4]
1.3	0.719	0.004 356 (17) (7)(26)(5)(13)[35]	-0.004 43 (2) (1) (4)(0)(1) [4]
1.35	0.746	0.004 429 (18) (7)(26)(5)(13)[35]	-0.004 50 (2) (1) (4)(1)(1) [4]
1.4	0.774	0.004 50 (2) (1) (3)(0) (1) [4]	-0.004 58 (2) (1) (4)(1)(1) [4]
1.45	0.802	0.004 57 (2) (1) (3)(1) (1) [4]	-0.004 65 (2) (1) (4)(1)(1) [4]
1.5	0.829	0.004 63 (2) (1) (3)(1) (1) [4]	-0.004 71 (2) (1) (4)(1)(1) [4]
1.55	0.857	0.004 70 (2) (1) (3)(1) (1) [4]	-0.004 78 (2) (1) (4)(1)(1) [4]
1.6	0.885	0.004 76 (2) (1) (3)(1) (1) [4]	-0.004 84 (2) (1) (4)(1)(1) [5]
1.65	0.912	0.004 82 (2) (1) (3)(1) (1) [4]	-0.004 90 (2) (1) (4)(1)(1) [5]
1.7	0.940	0.004 88 (2) (1) (3)(1) (1) [4]	-0.004 96 (2) (1) (4)(1)(1) [5]
1.75	0.968	0.004 94 (2) (1) (3)(1) (1) [4]	-0.005 02 (2) (1) (4)(1)(1) [5]
1.8	0.995	0.004 99 (2) (1) (3)(1) (1) [4]	-0.005 08 (2) (1) (4)(1)(1) [5]
1.85	1.023	0.005 05 (2) (1) (3)(1) (1) [4]	-0.005 14 (2) (1) (4)(1)(1) [5]
1.9	1.050	0.005 10 (2) (0) (3)(1) (1) [4]	-0.005 19 (2) (1) (4)(1)(1) [5]
1.95	1.078	0.005 16 (2) (0) (3)(1) (1) [4]	-0.005 25 (3) (1) (4)(1)(1) [5]
2.0	1.106	0.005 21 (2) (0) (3)(1) (2) [4]	-0.005 30 (3) (0) (4)(1)(1) [5]
2.1	1.161	0.005 31 (3) (0) (3)(1) (2) [5]	-0.005 40 (3) (0) (4)(1)(1) [5]
2.2	1.216	0.005 40 (3) (0) (3)(1) (2) [5]	-0.005 49 (3) (0) (5)(1)(1) [6]
2.3	1.272	0.005 49 (3) (0) (3)(1) (2) [5]	-0.005 59 (3) (0) (5)(1)(1) [6]
2.4	1.327	0.005 58 (3) (0) (4)(1) (2) [5]	-0.005 68 (4) (0) (5)(1)(1) [6]
2.5	1.382	0.005 67 (4) (0) (4)(1) (2) [6]	-0.005 76 (4) (0) (5)(1)(1) [7]
2.6	1.437	0.005 75 (4) (0) (4)(1) (2) [6]	-0.005 84 (5) (0) (5)(1)(1) [7]
2.7	1.493	0.005 83 (5) (0) (4)(1) (2) [6]	-0.005 92 (5) (0) (5)(1)(1) [7]
2.8	1.548	0.005 90 (5) (0) (4)(1) (2) [7]	-0.006 00 (5) (0) (5)(1)(1) [8]
2.9	1.603	0.005 98 (5) (0) (4)(1) (2) [7]	-0.006 07 (6) (0) (5)(1)(1) [8]
3.0	1.659	0.006 05 (6) (0) (4)(1) (2) [7]	-0.006 14 (6) (0) (5)(1)(1) [8]
3.1	1.714	0.006 12 (6) (0) (4)(1) (2) [7]	-0.006 21 (6) (0) (5)(1)(1) [8]
3.2	1.769	0.006 18 (6) (0) (4)(1) (2) [8]	-0.006 28 (7) (0) (5)(1)(1) [9]
3.3	1.825	0.006 25 (6) (0) (4)(1) (2) [8]	-0.006 35 (7) (0) (5)(1)(1) [9]
3.4	1.880	0.006 31 (6) (0) (4)(1) (2) [8]	-0.006 41 (7) (0) (5)(1)(1) [9]

continued

Table 13: (continued)

Q^2 [GeV ²]	$t_0 Q^2$		$\Delta\alpha_{\text{had}}$		$\Delta_{\text{had}} \sin^2 \theta_W$
3.5	1.935	0.006 37	(7) (0) (4)(1) (2) [8]	−0.006 47	(7) (0) (5)(1)(1) [9]
3.6	1.990	0.006 44	(7) (0) (4)(1) (2) [8]	−0.006 53	(7) (0) (6)(1)(1) [9]
3.7	2.046	0.006 49	(7) (0) (4)(1) (2) [8]	−0.006 59	(8) (0) (6)(1)(1)[10]
3.8	2.101	0.006 55	(7) (0) (4)(1) (2) [9]	−0.006 65	(8) (0) (6)(1)(1)[10]
3.9	2.156	0.006 61	(7) (0) (4)(1) (2) [9]	−0.006 70	(8) (0) (6)(1)(1)[10]
4.0	2.212	0.006 66	(7) (0) (4)(1) (2) [9]	−0.006 76	(8) (0) (6)(1)(1)[10]
4.1	2.267	0.006 72	(7) (0) (4)(1) (2) [9]	−0.006 81	(8) (0) (6)(1)(1)[10]
4.2	2.322	0.006 77	(7) (0) (4)(1) (2) [9]	−0.006 86	(8) (0) (6)(2)(1)[10]
4.3	2.377	0.006 82	(7) (0) (4)(1) (2) [9]	−0.006 91	(8) (0) (6)(2)(1)[10]
4.4	2.433	0.006 87	(7) (0) (4)(1) (2) [9]	−0.006 96	(8) (0) (6)(2)(1)[10]
4.5	2.488	0.006 92	(8) (0) (4)(2) (2) [9]	−0.007 01	(8) (0) (6)(2)(1)[10]
4.6	2.543	0.006 97	(8) (0) (4)(2) (2) [9]	−0.007 06	(8) (0) (6)(2)(1)[10]
4.7	2.599	0.007 02	(8) (0) (4)(2) (2) [9]	−0.007 10	(8) (0) (6)(2)(1)[10]
4.8	2.654	0.007 06	(8) (0) (5)(2) (2) [9]	−0.007 15	(8) (0) (6)(2)(1)[10]
4.9	2.709	0.007 11	(8) (0) (4)(2) (2) [9]	−0.007 19	(8) (0) (6)(2)(1)[10]
5.0	2.764	0.007 16	(8) (0) (5)(2) (2) [9]	−0.007 24	(8) (0) (6)(2)(1)[10]
5.2	2.875	0.007 24	(8) (0) (4)(2) (2) [9]	−0.007 32	(8) (0) (6)(2)(1)[10]
5.4	2.986	0.007 33	(8) (0) (4)(2) (2) [9]	−0.007 41	(8) (0) (6)(2)(1)[10]
5.6	3.096	0.007 41	(8) (0) (5)(2) (2) [9]	−0.007 49	(8) (0) (6)(2)(1)[11]
5.8	3.207	0.007 49	(8) (0) (4)(2) (2) [9]	−0.007 57	(8) (0) (6)(2)(1)[11]
6.0	3.317	0.007 57	(8) (0) (5)(2) (2) [9]	−0.007 64	(8) (0) (6)(2)(1)[11]
6.2	3.428	0.007 65	(8) (0) (4)(2) (2) [9]	−0.007 71	(8) (0) (6)(2)(1)[11]
6.4	3.538	0.007 72	(8) (0) (5)(2) (2) [9]	−0.007 78	(8) (0) (6)(2)(1)[11]
6.6	3.65	0.007 79	(8) (0) (5)(2) (2) [9]	−0.007 85	(8) (0) (6)(2)(1)[11]
6.8	3.76	0.007 86	(8) (0) (4)(2) (2) [9]	−0.007 92	(8) (0) (6)(2)(1)[11]
7.0	3.87	0.007 93	(8) (0) (4)(2) (2) [9]	−0.007 99	(8) (0) (6)(2)(1)[11]

References

- [1] S. Aoki et al. (Flavour Lattice Averaging Group), “FLAG review 2019”, *Eur. Phys. J. C* **80**, 113 (2020), [arXiv:1902.08191 \[hep-lat\]](#).
- [2] Y. Aoki et al. (Flavour Lattice Averaging Group), “FLAG review 2021”, (2021), [arXiv:2111.09849 \[hep-lat\]](#).
- [3] B. Abi et al., “Measurement of the positive muon anomalous magnetic moment to 0.46 ppm”, *Phys. Rev. Lett.* **126**, 141801 (2021), [arXiv:2104.03281 \[hep-ex\]](#).
- [4] G. W. Bennett et al. (Muon $g - 2$ Collaboration), “Final report of the E821 muon anomalous magnetic moment measurement at BNL”, *Phys. Rev. D* **73**, 072003 (2006), [arXiv:hep-ex/0602035 \[hep-ex\]](#).
- [5] T. Aoyama et al., “The anomalous magnetic moment of the muon in the Standard Model”, *Phys. Rep.* **887**, 1–166 (2020), [arXiv:2006.04822 \[hep-ph\]](#).

- [6] Sz. Borsányi et al. (Budapest-Marseille-Wuppertal Collaboration), “Leading hadronic contribution to the muon magnetic moment from lattice QCD”, *Nature* **593**, 51–55 (2021), [arXiv:2002.12347 \[hep-lat\]](#).
- [7] P. A. Zyla et al. (Particle Data Group), “Review of particle physics”, *PTEP* **2020**, 083C01 (2020).
- [8] A. Gérardin et al., “Leading hadronic contribution to $(g - 2)_\mu$ from lattice QCD with $N_f = 2 + 1$ flavors of $O(a)$ improved Wilson quarks”, *Phys. Rev. D* **100**, 014510 (2019), [arXiv:1904.03120 \[hep-lat\]](#).
- [9] S. Eidelman, F. Jegerlehner, A. L. Kataev, and O. Veretin, “Testing non-perturbative strong interaction effects via the Adler function”, *Phys. Lett. B* **454**, 369–380 (1999), [arXiv:hep-ph/9812521 \[hep-ph\]](#).
- [10] F. Jegerlehner, “The running fine structure constant $\alpha(E)$ via the Adler function”, *Nucl. Phys. B Proc. Suppl.* **181-182**, edited by C. Bini and G. Venanzoni, 135–140 (2008), [arXiv:0807.4206 \[hep-ph\]](#).
- [11] A. Keshavarzi, D. Nomura, and T. Teubner, “ $g - 2$ of charged leptons, $\alpha(M_Z^2)$, and the hyperfine splitting of muonium”, *Phys. Rev. D* **101**, 014029 (2020), [arXiv:1911.00367 \[hep-ph\]](#).
- [12] M. Davier, A. Hoecker, B. Malaescu, and Z. Zhang, “A new evaluation of the hadronic vacuum polarisation contributions to the muon anomalous magnetic moment and to $\alpha(m_Z^2)$ ”, *Eur. Phys. J. C* **80**, 241 (2020), [arXiv:1908.00921 \[hep-ph\]](#), [Erratum: *Eur. Phys. J. C* **80**, 410 (2020)].
- [13] F. Jegerlehner, “ $\alpha_{\text{QED,eff}}(s)$ for precision physics at the FCC-ee/ILC”, in, *CERN Yellow Reports: Monographs* **3**, edited by A. Blondel, J. Gluza, S. Jadach, P. Janot, and T. Riemann, 9–37 (2020).
- [14] L. Morel, Z. Yao, P. Cladé, and S. Guellati-Khélifa, “Determination of the fine-structure constant with an accuracy of 81 parts per trillion”, *Nature* **588**, 61–65 (2020).
- [15] G. Colangelo, M. Hoferichter, and P. Stoffer, “Two-pion contribution to hadronic vacuum polarization”, *JHEP* **1902**, 006 (2019), [arXiv:1810.00007 \[hep-ph\]](#).
- [16] S. L. Adler, “Some simple vacuum-polarization phenomenology: $e^+e^- \rightarrow$ hadrons; the muonic-atom x-ray discrepancy and $g_\mu - 2$ ”, *Phys. Rev. D* **10**, 3714 (1974).
- [17] F. Jegerlehner, “Hadronic effects in $(g - 2)_\mu$ and $\alpha_{\text{QED}}(M_Z)$: status and perspectives”, in *4th International Symposium on Radiative Corrections: Applications of Quantum Field Theory to Phenomenology* (1999), pp. 75–89, [arXiv:hep-ph/9901386 \[hep-ph\]](#).
- [18] F. Jegerlehner, “Hadronic vacuum polarization effects in $\alpha_{\text{em}}(M_Z)$ ”, in *Mini-Workshop on Electroweak Precision Data and the Higgs Mass* (), pp. 97–112, [arXiv:hep-ph/0308117 \[hep-ph\]](#).
- [19] F. Burger, K. Jansen, M. Petschlies, and G. Pientka, “Leading hadronic contributions to the running of the electroweak coupling constants from lattice QCD”, *JHEP* **1511**, 215 (2015), [arXiv:1505.03283 \[hep-lat\]](#).
- [20] A. Francis et al., “Study of the hadronic contributions to the running of the QED coupling and the weak mixing angle”, *PoS LATTICE2015*, 110 (2015), [arXiv:1511.04751 \[hep-lat\]](#).
- [21] Sz. Borsányi et al. (Budapest-Marseille-Wuppertal Collaboration), “Hadronic vacuum polarization contribution to the anomalous magnetic moments of leptons from first principles”, *Phys. Rev. Lett.* **121**, 022002 (2018), [arXiv:1711.04980 \[hep-lat\]](#).

- [22] H. B. Meyer and H. Wittig, “Lattice QCD and the anomalous magnetic moment of the muon”, *Prog. Part. Nucl. Phys.* **104**, 46–96 (2019), arXiv:1807.09370 [hep-lat].
- [23] B. Chakraborty et al. (Fermilab Lattice, HPQCD, and MILC Collaborations), “Strong-isospin-breaking correction to the muon anomalous magnetic moment from lattice qcd at the physical point”, *Phys. Rev. Lett.* **120**, 152001 (2018), arXiv:1710.11212 [hep-lat].
- [24] T. Blum et al. (RBC and UKQCD Collaborations), “Calculation of the hadronic vacuum polarization contribution to the muon anomalous magnetic moment”, *Phys. Rev. Lett.* **121**, 022003 (2018), arXiv:1801.07224 [hep-lat].
- [25] D. Giusti, V. Lubicz, G. Martinelli, F. Sanfilippo, and S. Simula (for ETM Collaboration), “Electromagnetic and strong isospin-breaking corrections to the muon $g - 2$ from Lattice QCD+QED”, *Phys. Rev. D* **99**, 114502 (2019), arXiv:1901.10462 [hep-lat].
- [26] E. Shintani and Y. Kuramashi (PACS Collaboration), “Hadronic vacuum polarization contribution to the muon $g - 2$ with 2+1 flavor lattice QCD on a larger than $(10 \text{ fm})^4$ lattice at the physical point”, *Phys. Rev. D* **100**, 034517 (2019), arXiv:1902.00885 [hep-lat].
- [27] C. T. H. Davies et al. (Fermilab Lattice, HPQCD, and MILC Collaborations), “Hadronic-vacuum-polarization contribution to the muon’s anomalous magnetic moment from four-flavor lattice QCD”, *Phys. Rev. D* **101**, 034512 (2020), arXiv:1902.04223 [hep-lat].
- [28] C. Aubin et al., “Light quark vacuum polarization at the physical point and contribution to the muon $g - 2$ ”, *Phys. Rev. D* **101**, 014503 (2020), arXiv:1905.09307 [hep-lat].
- [29] D. Giusti and S. Simula, “Lepton anomalous magnetic moments in Lattice QCD+QED”, *PoS LATTICE2019*, 104 (2019), arXiv:1910.03874 [hep-lat].
- [30] M. Davier, A. Hoecker, B. Malaescu, and Z. Zhang, “Reevaluation of the hadronic vacuum polarisation contributions to the Standard Model predictions of the muon $g - 2$ and $\alpha(m_Z^2)$ using newest hadronic cross-section data”, *Eur. Phys. J. C* **77**, 827 (2017), arXiv:1706.09436 [hep-ph].
- [31] A. Keshavarzi, D. Nomura, and T. Teubner, “Muon $g - 2$ and $\alpha(M_Z^2)$: a new data-based analysis”, *Phys. Rev. D* **97**, 114025 (2018), arXiv:1802.02995 [hep-ph].
- [32] M. Hoferichter, B.-L. Hoid, and B. Kubis, “Three-pion contribution to hadronic vacuum polarization”, *JHEP* **1908**, 137 (2019), arXiv:1907.01556 [hep-ph].
- [33] M. Passera, W. J. Marciano, and A. Sirlin, “The muon $g - 2$ and the bounds on the Higgs boson mass”, *Phys. Rev. D* **78**, 013009 (2008), arXiv:0804.1142 [hep-ph].
- [34] A. Crivellin, M. Hoferichter, C. A. Manzari, and M. Montull, “Hadronic vacuum polarization: $(g - 2)_\mu$ versus global electroweak fits”, *Phys. Rev. Lett.* **125**, 091801 (2020), arXiv:2003.04886 [hep-ph].
- [35] A. Keshavarzi, W. J. Marciano, M. Passera, and A. Sirlin, “Muon $g - 2$ and $\Delta\alpha$ connection”, *Phys. Rev. D* **102**, 033002 (2020), arXiv:2006.12666 [hep-ph].
- [36] B. Malaescu and M. Schott, “Impact of correlations between a_μ and α_{QED} on the EW fit”, *Eur. Phys. J. C* **81**, 46 (2021), arXiv:2008.08107 [hep-ph].
- [37] G. Colangelo, M. Hoferichter, and P. Stoffer, “Constraints on the two-pion contribution to hadronic vacuum polarization”, *Phys. Lett. B* **814**, 136073 (2021), arXiv:2010.07943 [hep-ph].
- [38] S. L. Glashow, “Partial-symmetries of weak interactions”, *Nucl. Phys.* **22**, 579–588 (1961).
- [39] S. Sarantakos, A. Sirlin, and W. J. Marciano, “Radiative corrections to neutrino-lepton scattering in the $SU(2)_L \otimes U(1)$ theory”, *Nucl. Phys. B* **217**, 84–116 (1983).

- [40] A. Czarnecki and W. J. Marciano, “Electroweak radiative corrections to polarized Møller scattering asymmetries”, *Phys. Rev. D* **53**, 1066–1072 (1996), arXiv:hep-ph/9507420 [hep-ph].
- [41] A. Czarnecki and W. J. Marciano, “Parity violating asymmetries at future lepton colliders”, *Int. J. Mod. Phys. A* **13**, edited by C. A. Heusch, 2235–2244 (1998), arXiv:hep-ph/9801394 [hep-ph].
- [42] A. Czarnecki and W. J. Marciano, “Polarized Møller scattering asymmetries”, *Int. J. Mod. Phys. A* **15**, edited by C. A. Heusch, 2365–2376 (2000), arXiv:hep-ph/0003049 [hep-ph].
- [43] A. Ferroglia, G. Ossola, and A. Sirlin, “The electroweak form factor $\hat{\kappa}(q^2)$ and the running of $\sin^2 \hat{\theta}_W$ ”, *Eur. Phys. J. C* **34**, 165–171 (2004), arXiv:hep-ph/0307200 [hep-ph].
- [44] K. S. Kumar, S. Mantry, W. J. Marciano, and P. A. Souder, “Low energy measurements of the weak mixing angle”, *Ann. Rev. Nucl. Part. Sci.* **63**, 237–267 (2013), arXiv:1302.6263 [hep-ex].
- [45] J. Erler and M. J. Ramsey-Musolf, “Weak mixing angle at low energies”, *Phys. Rev. D* **72**, 073003 (2005), arXiv:hep-ph/0409169 [hep-ph].
- [46] J. Erler and R. Ferro-Hernández, “Weak mixing angle in the Thomson limit”, *JHEP* **1803**, 196 (2018), arXiv:1712.09146 [hep-ph].
- [47] P. L. Anthony et al. (SLAC E158 Collaboration), “Precision measurement of the weak mixing angle in Møller scattering”, *Phys. Rev. Lett.* **95**, 081601 (2005), arXiv:hep-ex/0504049 [hep-ex].
- [48] D. Androic et al. (Q_{weak} Collaboration), “First determination of the weak charge of the proton”, *Phys. Rev. Lett.* **111**, 141803 (2013), arXiv:1307.5275 [nucl-ex].
- [49] D. Wang et al. (The Jefferson Lab PVDIS Collaboration), “Measurement of parity violation in electron–quark scattering”, *Nature* **506**, 67–70 (2014).
- [50] D. Androić et al. (The Jefferson Lab Q_{weak} Collaboration), “Precision measurement of the weak charge of the proton”, *Nature* **557**, 207–211 (2018), arXiv:1905.08283 [nucl-ex].
- [51] D. Becker et al., “The P2 experiment”, *Eur. Phys. J. A* **54**, 208 (2018), arXiv:1802.04759 [nucl-ex].
- [52] J. Benesch et al. (The MOLLER Collaboration), “The MOLLER experiment: an ultra-precise measurement of the weak mixing angle using Møller scattering”, (2014), arXiv:1411.4088 [nucl-ex].
- [53] J. P. Chen, H. Gao, T. K. Hemmick, Z.-E. Meziani, and P. A. Souder (The SoLID collaboration), “A white paper on SoLID (solenoidal large intensity device)”, arXiv:1409.7741 [nucl-ex].
- [54] P. A. Souder, “Parity violation in deep inelastic scattering with the SoLID spectrometer at JLab”, *Int. J. Mod. Phys. Conf. Ser.* **40**, edited by H. Gao and B.-Q. Ma, 1660077 (2016).
- [55] F. Jegerlehner, “Hadronic contributions to electroweak parameter shifts”, *Z. Phys. C Part. Fields* **32**, 195 (1986).
- [56] F. Jegerlehner, “Electroweak effective couplings for future precision experiments”, *Nuovo Cim. C* **034S1**, 31–40 (2011), arXiv:1107.4683 [hep-ph].
- [57] F. Jegerlehner, “Variations on photon vacuum polarization”, (2017), arXiv:1711.06089 [hep-ph].
- [58] F. Jegerlehner, “Vector boson parameters: scheme dependence and theoretical uncertainties”, *Z. Phys. C* **32**, 425–436 (1986), [Erratum: *Z. Phys. C* **38**, 519 (1988)].

- [59] V. Gülpers, H. Meyer, G. von Hippel, and H. Wittig, “The leading hadronic contribution to γ - Z mixing”, *PoS LATTICE2015*, 263 (2016).
- [60] M. Cè, A. Gérardin, K. Ottnad, and H. B. Meyer, “The leading hadronic contribution to the running of the weinberg angle using covariant coordinate-space methods”, *PoS LATTICE2018*, 137 (2018), [arXiv:1811.08669 \[hep-lat\]](#).
- [61] D. Bernecker and H. B. Meyer, “Vector correlators in lattice QCD: methods and applications”, *Eur. Phys. J. A* **47**, 148 (2011), [arXiv:1107.4388 \[hep-lat\]](#).
- [62] A. Francis, B. Jaeger, H. B. Meyer, and H. Wittig, “New representation of the Adler function for lattice QCD”, *Phys. Rev. D* **88**, 054502 (2013), [arXiv:1306.2532 \[hep-lat\]](#).
- [63] M. Della Morte et al., “The hadronic vacuum polarization contribution to the muon $g - 2$ from lattice QCD”, *JHEP* **1710**, 020 (2017), [arXiv:1705.01775 \[hep-lat\]](#).
- [64] T. Bhattacharya, R. Gupta, W. Lee, S. R. Sharpe, and J. M. S. Wu, “Improved bilinears in lattice QCD with nondegenerate quarks”, *Phys. Rev. D* **73**, 034504 (2006), [arXiv:hep-lat/0511014 \[hep-lat\]](#).
- [65] A. Gérardin, T. Harris, and H. B. Meyer, “Non-perturbative renormalization and $O(a)$ -improvement of the non-singlet vector current with $N_f = 2+1$ Wilson fermions and tree-level Symanzik improved gauge action”, *Phys. Rev. D* **99**, 014519 (2018), [arXiv:1811.08209 \[hep-lat\]](#).
- [66] M. Bruno, T. Korzec, and S. Schaefer, “Setting the scale for the CLS 2+1 flavor ensembles”, *Phys. Rev. D* **95**, 074504 (2017), [arXiv:1608.08900 \[hep-lat\]](#).
- [67] M. Bruno et al., “Simulation of QCD with $N_f = 2 + 1$ flavors of non-perturbatively improved Wilson fermions”, *JHEP* **1502**, 043 (2015), [arXiv:1411.3982 \[hep-lat\]](#).
- [68] J. Bulava and S. Schaefer, “Improvement of $N_f = 3$ lattice QCD with Wilson fermions and tree-level improved gauge action”, *Nucl. Phys. B* **874**, 188–197 (2013), [arXiv:1304.7093 \[hep-lat\]](#).
- [69] M. Lüscher and S. Schaefer, “Lattice QCD without topology barriers”, *JHEP* **1107**, 036 (2011), [arXiv:1105.4749 \[hep-lat\]](#).
- [70] M. Lüscher, “Properties and uses of the Wilson flow in lattice QCD”, *JHEP* **1008**, 071 (2010), [arXiv:1006.4518 \[hep-lat\]](#), [Erratum: *JHEP* **1403** 092 (2014)].
- [71] D. Mohler and S. Schaefer, “Remarks on strange-quark simulations with Wilson fermions”, *Phys. Rev. D* **102**, 074506 (2020), [arXiv:2003.13359 \[hep-lat\]](#).
- [72] L. Giusti, T. Harris, A. Nada, and S. Schaefer, “Frequency-splitting estimators of single-propagator traces”, *Eur. Phys. J. C* **79**, 586 (2019), [arXiv:1903.10447 \[hep-lat\]](#).
- [73] C. McNeile and C. Michael (UKQCD Collaboration), “Decay width of light quark hybrid meson from the lattice”, *Phys. Rev. D* **73**, 074506 (2006), [arXiv:hep-lat/0603007 \[hep-lat\]](#).
- [74] K. Jansen, C. Michael, and C. Urbach (European Twisted Mass Collaboration), “The η' meson from lattice QCD”, *Eur. Phys. J. C* **58**, 261–269 (2008), [arXiv:0804.3871 \[hep-lat\]](#).
- [75] Ph. Boucaud et al. (ETM Collaboration), “Dynamical twisted mass fermions with light quarks: simulation and analysis details”, *Comput. Phys. Commun.* **179**, 695–715 (2008), [arXiv:0803.0224 \[hep-lat\]](#).
- [76] V. Gülpers, G. von Hippel, and H. Wittig, “Scalar pion form factor in two-flavor lattice QCD”, *Phys. Rev. D* **89**, 094503 (2014), [arXiv:1309.2104 \[hep-lat\]](#).

- [77] A. Stathopoulos, J. Laeuchli, and K. Orginos, “Hierarchical probing for estimating the trace of the matrix inverse on toroidal lattices”, *SIAM J. Sci. Comput.* **35**, S299–S322 (2013), [arXiv:1302.4018 \[hep-lat\]](#).
- [78] D. Djukanovic, K. Ottnad, J. Wilhelm, and H. Wittig, “Strange electromagnetic form factors of the nucleon with $N_f = 2 + 1$ $\mathcal{O}(a)$ -improved Wilson fermions”, *Phys. Rev. Lett.* **123**, 212001 (2019), [arXiv:1903.12566 \[hep-lat\]](#).
- [79] G. Parisi, “The strategy for computing the hadronic mass spectrum”, *Phys. Rep.* **103**, 203–211 (1984).
- [80] G. P. Lepage, “The analysis of algorithms for lattice field theory”, in *Boulder ASI 1989* (1989), pp. 97–120.
- [81] M. Lüscher and P. Weisz, “Locality and exponential error reduction in numerical lattice gauge theory”, *JHEP* **0109**, 010 (2001), [arXiv:hep-lat/0108014 \[hep-lat\]](#).
- [82] H. B. Meyer, “Locality and statistical error reduction on correlation functions”, *JHEP* **0301**, 048 (2003), [arXiv:hep-lat/0209145 \[hep-lat\]](#).
- [83] M. Cè, L. Giusti, and S. Schaefer, “Domain decomposition, multilevel integration, and exponential noise reduction in lattice QCD”, *Phys. Rev. D* **93**, 094507 (2016), [arXiv:1601.04587 \[hep-lat\]](#).
- [84] M. Cè, L. Giusti, and S. Schaefer, “Local factorization of the fermion determinant in lattice QCD”, *Phys. Rev. D* **95**, 034503 (2017), [arXiv:1609.02419 \[hep-lat\]](#).
- [85] M. Cè, “Locality and multi-level sampling with fermions”, *Eur. Phys. J. Plus* **134**, 299 (2019).
- [86] M. Dalla Brida, L. Giusti, T. Harris, and M. Pepe, “Multi-level Monte Carlo computation of the hadronic vacuum polarization contribution to $(g_\mu - 2)$ ”, *Phys. Lett. B* **816**, 136191 (2020), [arXiv:2007.02973 \[hep-lat\]](#).
- [87] C. Lehner, *The hadronic vacuum polarization contribution to the muon anomalous magnetic moment*, talk at RBRC Workshop on Lattice Gauge Theories, (2016) <https://indico.bnl.gov/event/1628/contributions/2819/>.
- [88] C. Andersen, J. Bulava, B. Hörz, and C. Morningstar, “The $I = 1$ pion-pion scattering amplitude and timelike pion form factor from $N_f = 2 + 1$ lattice QCD”, *Nucl. Phys. B* **939**, 145–173 (2019), [arXiv:1808.05007 \[hep-lat\]](#).
- [89] M. T. Hansen, F. Romero-López, and S. R. Sharpe, “Generalizing the relativistic quantization condition to include all three-pion isospin channels”, *JHEP* **2007**, 047 (2020), [arXiv:2003.10974 \[hep-lat\]](#).
- [90] M. Cè et al., “The hadronic contribution to the running of the electromagnetic coupling and the electroweak mixing angle”, *PoS LATTICE2019*, 010 (2020), [arXiv:1910.09525 \[hep-lat\]](#).
- [91] C. Aubin et al., “Finite-volume effects in the muon anomalous magnetic moment on the lattice”, *Phys. Rev. D* **93**, 054508 (2016), [arXiv:1512.07555 \[hep-lat\]](#).
- [92] J. Bijnens and J. Relefors, “Vector two-point functions in finite volume using partially quenched chiral perturbation theory at two loops”, *JHEP* **1712**, 114 (2017), [arXiv:1710.04479 \[hep-lat\]](#).
- [93] H. B. O’Connell, B. C. Pearce, A. W. Thomas, and A. G. Williams, “Rho-omega mixing, vector meson dominance and the pion form-factor”, *Prog. Part. Nucl. Phys.* **39**, 201–252 (1997), [arXiv:hep-ph/9501251 \[hep-ph\]](#).

- [94] F. Jegerlehner and A. Nyffeler, “The muon $g - 2$ ”, *Phys. Rept.* **477**, 1–110 (2009), [arXiv:0902.3360 \[hep-ph\]](#).
- [95] H. B. Meyer, “Lattice QCD and the Timelike Pion Form Factor”, *Phys. Rev. Lett.* **107**, 072002 (2011), [arXiv:1105.1892 \[hep-lat\]](#).
- [96] M. Lüscher, “Signatures of unstable particles in finite volume”, *Nucl. Phys. B* **364**, 237–251 (1991).
- [97] L. Lellouch and M. Lüscher, “Weak transition matrix elements from finite-volume correlation functions”, *Commun. Math. Phys.* **219**, 31–44 (2001), [arXiv:hep-lat/0003023 \[hep-lat\]](#).
- [98] G. J. Gounaris and J. J. Sakurai, “Finite-width corrections to the vector-meson-dominance prediction for $\rho \rightarrow e + e^-$ ”, *Phys. Rev. Lett.* **21**, 244–247 (1968).
- [99] F. Erben, J. R. Green, D. Mohler, and H. Wittig, “Rho resonance, timelike pion form factor, and implications for lattice studies of the hadronic vacuum polarization”, *Phys. Rev. D* **101**, 054504 (2020), [arXiv:1910.01083 \[hep-lat\]](#).
- [100] M. T. Hansen and A. Patella, “Finite-volume effects in $(g - 2)_\mu^{\text{HVP,LO}}$ ”, *Phys. Rev. Lett.* **123**, 172001 (2019), [arXiv:1904.10010 \[hep-lat\]](#).
- [101] M. T. Hansen and A. Patella, “Finite-volume and thermal effects in the leading-HVP contribution to muonic $(g - 2)$ ”, *JHEP* **2010**, 029 (2020), [arXiv:2004.03935 \[hep-lat\]](#).
- [102] D. Brömmel et al. (QCDSF/UKQCD Collaboration), “The pion form factor from lattice QCD with two dynamical flavours”, *Eur. Phys. J. C* **51**, 335–345 (2007), [arXiv:hep-lat/0608021 \[hep-lat\]](#).
- [103] L. Lellouch, *Discussion: benchmarks, In memoriam Simon Eidelman*, at the Muon $g - 2$ theory initiative workshop in memoriam Simon Eidelman, (2021) <https://agenda.hepl.phys.nagoya-u.ac.jp/indico/contributionDisplay.py?sessionId=5&contribId=25&confId=1691>.
- [104] R. Urech, “Virtual photons in chiral perturbation theory”, *Nucl. Phys. B* **433**, 234–254 (1995), [arXiv:hep-ph/9405341 \[hep-ph\]](#).
- [105] H. Neufeld and H. Rupertsberger, “The electromagnetic interaction in chiral perturbation theory”, *Z. Phys. C* **71**, 131–138 (1996), [arXiv:hep-ph/9506448 \[hep-ph\]](#).
- [106] N. Husung, P. Marquard, and R. Sommer, “Asymptotic behavior of cutoff effects in Yang–Mills theory and in Wilson’s lattice QCD”, *Eur. Phys. J. C* **80**, 200 (2020), [arXiv:1912.08498 \[hep-lat\]](#).
- [107] M. Cè, T. Harris, H. B. Meyer, A. Toniato, and Cs. Török, “Vacuum correlators at short distances from lattice QCD”, *JHEP* **2112**, 215 (2021), [arXiv:2106.15293 \[hep-lat\]](#).
- [108] S. Aoki et al. (Flavour Lattice Averaging Group), “Review of lattice results concerning low-energy particle physics”, *Eur. Phys. J. C* **77**, 112 (2017), [arXiv:1607.00299 \[hep-lat\]](#).
- [109] G. Ecker, J. Gasser, A. Pich, and E. de Rafael, “The role of resonances in chiral perturbation theory”, *Nucl. Phys. B* **321**, 311–342 (1989).
- [110] C. Aubin and T. Blum, “Calculating the hadronic vacuum polarization and leading hadronic contribution to the muon anomalous magnetic moment with improved staggered quarks”, *Phys. Rev. D* **75**, 114502 (2007), [arXiv:hep-lat/0608011 \[hep-lat\]](#).
- [111] M. Golterman, K. Maltman, and S. Peris, “Chiral extrapolation of the leading hadronic contribution to the muon anomalous magnetic moment”, *Phys. Rev. D* **95**, 074509 (2017), [arXiv:1701.08685 \[hep-lat\]](#).

- [112] G. Colangelo, M. Hoferichter, B. Kubis, M. Niehus, and J. Ruiz de Elvira, “Chiral extrapolation of hadronic vacuum polarization”, *Phys. Lett. B* **825**, 136852 (2021), arXiv:2110.05493 [hep-ph].
- [113] O. Ledoit and M. Wolf, “A well-conditioned estimator for large-dimensional covariance matrices”, *J. Multivariate Anal.* **88**, 365–411 (2004).
- [114] A. Touloumis, “Nonparametric stein-type shrinkage covariance matrix estimators in high-dimensional settings”, *Comput. Stat. Data Anal.* **83**, 251–261 (2015), arXiv:1410.4726 [stat.ME].
- [115] T. San José, “The hadronic contribution to the running of the electromagnetic coupling and the electroweak mixing angle”, PhD thesis (Johannes Gutenberg-Universität Mainz, 2022), to be published.
- [116] A. M. Ferrenberg and R. H. Swendsen, “New monte carlo technique for studying phase transitions”, *Phys. Rev. Lett.* **61**, 2635–2638 (1988), [Erratum: *Phys. Rev. Lett.* **63**, 1658 (1989)].
- [117] A. Duncan, E. Eichten, and R. Sedgewick, “Computing electromagnetic effects in fully unquenched QCD”, *Phys. Rev. D* **71**, 094509 (2005), arXiv:hep-lat/0405014 [hep-lat].
- [118] A. Hasenfratz, R. Hoffmann, and S. Schaefer, “Reweighting towards the chiral limit”, *Phys. Rev. D* **78**, 014515 (2008), arXiv:0805.2369 [hep-lat].
- [119] J. Finkenrath, F. Knechtli, and B. Leder, “One flavor mass reweighting in lattice QCD”, *Nucl. Phys. B* **877**, 441–456 (2013), arXiv:1306.3962 [hep-lat], [Erratum: *Nucl. Phys. B* **880**, 574–575 (2014)].
- [120] G. M. de Divitiis et al. (RM123 collaboration), “Isospin breaking effects due to the up-down mass difference in lattice QCD”, *JHEP* **1204**, 124 (2012), arXiv:1110.6294 [hep-lat].
- [121] G. M. de Divitiis et al. (RM123 Collaboration), “Leading isospin breaking effects on the lattice”, *Phys. Rev. D* **87**, 114505 (2013), arXiv:1303.4896 [hep-lat].
- [122] M. Hayakawa and S. Uno, “QED in finite volume and finite size scaling effect on electromagnetic properties of hadrons”, *Prog. Theor. Phys.* **120**, 413–441 (2008), arXiv:0804.2044 [hep-ph].
- [123] A. Risch and H. Wittig, “Leading isospin breaking effects in the HVP contribution to a_μ and to the running of α ”, *PoS LATTICE2021*, 106 (2021), arXiv:2112.00878 [hep-lat].
- [124] A. Risch and H. Wittig, “Leading isospin breaking effects in the hadronic vacuum polarisation with open boundaries”, *PoS LATTICE2019*, 296 (2020), arXiv:1911.04230 [hep-lat].
- [125] A. Risch and H. Wittig, “Towards leading isospin breaking effects in mesonic masses with open boundaries”, *PoS LATTICE2018*, 059 (2019), arXiv:1811.00895 [hep-lat].
- [126] A. Risch and H. Wittig, “Towards leading isospin breaking effects in mesonic masses with $O(a)$ improved wilson fermions”, *EPJ Web Conf.* **175**, edited by M. Della Morte, P. Fritzsche, E. Gámiz Sánchez, and C. Pena Ruano, 14019 (2018), arXiv:1710.06801 [hep-lat].
- [127] E. Shintani et al., “Covariant approximation averaging”, *Phys. Rev. D* **91**, 114511 (2015), arXiv:1402.0244 [hep-lat].
- [128] G. S. Bali, S. Collins, and A. Schäfer, “Effective noise reduction techniques for disconnected loops in lattice QCD”, *Comput. Phys. Commun.* **181**, 1570–1583 (2010), arXiv:0910.3970 [hep-lat].

- [129] A. Risch, “Isospin breaking effects in hadronic matrix elements on the lattice”, PhD thesis (Johannes Gutenberg-Universität Mainz, 2021), [10.25358/openscience-6314](https://nbn-resolving.org/urn:nbn:de:hbz:5:1-6314).
- [130] C. Aubin, T. Blum, M. Golterman, and S. Peris, “Model-independent parametrization of the hadronic vacuum polarization and $g - 2$ for the muon on the lattice”, *Phys. Rev. D* **86**, 054509 (2012), [arXiv:1205.3695 \[hep-lat\]](https://arxiv.org/abs/1205.3695).
- [131] G. A. Baker, “Best error bounds for Padé approximants to convergent series of Stieltjes”, *J. Math. Phys.* **10**, 814–820 (1969).
- [132] M. Barnsley, “The bounding properties of the multipoint Padé approximant to a series of Stieltjes on the real line”, *J. Math. Phys.* **14**, 299–313 (1973).
- [133] W. H. Press, S. A. Teukolsky, W. T. Vetterling, and B. P. Flannery, *Numerical recipes, The art of scientific computing*, Third Edition (Cambridge University Press, 2007), 1256 pp.
- [134] F. Jegerlehner, *alphaQEDc19*, (2019) <http://www-com.physik.hu-berlin.de/~fjeger/software.html>.
- [135] B. Colquhoun, R. J. Dowdall, C. T. H. Davies, K. Hornbostel, and G. P. Lepage (HPQCD Collaboration), “ Υ and Υ' leptonic widths, a_μ^b , and m_b from full lattice QCD”, *Phys. Rev. D* **91**, 074514 (2015), [arXiv:1408.5768 \[hep-lat\]](https://arxiv.org/abs/1408.5768).
- [136] B. Chakraborty et al. (HPQCD Collaboration), “The hadronic vacuum polarization contribution to a_μ from full lattice QCD”, *Phys. Rev. D* **96**, 034516 (2017), [arXiv:1601.03071 \[hep-lat\]](https://arxiv.org/abs/1601.03071).
- [137] M. Davier, A. Hoecker, B. Malaescu, and Z. Zhang, *Space-like $\Delta\alpha_{\text{had}}^{(5)}(-Q^2)$ data*, private communication.
- [138] A. Keshavarzi, D. Nomura, and T. Teubner, *Space-like $\Delta\alpha_{\text{had}}^{(5)}(-Q^2)$ data, including correlation*, private communication.
- [139] M. Baak et al. (The Gfitter Group), “The global electroweak fit at NNLO and prospects for the LHC and ILC”, *Eur. Phys. J. C* **74**, 3046 (2014), [arXiv:1407.3792 \[hep-ph\]](https://arxiv.org/abs/1407.3792).
- [140] K. G. Chetyrkin, J. H. Kühn, and M. Steinhauser, “Three-loop polarization function and $O(\alpha_s^2)$ corrections to the production of heavy quarks”, *Nucl. Phys. B* **482**, 213–240 (1996), [arXiv:hep-ph/9606230 \[hep-ph\]](https://arxiv.org/abs/hep-ph/9606230).
- [141] F. Jegerlehner, *pQCDAdler*, (2012) <http://www-com.physik.hu-berlin.de/~fjeger/software.html>.
- [142] J. Haller et al. (The Gfitter Group), “Update of the global electroweak fit and constraints on two-Higgs-doublet models”, *Eur. Phys. J. C* **78**, 675 (2018), [arXiv:1803.01853 \[hep-ph\]](https://arxiv.org/abs/1803.01853).
- [143] J. de Blas et al., “Global analysis of electroweak data in the standard model”, (2021), [arXiv:2112.07274 \[hep-ph\]](https://arxiv.org/abs/2112.07274).
- [144] J. de Blas et al., “Hepfit: a code for the combination of indirect and direct constraints on high energy physics models”, *Eur. Phys. J. C* **80**, 456 (2020), [arXiv:1910.14012 \[hep-ph\]](https://arxiv.org/abs/1910.14012).
- [145] S. Schael et al. (ALEPH, DELPHI, L3, OPAL, SLD, LEP Electroweak Working Group, SLD Electroweak Group, SLD Heavy Flavour Group), “Precision electroweak measurements on the Z resonance”, *Phys. Rept.* **427**, 257–454 (2006), [arXiv:hep-ex/0509008 \[hep-ex\]](https://arxiv.org/abs/hep-ex/0509008).
- [146] A. Francis, G. von Hippel, H. B. Meyer, and F. Jegerlehner, “Vector correlator and scale determination in lattice QCD”, *PoS LATTICE2013*, 320 (2014), [arXiv:1312.0035 \[hep-lat\]](https://arxiv.org/abs/1312.0035).
- [147] B. Straßberger et al., “Scale setting for CLS 2 + 1 simulations”, *PoS LATTICE2021*, 135 (2022), [arXiv:2112.06696 \[hep-lat\]](https://arxiv.org/abs/2112.06696).

- [148] M. Cè et al., “Hadronic contributions to the anomalous magnetic moment of the muon from lattice QCD”, in *High performance computing in science and engineering '19* (Springer International Publishing, 2021), pp. 89–100.
- [149] M. Lüscher and S. Schaefer, “Lattice QCD with open boundary conditions and twisted-mass reweighting”, *Comput. Phys. Commun.* **184**, 519–528 (2013), arXiv:1206.2809 [hep-lat].
- [150] M. Lüscher and S. Schaefer, *openQCD*, <https://cern.ch/luscher/openQCD>.
- [151] R. G. Edwards and B. Joo (SciDAC, LHPC Collaboration, UKQCD Collaboration), “The chroma software system for lattice QCD”, *Nucl. Phys. B Proc. Suppl.* **140**, edited by G. T. Bodwin et al., 832–834 (2005), arXiv:hep-lat/0409003 [hep-lat].
- [152] C. R. Harris et al., “Array programming with NumPy”, *Nature* **585**, 357–362 (2020), arXiv:2006.10256 [cs.MS].
- [153] P. Virtanen et al. (SciPy 1.0 Contributors), “SciPy 1.0: fundamental algorithms for scientific computing in python”, *Nature Meth.* **17**, 261–272 (2020), arXiv:1907.10121 [cs.MS].
- [154] W. McKinney, “Data structures for statistical computing in Python”, in *Proceedings of the 9th Python in Science conference*, edited by S. van der Walt and J. Millman (2010), pp. 56–61.
- [155] J. Reback et al. (The pandas development team), *pandas*, <https://pandas.pydata.org/>.
- [156] F. Johansson et al., *mpmath: a Python library for arbitrary-precision floating-point arithmetic*, <https://mpmath.org/>.
- [157] E. O. Lebigot, *Uncertainties: a Python package for calculations with uncertainties*, <https://pythonhosted.org/uncertainties/>.
- [158] O. Tange, *GNU Parallel*, <https://www.gnu.org/software/parallel/>.
- [159] J. D. Hunter, “Matplotlib: a 2d graphics environment”, *Comput. Sci. Eng.* **9**, 90–95 (2007).
- [160] J. Bulava, M. Della Morte, J. Heitger, and C. Wittmeier, “Nonperturbative renormalization of the axial current in $N_f = 3$ lattice QCD with Wilson fermions and a tree-level improved gauge action”, *Phys. Rev. D* **93**, 114513 (2016), arXiv:1604.05827 [hep-lat].
- [161] M. Dalla Brida, T. Korzec, S. Sint, and P. Vilaseca, “High precision renormalization of the flavour non-singlet Noether currents in lattice QCD with Wilson quarks”, *Eur. Phys. J. C* **79**, 23 (2019), arXiv:1808.09236 [hep-lat].
- [162] P. Korcyl and G. S. Bali, “Nonperturbative determination of improvement coefficients using coordinate space correlators in $N_f = 2 + 1$ lattice QCD”, *Phys. Rev. D* **95**, 014505 (2017), arXiv:1607.07090 [hep-lat].
- [163] Sz. Borsányi et al. (Budapest-Marseille-Wuppertal collaboration), “High-precision scale setting in lattice QCD”, *JHEP* **1209**, 010 (2012), arXiv:1203.4469 [hep-lat].
- [164] G. Colangelo, S. Dürr, and C. Haefeli, “Finite volume effects for meson masses and decay constants”, *Nucl. Phys. B* **721**, 136–174 (2005), arXiv:hep-lat/0503014 [hep-lat].
- [165] U. Wolff (ALPHA Collaboration), “Monte Carlo errors with less errors”, *Comput. Phys. Commun.* **156**, 143–153 (2004), arXiv:hep-lat/0306017 [hep-lat], [Erratum: *Comput. Phys. Commun.* **176**, 383 (2007)].
- [166] B. De Palma, M. Erba, L. Mantovani, and N. Mosco, “A Python program for the implementation of the T -method for Monte Carlo simulations”, *Comput. Phys. Commun.* **234**, 294–301 (2019), arXiv:1703.02766 [hep-lat].

- [167] C. Kelly and T. Wang, “Update on the improved lattice calculation of direct CP-violation in K decays”, *PoS LATTICE2019*, 129 (2020), [arXiv:1911.04582 \[hep-lat\]](#).
- [168] J. Bijnens and J. Relefors, “Connected, disconnected and strange quark contributions to HVP”, *JHEP* **1611**, 086 (2016), [arXiv:1609.01573 \[hep-lat\]](#).
- [169] M. Ablikim et al. (BESIII Collaboration), “Measurement of proton electromagnetic form factors in the time-like region using initial state radiation at BESIII”, *Phys. Lett. B* **817**, 136328 (2021), [arXiv:2102.10337 \[hep-ex\]](#).
- [170] A. H. Hoang, M. Jezabek, J. H. Kühn, and T. Teubner, “Radiation of heavy quarks”, *Phys. Lett. B* **338**, 330–335 (1994), [arXiv:hep-ph/9407338 \[hep-ph\]](#).
- [171] M. K. Volkov, A. A. Pivovarov, and K. Nurlan, “On the mixing angle of the vector mesons $\omega(782)$ and $\phi(1020)$ ”, *Mod. Phys. Lett. A* **35**, 2050200 (2020), [arXiv:2005.00763 \[hep-ph\]](#).